Ceria Morphologies As Pd Nanoparticles Support For Heterogeneous Catalysis

Abdul Hanif Mahadi

360865

University College

A dissertation submitted for the degree of Doctor of Philosophy at the

Inorganic Chemistry Laboratory, Department of Chemistry

University of Oxford

2015

Ceria Morphologies As Pd Nanoparticles Support For Heterogeneous Catalysis

By

Abdul Hanif Mahadi

360865

University College

Supervisor

Professor S. C. Edman Tsang

Internal Accessor

Professor John S. Foord

A dissertation submitted for the degree of Doctor of Philosophy at the

Inorganic Chemistry Laboratory, Department of Chemistry

University of Oxford

2015

Table of Contents

DECLARATION

I confirm that this is my own work and the use of all material from other sources has been properly and fully acknowledged.

Abdul Hanif Mahadi

Bismillah Hirrahman Nirrahim

DEDICATION

To my dear wife, Syazwani, and to my parents and my family.

Acknowledgements

First and foremost, I would like to express my deepest gratitude to my supervisor, Professor S. C. Edman Tsang, for all his guidance and endless support throughout the course of my DPhil study. I would also like to thank the Chancellor's Scholarship from Universiti Brunei Darussalam, the Department of Economic Planning and Development, Prime Minister's Office and the Ministry of Education of Brunei for funding my entire DPhil course. I am also grateful to Oxford University for providing research equipment and facilities to carry out the experimental studies.

I would like to thank Dr. Neil Young and Dr. Phil Wiseman for training and assistance for TEM and XRD, respectively. I am also grateful to Dr. Aaron Chan and Dr. Simon Jones for training in the use of characterisation equipment and techniques in the lab.

I would like to express my gratitude to Dr. Simon Fairclough for all his assistance and diligence in performing the STEM-EELS experiments. I must thank Dr. Wei Chen and Professor Ian Metcalfe from Newcastle University, for all their help and discussions in the PIE experiments. Similarly, I must also thank Dr. Junjun Shan and Associate Professor Franklin Tao from University of Norte Dame, for their assistance and efforts with the AP-XPS experiments. Additionally, I would like to thank Dr. Jin Qu and Dr. Qin Lu for carrying out the DFT calculations and EPR measurements, respectively. Special thanks goes to Elizabeth Raine for the contribution on the methane combustion experiments and for proof reading this thesis. Also to Matthew Powell for his contribution during his part II project.

Finally, I would like to thank all members of the Tsang Group, both past and present, for their discussions, support and contributions, especially to Dr. Amy Kolpin, Ieuan Ellis, Bin Yu, Aaron Lau, Dr. Clive Eley, Dr. Serena Tiantian Jia for the in-depth discussions and friendship throughout the course of this project. I am also grateful to Associate Professor Jonathan Hobley from Universiti Brunei Darussalam for general discussion and advice. Finally and most importantly, I need to thank my wife, Syazwani Zaini, my parents, my family and my close friends for their selfless support throughout the DPhil course. And not to forget, my feline companion, Lucy, for her company during the thesis writing.

Ceria Morphologies As Pd Nanoparticles Support For Heterogeneous Catalysis

Abdul Hanif Mahadi

University College

Thesis submitted in partial fulfilment of the requirements for the degree of Doctor of Philosophy at the University of Oxford, Trinity Term, 2015

Abstract

Ceria is well known for its unique properties in fast oxygen mobility and formation of oxygen vacancies which makes ceria an excellent catalyst support for metal nanoparticles. Promotional effect of ceria has been well established in a number of reactions including three-way catalyst and CO oxidation. These unique properties of ceria are dependent on the surface facets it exposes, where they can be enhanced by the exposure of high energy surfaces such as (100) and (110).

The work presented in this thesis involves controlling the surface exposed by the ceria support by making them into cube and rod morphology, which predominantly expose the (100) and (110) surface, respectively. Hence, the effect of these surfaces on the ceria support can be investigated. The ceria morphologies were deposited with Pd nanoparticles and their catalytic properties were tested on methane combustion and gas-phase formic acid decomposition reactions. In both of the catalyst test reactions, the Pd deposited on the ceria cubes support had shown superior catalytic properties compared to the Pd deposited on the ceria rods support, indicated by the former's higher activity, TOF and resistance to poisoning. Based on the characterisation techniques performed in this study such as TPR, ambient pressure XPS, STEM-EELS and pulse isotopic oxygen exchange, the enhanced catalytic properties of Pd/ceria cubes were attributed to the high energy ceria (100) surface which led to more favourable formation of oxygen vacancies and faster oxygen mobility.

Keywords: Heterogeneous catalysis, ceria morphologies, methane combustion, gas-phase formic acid decomposition, oxygen mobility, oxygen vacancy formation.

List of Figures

List of Tables

List of Abbreviation

ΔG – Change in Gibb's free energy

ΔH – Change in enthalpy

ΔS – Change in entropy

AP-XPS – Ambient pressure x-ray photoelectron spectroscopy

CCD – Charge-coupled device

DFT – Density functional theory

DI – Deionised

EELS – Electron energy loss spectroscopy

EPA – Environmental Protection Agency

EPR – Electron paramagnetic resonance

FID – Flame ionisation detector

GC – Gas chromatography

HAADF – High angle annular dark field

MS – Mass spectrometry

PIE – Pulse isotopic exchange

PGM – Platinum-group metals

RT – Room temperature

SEM – Scanning electron microscope

STEM – Scanning transmission electron microscope

TCD – Thermal conductivity detector

TEM – Transmission electron microscopy

TOF – Turnover frequency

TON – Turnover number

TPR – Temperature programmed reduction

UHV – Ultra high vacuum

XPS – X-ray photoelectron spectroscopy

XRD – X-ray diffraction

List of Publication

Interstitial modification of palladium nanoparticles with boron atoms as a green catalyst for selective hydrogenation.
C. W. A. Chan, A. H. Mahadi, M. M. J. Li, E. C. Corbos, C. Tang, G. Jones, W. C. H. Kuo, J. Cookson, C. M. Brown, P. T. Bishop and S. C. E. Tsang, *Nat. Commun.*, 2014, **5**, 9.

1 Introduction

Contents

1.1 Catalysis

In the last few decades of the 20th century, concerns have been raised over the impact of industry on the global environment. Since the beginning of the industrial revolution in the 18th century, the chemical industry has risen exponentially which caused the increase in air pollutants and greenhouse gases, toxic chemicals in rivers and streams, a hole in the ozone layer and polluted city atmospheres. In the early 1990's, the Environmental Protection Agency (EPA), an agency of the US government introduced the term 'green chemistry' which aims at sustainability of the environment[1]. One of the key principles to highlight the concept of green chemistry is the use of catalysts as opposed to classical stoichiometric methods.

Another contribution of catalyst to green chemistry is the reduction of air pollutants production. For example, it is a requirement for all gasoline powered vehicles starting with the 1975 model year to be fitted with catalytic converters, to comply with the EPA regulations on exhaust emissions[2]. The role of the catalytic converter is to convert toxic pollutants such as CO, NO_x and hydrocarbons in the exhaust to safer gases, N_2, CO_2 and H_2O before they are released to the atmosphere[3].

The importance of catalyst is emphasised when Richard F. Heck, Ei-ichi Negishi and Akira Suzuki were awarded The Nobel Prize in Chemistry for their 'palladium catalysed cross-couplings in organic synthesis'[4]. Even before catalysis was intended for the purpose of green chemistry, catalyst technologies have been making large contributions to the chemical industry. One notable achievement was the discovery made by Fritz Haber and Carl Bosch when they applied iron catalyst for ammonia synthesis. It has been referred to as 'the most important invention of the 20th century' due to its impact in population growth as ammonia and its derivatives have been used as fertilisers for food crop production[5].

The word catalyst was first coined by J. J. Berzelius in 1836 to rationalise the unexplainable reactions observed by Michael Faraday who demonstrated that a platinum sponge was able to sustain ethanol oxidation and the oxidation of hydrogen by platinum discovered by J. W. Dobereiner[6]. Berzelius wrote *"Catalytic power actually means that substances are able to awake affinities which are asleep at this temperature by their mere presence and not by their own affinity"*[7].

The current accepted definition of a catalyst is that it is a *'substance that increases the rate at which a chemical system approaches equilibrium, without being consumed in the process'*[7]. As the catalyst is not altered in the reaction, it can be recycled which is an advantage compared to stoichiometric methods. A catalyst increases the rate of reaction by lowering the activation energy of the reaction (Figure 1.1) as expressed in the Arrhenius equation (Equation 1.1)[8].

$$k = Ae^{-\frac{E_a}{RT}}, \text{ where} \qquad \text{Equation 1.1}$$

where k is the rate constant, A is the pre-exponential factor, E_a is the activation energy, R is the gas constant and T is the absolute temperature.

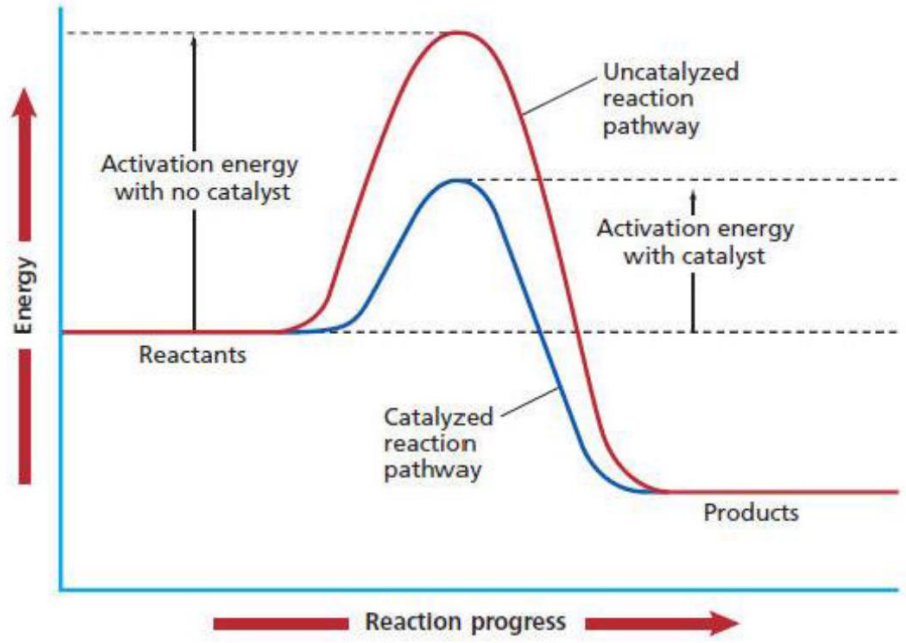

Figure 1.1 A schematic of energy profile diagram of a catalysed reaction compared to an uncatalysed reaction[9].

The implication of this is that chemical processes involving exothermic reactions could be performed at lower temperatures[10], hence making the processes more economical and energy efficient. However, the equilibrium position of the reaction is still governed by thermodynamics, where $\Delta G > 0$ for the reaction to occur (Equation 1.2 and 1.3). Therefore a catalyst cannot speed up a thermodynamically unfavourable reaction ($\Delta G < 0$).

$$\Delta G = \Delta H - T\Delta S \qquad \text{Equation 1.2}$$

At equilibrium, $\Delta G^o = -RTlnK$ Equation 1.3

1.1.1 Types of catalysis

All catalyst systems share the same fundamental principle of catalysis, which is the lowering of the activation energy. They are divided into 3 categories:

- Homogeneous catalysis
- Heterogeneous catalysis
- Biocatalysis

A homogeneous catalysis system is where the catalyst and the reactants are in the same phase and no phase boundary exists. This could occur in gas phase such as the catalysis of sulphur dioxide oxidation by nitrogen oxide, or more commonly homogeneous catalysis which is done in the liquid phase. Liquid phase homogeneous catalysts usually involves organometallic complexes which consist of a metal centre surrounded by ligands to stabilise the metal atom. One example is the use of Pd complexes as a catalyst for the formation of a carbon-carbon bond[11]. Organometallic complexes benefit from a high degree of control over the catalytic properties by the modification of its metal centre or ligands through electronic or steric effects[12, 13]. Hence homogeneous catalysis is generally applied in the pharmaceutical industry where the ability to tune the selectivity of the products is the top priority. However, due to the absence of phase boundary, recycling of homogeneous catalyst is a challenge and requires excessive solvent for the work up procedures.

Biocatalysis consists of the use of biologically occurring catalysts such as protein enzymes to perform catalytic reactions. Due to the complex structure of these naturally-made proteins, reactions with high activities and selectivities can be achieved with a high yield of enantiomerically pure molecules and most importantly under mild conditions[14]. The downside to using protein enzymes as catalysts is that they are very sensitive to changes in temperatures, pressure and pH, hence making them unsuitable for most industrial processes[15].

In contrast to homogeneous catalysis, heterogeneous catalysis is when a phase boundary separates the catalyst from the reactants. A number of catalyst/reactant phase combinations can occur such as liquid/gas in the polymerisation of alkenes catalysed by phosphoric acid, solid/liquid in gold catalysed decomposition of hydrogen peroxide reaction and solid/liquid + gas in hydrogenation of nitrobenzene to aniline with Pd catalyst[7]. However, solid catalysts make up the majority of heterogeneous catalysis because of their robustness under extreme conditions (high temperature and pressure) and also its simplicity in separation from reactants and products[16]. For example, in solid/liquid system, the catalyst separation can be done with a simple filtration and no separation procedure is needed in solid/gas system. For these reasons, the design of high-throughput continuous flow reactors is made possible in gas-phase industrial synthesis. Solid catalysts are also applied in the automotive industry with the use of catalytic converters mentioned earlier. They are fitted into the exhaust of all gasoline powered vehicles and usually require minimal maintenance[17]. Currently, solid catalysts account for nearly 90% of the all catalysts sold[18].

1.1.2 Heterogeneous Solid Catalysis

In heterogeneous solid catalysis, the reaction occurs on the surface of the catalyst, as such the surface of the catalyst is regarded as the active site. When a reactant molecule collides with the surface of a catalyst, a number of events can occur. The molecules could either be elastically or inelastically scattered or they could 'stick' to the surface, which is termed adsorption. However, the type of adsorption of the reactant molecules depends on strength of the interaction forces. Interaction forces such as van der Waals and electrostatic attraction in the case of molecules with permanent dipole moments only exert physical attraction between the reactant and the surface, thus bind without alteration of the reactant atom/molecule. This adsorption is referred to as physical adsorption or physisorption. On the other hand, the reactant

atom/molecule can react chemically with the surface of the catalyst which involves rearrangement of the electrons within the atom/molecules. This form of adsorption is called chemical adsorption or chemisorption[7]. For a surface catalysed reaction to occur, chemisorption of the reactant is the essential initial step[8, 19].

A typical surface catalysed reaction is the synthesis of ammonia with an iron based catalyst shown in Figure 1.2, known as Haber-Bosch reaction. The reaction is started with the chemisorption of N_2 and H_2 reactants followed by the reaction of the chemisorbed reactants to produce NH_3. The ammonia product is then desorbed from the catalyst surface, leaving the catalyst in its original state[20]. Under this reaction scheme, all the processes exhibit their own activation energies. The rate determining step is given by the process with the highest activation energy[21], which in this case is the chemisorption of the reactants (E_{cat}). By going through these processes on the surface of the catalyst, the activation energy is lowered compared to the activation energy of the uncatalysed reaction (E_{homo}). Hence, the chemisorption of N_2 onto the surface assists the cleavage of the strong nitrogen triple bond. It is also noted that in the catalysed reaction scheme, the thermodynamic favourability of the reaction is unchanged as it is determined by the relative energies of the reactants and products.

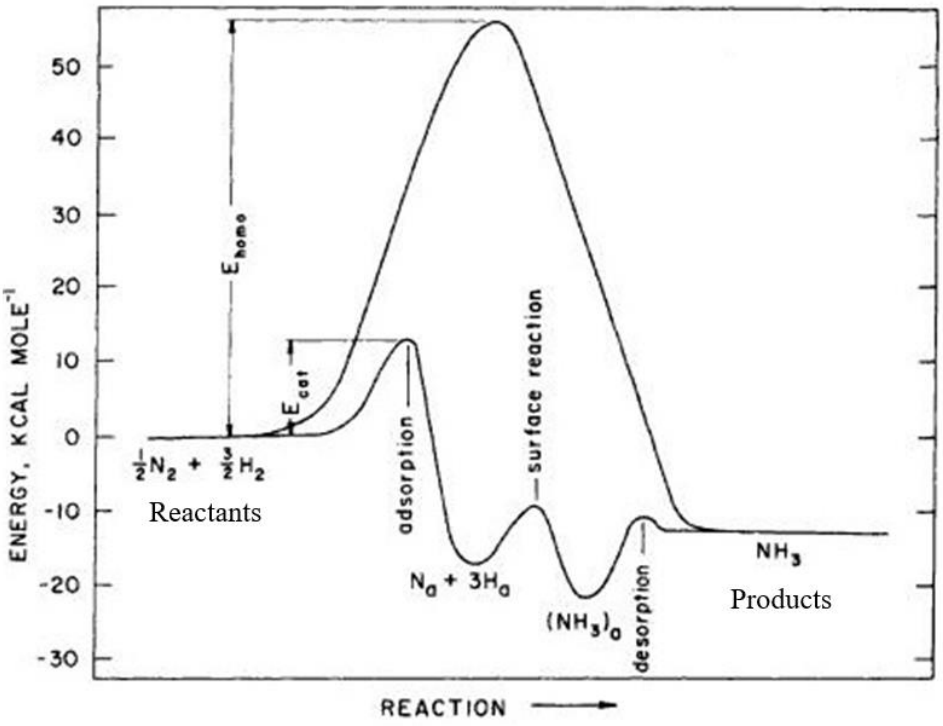

Figure 1.2 A schematic of energy profile diagram of a catalysed Haber-Bosch reaction for ammonia synthesis compared to the uncatalysed reaction[20].

According to Sabatier, the chemisorption strength of the reactant atom/molecule on the catalyst surface is the key to determining the activity of the catalyst for a given reaction. If the reactant is adsorbed too weakly, it would be desorbed off the surface easily before any reactions could occur[8]. On the other hand, if the chemisorption strength is too strong, it would create an energy barrier for any reaction to take place and be unable to desorb from the surface, hence blocking the surface resulting in the poisoning of the catalyst. Therefore, the chemisorption strength of the reactant to the catalyst surface has to be 'just right' to achieve a high activity and this is known as the Sabatier Principle.

The Sabatier Principle was used to justify the volcano plot observed by Balandin in the decomposition of formic acid reaction. He found the volcano trend between the chemisorption strength of formate on a series of transition metals and their decomposition temperatures

(Figure 1.3)[8, 22]. In the decomposition reaction, formic acid was dissociatively chemisorbed on the catalyst surface to form formate, where it could be decomposed into carbon dioxide and water or carbon monoxide and hydrogen. The activity of the reaction was represented by the temperature at which decomposition was achieved, with lower temperature indicating the higher activity. It was demonstrated that the decomposition temperature was at its highest when the chemisorption strength of formate was too weak (Au) and when it was too strong (W). Whereas the lowest decomposition temperature, which indicated the highest activity was observed when the chemisorption strength was in the centre at the 'just right' strength.

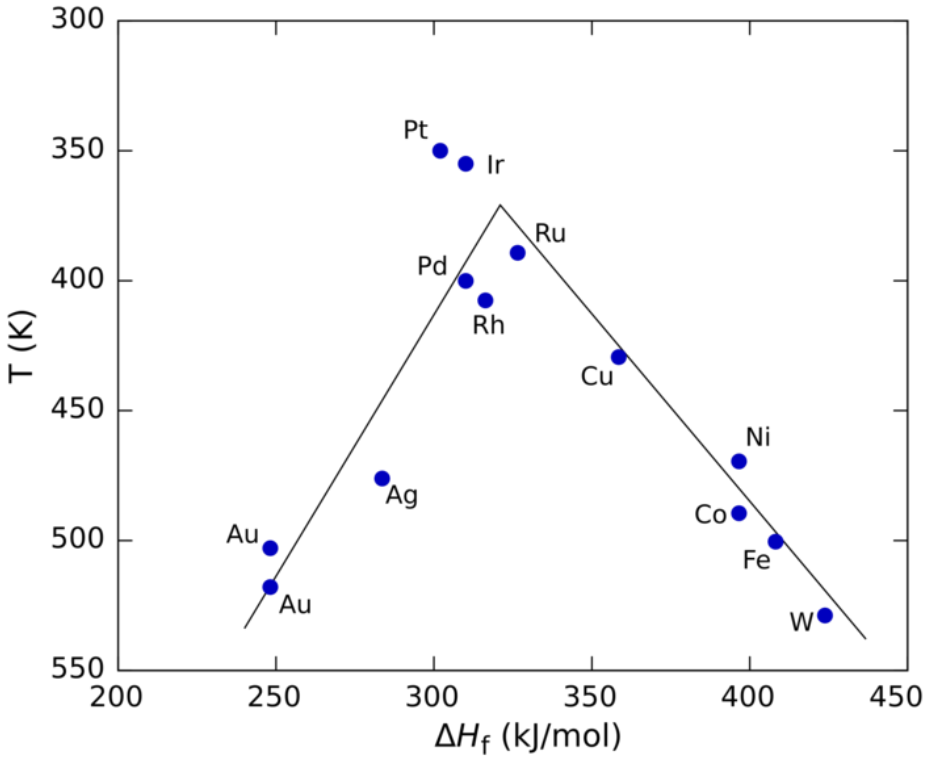

Figure 1.3 A volcano plot of the temperature of decomposition of formic acid reaction against the adsorption strength of formate on different transition metals[19].

Other than the adsorption of the reactants, the desorption of the products is also a crucial step so that the catalyst surface is available for another cycle of reaction or a reaction turnover. Therefore, for an efficient solid catalyst, it is essential for reactants to chemisorb sufficiently

strongly on the catalyst surface for the reaction to occur and products to desorb quickly for a fast catalytic cycle termed as the turnover rate.

The performance of the catalyst usually takes into account its activity and ability to turnover for another catalytic cycle. Hence, catalysts are usually compared by these parameters[23, 24]:

- The specific rate, the rate of reaction divided by the weight of the catalyst.
- The areal rate, the rate of the reaction divided by the catalyst surface area.
- Turnover number (TON), the number of reactant molecules converted per surface atom or unit surface area of the catalyst.
- Turnover frequency (TOF), the number of reactant molecules converted per surface atom or unit surface area of the catalyst per unit time.

As the reactions occur on the surface of heterogeneous solid catalyst, not all the catalyst mass is utilised in for the catalysis. Instead only the surface of the catalyst is regarded as the active sites. Therefore, areal rate, TON and TOF are more appropriate representations of the activity of a solid catalyst as these parameters took the surface atoms/area into account as opposed to the specific rate.

1.1.3 Efficient Catalyst

Whilst activity of a catalyst is a key parameter, its selectivity is also an important factor. An efficient catalyst needs to have high activity as well as high selectivity towards the desired products. The production of side products is deemed as waste and on industrial scale, these waste productions can be uneconomical and costly as the unwanted products have to be

separated from the desired products. In some cases, the unwanted products may adsorb strongly to the catalyst surface and block the surface from adsorption of reactant which results in the deactivation of the catalyst. These species are known as 'poisons' and CO is a typical example[25]. There are also a number of factors that contributes to the deactivation of a catalyst such as metal evaporation, leaching, reduction, oxidation, corrosion, coking, change in active site and sintering[25-27]. Hence the development of highly efficient catalyst is a key aspect in current catalysis research, with a focus on incorporating high activity, selectivity and resistance to deactivation[28, 29].

1.1.4 Kinetics

As catalysts are used to speed up a reaction, it is important to consider the reaction kinetics of a surface catalysed reaction. The first step for a surface catalysed reaction is the adsorption of the reactants to the active sites on the surface of the catalyst. An adsorption isotherm is the relationship between the quantity of gas adsorbed and the partial pressure of the gas at equilibrium at a constant temperature[7]. Hence, if x is the amount of gas adsorbed and x_{max} is the maximum amount the surface of the catalyst can accommodate, the fractional surface coverage is given as θ, where

$$\theta = \frac{x}{x_{max}} \qquad \text{Equation 1.4}$$

In a simplest case of unimolecular reaction, where only a single reactant and the catalyst surface are to be considered, the adsorption of a gaseous reactant can be expressed as

$$A + M^* \rightleftharpoons AM \qquad \text{Equation 1.5}$$

Where A is the reactant, M* is the unoccupied active sites and MA is the occupied active site where A is chemisorbed. When the system is in equilibrium, the equilibrium constant, K_A can be expressed as

$$K_A = \frac{[MA]}{[A][M^*]} \qquad \text{Equation 1.6}$$

Where [MA], [A] and [M*] are their equilibrium concentrations. Using Langmuir adsorption model, which assumes that an adsorbate behaves as an ideal gas at isothermal conditions, [A] can be replaced by p_A, the partial pressure of A at equilibrium, [M], by $(1 - \theta_A)$ and [AM] is replaced by θ, resulting in

$$K_A = \frac{\theta_A}{p_A(1-\theta_A)} \qquad \text{Equation 1.7}$$

Where upon rearrangement, gives the Langmuir adsorption isotherm.

$$\theta_A = \frac{K_A p_A}{1+K_A p_A} \qquad \text{Equation 1.8}$$

Hence, for a unimolecular reaction, the total scheme of the reaction is given by

$$A_{(g)} \underset{k_{-1}}{\overset{k_1}{\rightleftharpoons}} A_{ads} \overset{k_2}{\rightarrow} P_{(ads)} \underset{k_{-3}}{\overset{k_3}{\rightleftharpoons}} P_{(g)} \qquad \text{Equation 1.9}$$

$$\text{Rate} = k_2\theta_A = \frac{k_2 K_A p_A}{1+K_A p_A} \qquad \text{Equation 1.10}$$

where P is the product and k_2 is the rate determining step ($k_2 \gg k_1$, $k_2 \gg k_3$ and $K_A = \frac{k_1}{k_{-1}}$).

The Langmuir adsorption isotherm can also be applied to bimolecular surface catalysed reactions, where the most common model used is the Langmuir-Hinshelwood mechanism[30]. The key assumption made in this mechanism is that the catalyst surface consists of identical non-interacting sites, thus the adsorption between the adsorbates can be treated with equal probability at each site. Under the Langmuir Hinshelwood mechanism, both of the reactants are adsorbed on the surface where they can react and form the product in which is finally desorbed from the surface. It is the mechanism used to model the Haber-Bosch ammonia synthesis shown in Figure 1.2. Under this mechanism, the reaction is expressed as

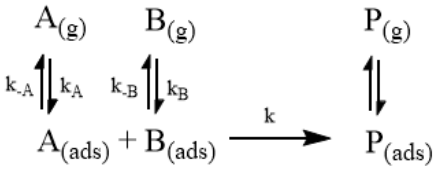

Equation 1.11

where A and B are the reactants and P is the product. Assuming the rate of reaction between A and B is much slower than the attainment of adsorption-desorption equilibrium of the reactants and products, the rate of the reaction is given by

$$Rate = k\theta_A\theta_B \qquad \text{Equation 1.12}$$

By assuming Langmuir adsorption model

$$K_A = \frac{\theta_A}{p_A(1-\theta_A-\theta_B)} \qquad \text{Equation 1.13}$$

$$K_B = \frac{\theta_B}{p_B(1-\theta_A-\theta_B)} \qquad \text{Equation 1.14}$$

$$\text{Rate} = \frac{kK_A p_A K_B p_B}{(1+K_A p_A+K_B p_B)^2} \qquad \text{Equation 1.15}$$

Another less commonly used bimolecular surface catalysed reaction is the Eley-Rideal mechanism, where only one of the reactants is chemisorbed onto the surface. This adsorbed reactant reacts with unadsorbed reactant to give the product, which is then desorbed from the surface. Under this mechanism, the reaction scheme is given by

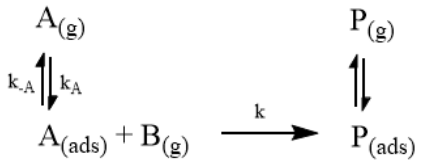

Equation 1.16

However it cannot be assumed that reactant B totally does not adsorb on the surface. Hence, B is assumed to compete with A for the surface sites and must be taken into consideration for the rate expression.

$$\text{Rate} = \frac{kK_A p_A p_B}{1+K_A p_A+K_B p_B} \qquad \text{Equation 1.17}$$

From the rate equation, the Eley-Rideal mechanism does not tend to reach a maximum when p_A and p_B are changed, as opposed to the Langmuir-Hinshelwood mechanism, hence this property is used to distinguish between these two mechanisms.

All these models used to derive the rate expressions for surface catalysed reactions are based on the Langmuir adsorption model which does not apply to real catalyst working conditions, as Langmuir himself noted[31]. However, by using these models, it is made possible to gain more understanding in the kinetics of real catalyst surfaces.

1.2 Metal Nanoparticle Catalysis

1.2.1 Size Effect

Surface chemistry plays an important role in heterogeneous solid catalysis. As all the reactions occur on surfaces, it is vital for these surface active sites to be maximised. One approach to increase the surface area is to design these catalysts into nanoparticles, particles with sizes between 1 – 100 nm, to maximise their surface area to volume ratio. In addition, solid catalysis usually involve expensive platinum group metals (PGM). In August 2015, the monthly average prices for Pt and Pd were US$ 990.92 /oz. and US$ 598.92 /oz. respectively[32]. Therefore, it is essential to maximise the catalytic usability of these metals. Figure 1.4a illustrated the exponential increase in CO oxidation activity as the gold catalyst size was decreased, despite gold being known for inertness[33]. The increase of activity became more apparent when the size of gold nanoparticles was less than 5 nm.

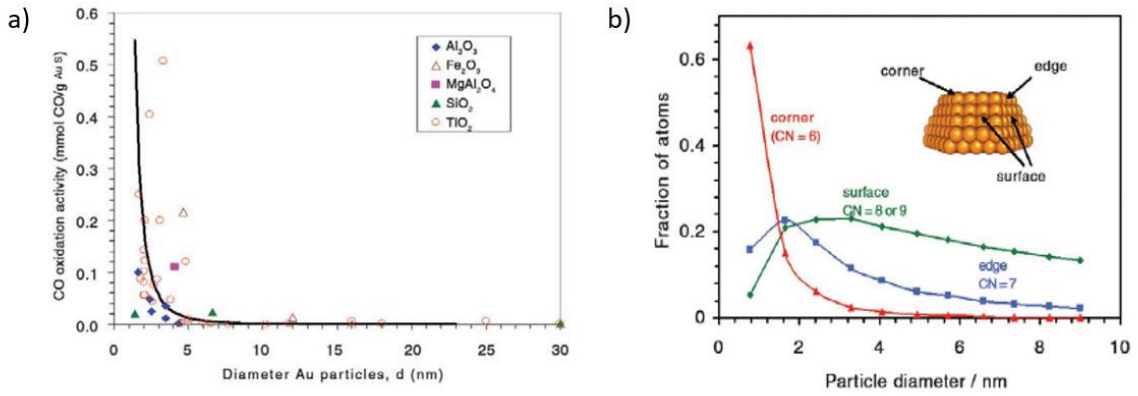

Figure 1.4 a) The activities of CO oxidation catalysed by different sizes of gold nanoparticles. b) The proportion of different coordination numbers on surface atoms of gold nanoparticles with respect to its size[33].

However, this phenomenon is not totally attributed to the increase in surface area to volume ratio. From Figure 1.4b, as the gold particle diameter decreased below 5 nm, the fraction of corner atoms was increased, coinciding with the increase in CO oxidation activity[33]. This indicated that the higher fractions of low coordinated atoms on the surface of the catalyst contributed to higher catalytic activity. Theoretically, atoms with low coordination numbers results in stronger adsorption of adsorbates than higher coordinated sites[34], which in this case increased the catalytic activity.

1.2.2 Electronic Effect

When a metal is in the nanoparticle size regime, its electronic properties resembled a transition between its bulk metallic state and its individual molecules (Figure 1.5). In bulk metallic state, the overlapping of d-orbitals from an extremely large number of metal atoms form a complete, continuous band structure[35, 36]. As the particle size is decreased into the nanoscale region, the band structure gradually splits into delocalised band states, separated by a band gap which increases as the particle size gets smaller. This is termed as the quantum size effect. This effect

carries on until the band structure devolves completely leading to the formation of discrete molecular orbitals resulting in the complete loss in metallic character.

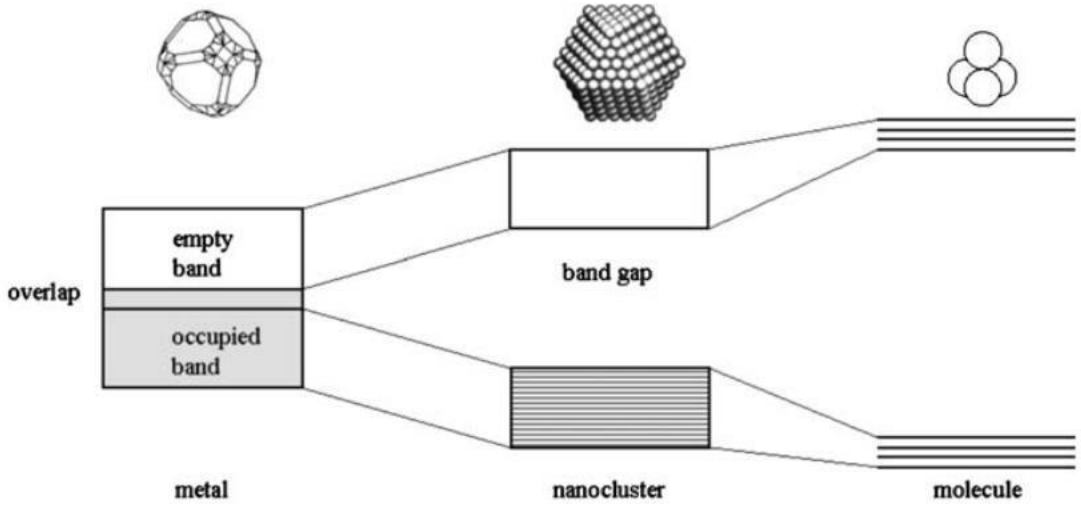

Figure 1.5 The quantum size effect which illustrates the change in electronic structure of metal in relation to its particle size[35].

For transition metal nanoparticles, the quantum size effect results in a narrow d-band in relative to the s-band, due to the low coupling between d-states[37]. By applying band theory, Hammer and Norskov proposed a theory to explain the relationship between the transition metal electronic properties and its adsorption strength whereby the surface-adsorbate interaction occurs in two steps[38]. Firstly, the adsorbate interacted with the s-band of the metals resulting in deep-lying filled bonding state and an empty anti-bonding state. Since all transition metals have a half-filled s-band (in metallic state)[39], this interaction contributes to little variation on the adsorption strength. Secondly, the bonding states interact with the metal d-states leading to the formation of lower energy bonding states and also an anti-bonding states above the metal d-bands (Figure 1.6a). The adsorption strength is influenced by the filling of these bonding and anti-bonding states, where the filling of the anti-bonding states results in a weaker surface-adsorbate bond[40]. In a metallic system, the occupancy of this anti-bonding state depends on its energy relative to the Fermi level[39]. Hence, the narrowing of d-band due to the decrease in the

metal nanoparticles size generally results in the increase of its d-band centre, shifting closer to the Fermi level, leading to stronger adsorption strength of adsorbates (Figure 1.6b).

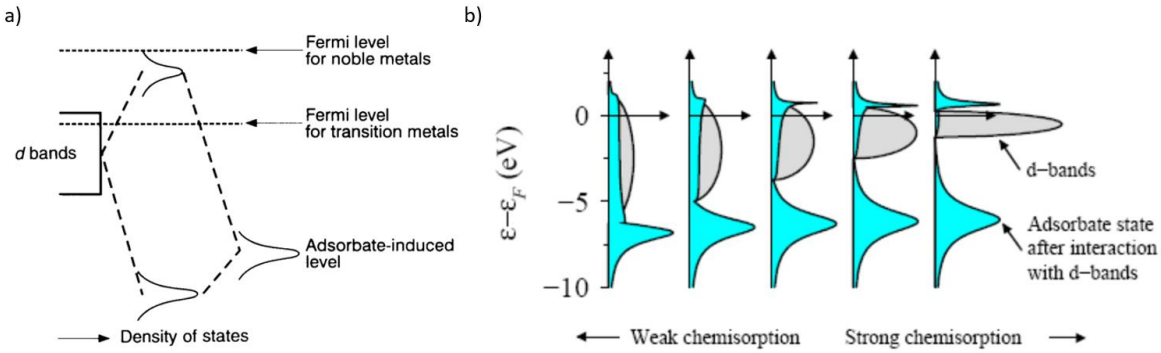

Figure 1.6 a) A schematic illustration of electronic interaction between metals and an adsorbate on the surface of the metal[38]. b) A schematic representation of the influence of the narrowing of d-band structure on the chemisorption strengths[37].

This theory was applied in the case of gold nanoparticles, where an increase in activity was observed when the particles size is less than 5 nm (Figure 1.4a). Concurrently, the increase of surface atoms with low coordination number also contributes to the narrowing of the d-band and shifting it closer to the Fermi level[34]. Thus below a certain cluster size, the anti-bonding states lie above the Fermi level, resulting in stronger CO adsorption strength on the gold surfaces, which in this case increased the CO oxidation activity.

The adsorption strengths of formate onto different transition metals surface could also be justified using this theory (Figure 1.3). Since the energy of the d-states in relative to their Fermi level varies between different metals, it influences the occupancy of their bonding and anti-bonding states which determines the surface-adsorbate strengths[39, 41]. Going across the transition metal period increases the energy gap between the d-band centre and the Fermi level, hence increasing the filling of the anti-bonding states, resulting in weaker adsorption strengths (Figure 1.6a). The same reason also applies going down a transition metal group.

With the understanding of the electronic bonding properties of the surface-adsorbate interaction, the adsorption strength between an adsorbate and a metal catalyst can be modified and fine-tuned by changing its Fermi level and/or d-band centre. This can alter the filling of the bonding and anti-bonding states due to the change in Fermi level and d-band centre energy gap. This leads to the development of electronic modification of catalyst for example through alloying[42], doping[28], changing metal bond length[43] and the use of supports[44].

1.2.3 Support

Synthesising the metals into nanoparticles however make them unstable due to the increase in surface energy because of the high surface area to volume ratio. Hence they tend to agglomerate or sinter into larger particles to gain thermodynamic stability[8]. Therefore, these small nanoparticles need an external source of stability in order to maintain their small sizes. One approach is to attach ligands onto the surface of the nanoparticles that refrain them from agglomerating through steric or electrostatic repulsion[45]. However, these ligands are usually composed of organic materials which limits the catalyst applications at high temperatures, as the ligands could easily be decomposed. The ligands could also block the surface of the metals resulting in lower catalytic activity due to the blockage of active sites[46].

Another method used to stabilise the small sized nanoparticles is by attaching them to a support[47]. The crucial property that these supports need to possess is a high surface area so that the nanoparticles can be highly dispersed throughout the surface of the supports[48]. A wide range of materials can be used as supports varying from organic materials such as activated carbon and charcoal to inorganic materials such as alumina and silica. Inorganic materials tend to be

the choice for high temperature applications due to their high stability and high decomposition and melting temperatures, for example alumina has a melting point of 2072 °C[49].

Other than providing stability for nanoparticles, some supports can also alter the properties of the supported metal nanoparticles through their interactions which in turn can alter their catalytic properties and this is termed as strong metal-support interaction (SMSI)[50-52]. SMSI was first reported by Tauster *et. al.* in the 1970's where they found that PGM nanoparticles supported on titania lost the ability for H_2 and CO chemisorption when they were treated at high temperatures[53]. The authors suggested that the loss of chemisorption ability was not due to the particles sintering, but attributed to the alteration of the charge state of the metal due to the interaction with electrons of titania.

1.3 Ceria

PGM metals on a ceria support system have been shown to exhibit the SMSI[44, 51, 54]. In contrast to titania, PGM metals on ceria supports have shown to enhance the catalytic activity. Both theoretical and experimental studies since the 1980s have indicated the positive effect of the ceria support[55]. The raised interest in the PGM/ceria system started in accordance to the reducible nature of ceria[55]. This led to its development for applications in three way catalysts[52, 56-58], CO oxidation[58-61], the water gas shift reaction[62, 63], oxygen sensors[64-66] and solid oxide fuel cells[67-69]. The excellent activity of ceria-based catalyst in these applications is attributed to the ceria oxygen storage capacity, oxygen vacancy formation and oxygen mobility properties. This results from the ability of ceria to shift between the oxidised and reduced state ($Ce^{3+} \leftrightarrow Ce^{4+}$) easily[56, 57, 70, 71].

CeO_2 or commonly known as ceria has a cubic fluorite crystal structure, space group F*m*3*m*[56, 72]. The Ce cations are arranged in a face-centred cubic structure with the O anions filling the tetrahedral holes (Figure 1.7). The lattice constant cubic unit cell is 5.41 Å. Each Ce cation is bonded to eight O anions while each O anion is bonded to four Ce cations.

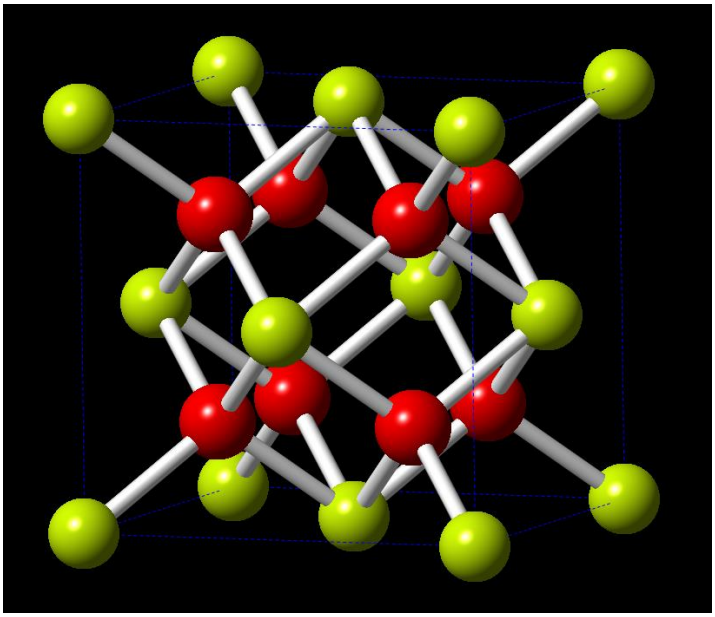

Figure 1.7 Cubic fluorite structure of CeO_2.

A fully reduced ceria, Ce_2O_3 on the other hand has a hexagonal structure, space group $P\bar{3}ml$. However, it has been suggested that the reduction of ceria to a partially reduced state, retains the fluorite structure of CeO_2 for the intermediate composition of CeO_{2-x}, $0.5 < x \leq 0$[73, 74]. Hence, oxygen vacancies can be formed in ceria without any major structural changes.

Since surface chemistry plays an important role in solid catalysis, it is essential to consider the surfaces of ceria. The low-index surfaces of ceria are (111), (110) and (100), with each of them varies in their surface structure and stability[75-78]. This variation in stability would lead to the

difference in their metal-support interaction and the modification of the unique properties of ceria mentioned earlier.

1.4 Morphology control

According to Wullf's rule, the crystal planes exposed on the surface of a crystalline material are determined by its morphology[79]. Thus, the surface exposed by a nanoparticle can be administered by controlling their morphologies. This leads to the advancement of morphology-controlled synthesis of various materials, for example it has been reported that CeO_2, CuO, TiO_2 and Co_3O_4, show examples of different morphologies such as nano-sized cubes, rods, belts, plates and octahedrons[80-82].

As mentioned in the previous section, varying the surface facets exposed on a nanoparticle could result in an alteration of its surface chemistry, which influences its catalytic properties. The role of morphology dependency on catalysis was first tested by Zhou *et. al.* where they found single crystalline rod-shaped ceria showed higher catalytic activity in the CO oxidation reaction compared to traditional polycrystalline ceria nanoparticles, despite the surface area of the rods being smaller[59]. The enhanced catalytic activity of morphology-controlled ceria was also evident in other catalysed reaction such as methanol and ethanol reforming[83, 84] and the water-gas shift reactions[85, 86].

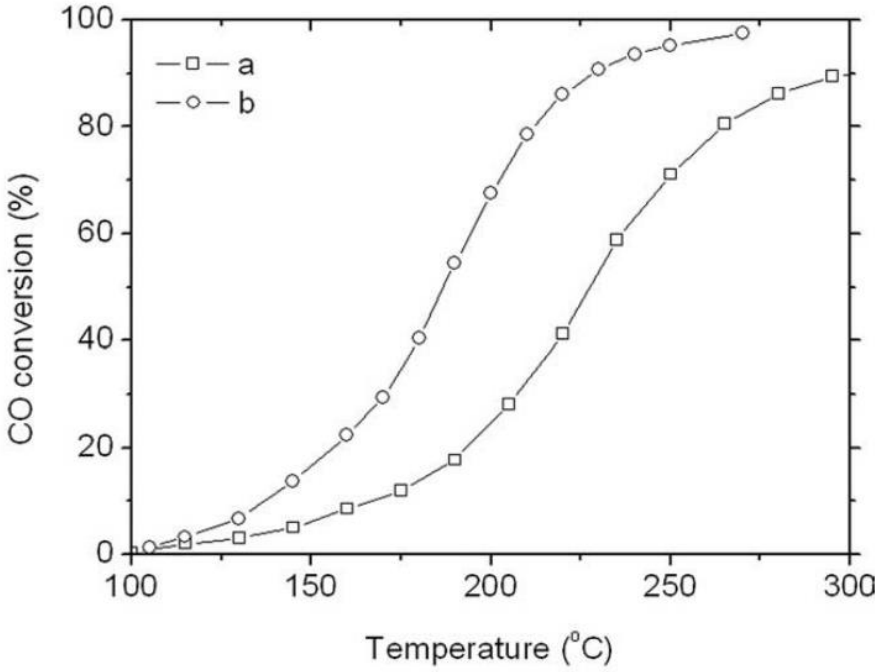

Figure 1.8 The percentage of CO conversion with respect to temperature for CO oxidation reaction catalysed by a) traditional ceria nanoparticles b) ceria nanorods[59].

Controlling the morphologies of the support can also alter the properties of the catalyst, especially when the support contributes to the catalytic properties through SMSI[87-90]. Liao *et. al*. reported the increase in selectivity of methanol production in the hydrogenation of CO_2 with Cu deposited on ZnO plates support compared to the rods support[91]. They attributed the enhanced selectivity to the polar (002) facets of the ZnO plates as opposed to non-polar (100) facets on the rods.

1.5 Aims and objectives

The objective of this study is to investigate the role of different ceria surfaces as a support for Pd nanoparticles in heterogeneous solid catalysis, by controlling the morphologies of the ceria support. We postulate that by synthesising these ceria morphology supports could result in enhancement in the catalytic properties of the supported Pd in the catalyst test reactions. In

addition, we aim to characterise these different ceria surfaces to gain a deeper understanding into the surface chemistry of this unique support that provides properties such as oxygen vacancy formation and oxygen mobility.

In order to achieve these objectives, we aim to execute the following methodologies:

- Synthesise single crystalline ceria morphologies that expose a specific surface.
- Deposit Pd nanoparticles onto the ceria morphologies.
- Evaluate the catalytic properties of the Pd deposited ceria morphologies in catalyst test reactions.
- Investigate the surface properties of the different ceria surfaces exposed on the morphologies.

1.6 Thesis overview

This thesis consists of seven chapters with Chapters 4 – 7 detailing the research I have done over the course of my DPhil study.

Chapter 1 – Introduces the principles of heterogeneous catalysis, the basics of ceria and the recent developments in morphology-controlled nanostructures.

Chapter 2 – Introduces the theories of the most commonly applied analytical techniques of characterisation of solid catalyst.

Chapter 3 – Experimental description of synthesis methods and characterisations of solid catalysts.

Chapter 4 – Reviewing the recent developments in synthesis of ceria morphologies and Pd deposition methods and describes their synthesis methods, characterisations and thermal stabilities.

Chapter 5 – Introduces the theory of catalysed methane combustion and gas-phase formic acid decomposition reactions. The catalytic properties of Pd deposited on the ceria morphologies support were tested on these reactions.

Chapter 6 – The study of ceria surfaces exposed by the different morphologies using various characterisation methods.

Chapter 7 – Summarises the conclusions presented throughout this thesis and the future perspective of the research.

1.7 References

1. http://www2.epa.gov/greenchemistry.

2. T. Palucka, *Invention & Technology*, 2004, 19.

3. D. Ciuparu, M. R. Lyubovsky, E. Altman, L. D. Pfefferle and A. Datye, *Catalysis Reviews*, 2002, 44, 593-649.

4. http://www.nobelprize.org/nobel_prizes/chemistry/laureates/2010/.

5. V. Smil, *Nature*, 1999, 400, 415-415.

6. J. J. Berzelius, *Jahresbericht*, 1836, 15, 237-243.

7. G. C. Bond, *Heterogeneous Catalysis: Principles and Applications*, Oxford Science Publications, 2 edn., 1986.

8. J. M. Thomas and W. J. Thomas, *Principlies and Practice of Heterogeneous Catalysis*, Wiley-VCH, 1997.

9. http://imgarcade.com/1/exothermicreaction-graph-with-catalyst/).

10. S. D. Jackson, J. S. J. Hargreaves and D. Lennon, *Catalysis in Application*, Royal Society of Chemistry, 2003.

11. J. P. Corbet and G. Mignani, *Chem Rev*, 2006, 106, 2651-2710.

12. G. J. P. Britovsek, V. C. Gibson and D. F. Wass, *Angewandte Chemie International Edition*, 1999, 38, 428-447.

13. L. Resconi, L. Cavallo, A. Fait and F. Piemontesi, *Chemical Reviews*, 2000, 100, 1253-1345.

14. A. Illanes, *Enzyme Biocatalysis: Principles and Applications*, Springer, 2008.

15. F. Cavani, G. Centi, S. Perathoner and F. Trifiro, *Sustainable Industrial Chemistry: Principles, Tools and Industrial Examples*, Wiley-VCH, 2009.

16. Y. Zhao, L. Deng, S. Y. Tang, D. M. Lai, B. Liao, Y. Fu and Q. X. Guo, *Energy Fuels*, 2011, 25, 3693-3697.

17. G. Rothenberg, *Catalysis: Concepts and Green Applications*, Wiley-VCH, 2008.

18. J. Hagen, *Industrial Catalysis: A Practical Approach*, Wiley-VCH, 2006.

19. H. Knözinger and K. Kochloefl, in *Ullmann's Encyclopedia of Industrial Chemistry*, Wiley-VCH Verlag GmbH & Co. KGaA, 2000, DOI: 10.1002/14356007.a05_313.

20. J. Richardson, *Principles of Catalyst Development*, Springer, 1989.

21. P. Stoltze, *Introduction to Heterogeneous Catalysis*, 1997.

22. A. A. Balandin, in *Advances in Catalysis*, eds. H. P. D.D. Eley and B. W. Paul, Academic Press, 1969, vol. Volume 19, pp. 1-210.

23. M. Boudart, *Chemical Reviews*, 1995, 95, 661-666.

24. A. P. Umpierre, E. de Jesus and J. Dupont, *Chemcatchem*, 2011, 3, 1413-1418.

25. P. Forzatti and L. Lietti, *Catal. Today*, 1999, 52, 165-181.

26. R. B. King, *Encyclopedia of Inorganic Chemistry*, Wiley, 2005.

27. P. Albers, J. Pietsch and S. F. Parker, *Journal of Molecular Catalysis A: Chemical*, 2001, 173, 275-286.

28. S. C. Tsang, N. Cailuo, W. Oduro, A. T. S. Kong, L. Clifton, K. M. K. Yu, B. Thiebaut, J. Cookson and P. Bishop, *ACS Nano*, 2008, 2, 2547-2553.

29. S. Jones, K. Tedsree, M. Sawangphruk, J. S. Foord, J. Fisher, D. Thompsett and S. C. E. Tsang, *Chemcatchem*, 2010, 2, 1089-1095.

30. U. Heiz and U. Landman, *Nanoscience and Technology: Nanocatalysis*, Springer, 2007.

31. I. Langmuir, *Transactions of the Faraday Society*, 1922, 17, 607-620.

32. http://www.platinum.matthey.com/prices/price-charts).

33. B. Hvolbaek, T. V. W. Janssens, B. S. Clausen, H. Falsig, C. H. Christensen and J. K. Norskov, *Nano Today*, 2007, 2, 14-18.

34. A. Visikovskiy, H. Matsumoto, K. Mitsuhara, T. Nakada, T. Akita and Y. Kido, *Physical Review B*, 2011, 83, 9.

35. B. Corain, G. Schmid and N. Toshima, *Metal Nanoclusters in Catalysis and Material Science: The Issue of Size Control*, Elsevier, 2008.

36. K. W. Kolasinski, *Surface Science: Foundations of Catalysis and Nanoscience*, Wiley, 2008.

37. B. Hammer and J. K. Nørskov, in *Advances in Catalysis*, Academic Press, 2000, vol. Volume 45, pp. 71-129.

38. B. Hammer and J. K. Norskov, *Nature*, 1995, 376, 238-240.

39. A. Nilsson, L. G. M. Pettersson, B. Hammer, T. Bligaard, C. H. Christensen and J. K. Norskov, *Catalysis Letters*, 2005, 100, 111-114.

40. J. K. Norskov, *Prog. Surf. Sci.*, 1991, 38, 103-144.

41. B. Hammer, Y. Morikawa and J. K. Norskov, *Phys. Rev. Lett.*, 1996, 76, 2141-2144.

42. J. R. Kitchin, J. K. Norskov, M. A. Barteau and J. G. Chen, *Phys. Rev. Lett.*, 2004, 93, 156801.

43. C. W. A. Chan, A. H. Mahadi, M. M. J. Li, E. C. Corbos, C. Tang, G. Jones, W. C. H. Kuo, J. Cookson, C. M. Brown, P. T. Bishop and S. C. E. Tsang, *Nat. Commun.*, 2014, 5, 9.

44. N. Acerbi, S. C. E. Tsang, G. Jones, S. Golunski and P. Collier, *Angewandte Chemie (International ed. in English)*, 2013, 52, 7737-7741.

45. K. Tedsree, C. W. A. Chan, S. Jones, Q. A. Cuan, W. K. Li, X. Q. Gong and S. C. E. Tsang, *Science*, 2011, 332, 224-228.

46. K. Tedsree, T. Li, S. Jones, C. W. A. Chan, K. M. K. Yu, P. A. J. Bagot, E. A. Marquis, G. D. W. Smith and S. C. E. Tsang, *Nat Nano*, 2011, 6, 302-307.

47. W.-J. Shen, M. Okumura, Y. Matsumura and M. Haruta, *Applied Catalysis A: General*, 2001, 213, 225-232.

48. Y. Li and W. J. Shen, *Chemical Society Reviews*, 43, 1543-1574.

49. K. A. Matori, L. C. Wah, M. Hashim, I. Ismail and M. H. M. Zaid, *International Journal of Molecular Sciences*, 2012, 13, 16812-16821.

50. C. M. Y. Yeung, K. M. K. Yu, Q. J. Fu, D. Thompsett, M. I. Petch and S. C. Tsang, *Journal of the American Chemical Society*, 2005, 127, 18010-18011.

51. X. Du, D. Zhang, L. Shi, R. Gao and J. Zhang, *The Journal of Physical Chemistry C*, 2012, 116, 10009-10016.

52. A. Trovarelli, *Catalysis Reviews*, 1996, 38, 439-520.

53. S. J. Tauster, S. C. Fung and R. L. Garten, *Journal of the American Chemical Society*, 1978, 100, 170-175.

54. C. Sun, H. Li and L. Chen, *Energy & Environmental Science*, 2012, 5, 8475-8475.

55. S. Bernal, J. J. Calvino, M. A. Cauqui, J. M. Gatica, C. Larese, J. A. P. Omil and J. M. Pintado, *Catal. Today*, 1999, 50, 175-206.

56. A. Trovarelli, *Comments on Inorganic Chemistry*, 1999, 20, 263-284.

57. J. Kašpar, P. Fornasiero and M. Graziani, *Catal. Today*, 1999, 50, 285-298.

58. A. Trovarelli, C. de Leitenburg, M. Boaro and G. Dolcetti, *Catal. Today*, 1999, 50, 353-367.

59. K. Zhou, X. Wang, X. Sun, Q. Peng and Y. Li, *Journal of Catalysis*, 2005, 229, 206-212.

60. C. Pan, D. Zhang and L. Shi, *Journal of Solid State Chemistry*, 2008, 181, 1298-1306.

61. X. Wang, Z. Jiang, B. Zheng, Z. Xie and L. Zheng, *Crystengcomm*, 2012, 14, 7579-7579.

62. W.-Q. Han, W. Wen, J. C. Hanson, X. Teng, N. Marinkovic and J. A. Rodrguez, *The Journal of Physical Chemistry C*, 2009, 113, 21949-21955.

63. Q. Fu, A. Weber and M. Flytzani-Stephanopoulos, *Catalysis Letters*, 2001, 77, 87-95.

64. H. J. Beie and A. Gnorich, *Sensors and Actuators B-Chemical*, 1991, 4, 393-399.

65. P. Jasinski, T. Suzuki and H. U. Anderson, *Sensors and Actuators B-Chemical*, 2003, 95, 73-77.

66. S. Molin, M. Gazda, P. Jasinski and A. Nowakowski, *Elektronika*, 2008, 49, 253-254, 223.

67. B. C. H. Steele, *Solid State Ion.*, 2000, 129, 95-110.

68. H. Kim, S. Park, J. M. Vohs and R. J. Gorte, *Journal of the Electrochemical Society*, 2001, 148, A693-A695.

69. C. Sun, R. Hui and J. Roller, *Journal of Solid State Electrochemistry*, 2010, 14, 1125-1144.

70. E. Aneggi, C. de Leitenburg and A. Trovarelli, *Catal. Today*, 2012, 181, 108-115.

71. A. Trovarelli, M. Boaro, E. Rocchini, C. de Leitenburg and G. Dolcetti, *J. Alloy. Compd.*, 2001, 323-324, 584-591.

72. D. R. Mullins, *Surface Science Reports*, 2015, 70, 42-85.

73. L. Eyring, in *Handbook on the Physics and Chemistry of Rare Earths*, Elsevier, 1979, vol. Volume 3, pp. 337-399.

74. J. Zhang, Z. C. Kang and L. Eyring, *J. Alloy. Compd.*, 1993, 192, 57-63.

75. J. C. Conesa, *Surface Science*, 1995, 339, 337-352.

76. M. Nolan, S. Grigoleit, D. C. Sayle, S. C. Parker and G. W. Watson, *Surface Science*, 2005, 576, 217-229.

77. D. C. Sayle, S. A. Maicaneanu and G. W. Watson, *Journal of the American …*, 2002, 124, 11429-11439.

78. T. X. T. Sayle, S. C. Parker and C. R. a. Catlow, *Surface Science*, 1994, 316, 329-336.

79. G. Wulff, *Kristallogr. Mineral.*, 1901, 34, 363-364.

80. K. Zhou and Y. Li, *Angewandte Chemie - International Edition*, 2012, 51, 602-613.

81. Y. Li and W. Shen, *Science China Chemistry*, 2012, 55, 2485-2496.

82. Y. Li and W. Shen, *Morphology-dependent nanocatalysts: Rod-shaped oxides*, 2014.

83. S. Chowdhury and K.-S. Lin, *Materials Chemistry and Physics*, 2012, 133, 163-169.

84. W.-I. Hsiao, Y.-S. Lin, Y.-C. Chen and C.-S. Lee, *Chemical Physics Letters*, 2007, 441, 294-299.

85. W.-Q. Han, W. Wen, J. C. Hanson, X. Teng, N. Marinkovic and J. A. Rodriguez, *J. Phys. Chem. C*, 2009, 113, 21949-21955.

86. S. Agarwal, L. Lefferts, B. L. Mojet, D. a. J. M. Ligthart, E. J. M. Hensen, D. R. G. Mitchell, W. J. Erasmus, B. G. Anderson, E. J. Olivier, J. H. Neethling and A. K. Datye, *ChemSusChem*, 2013, 6, 1898-1906.

87. Y. Guan, D. a. J. M. Ligthart, Ö. Pirgon-Galin, J. a. Z. Pieterse, R. a. Van Santen and E. J. M. Hensen, *Topics in Catalysis*, 2011, 54, 424-438.

88. D. Zhang, C. Zhang, Y. Chen, Q. Wang, L. Bian and J. Miao, *Electrochimica Acta*, 2014, 139, 42-47.

89. J. Y. Luo, M. Meng, H. Xian, Y. B. Tu, X. G. Li and T. Ding, *Catalysis Letters*, 2009, 133, 328-333.

90. Y. Gao, W. Wang, S. Chang and W. Huang, *ChemCatChem*, 2013, 5, 3610-3620.

91. F. L. Liao, Y. Q. Huang, J. W. Ge, W. R. Zheng, K. Tedsree, P. Collier, X. L. Hong and S. C. Tsang, *Angew. Chem.-Int. Edit.*, 50, 2162-2165.

2 Analytical Techniques

Contents

2.1 Introduction

The characterisation of catalysts plays a major role in understanding the chemistry that brings out their catalytic properties. In the early years of heterogeneous catalysis study was known as the "black art" due to lack of characterisation techniques at nano-sized resolutions[1]. As most catalysts consist of small nanoparticles, the lack of characterisation techniques made it difficult to identify the nature of the catalyst material and to explain the occurrences of a working catalyst. However, the development of new characterisation techniques has led to exceptional progress in the heterogeneous catalysis field.

Currently, a wide variety of characterisation techniques which are based on diffraction, spectroscopy, microscopy and thermal methods are available to provide the information in order to gain more understanding of a catalyst system. For example, with the help of electron microscopy coupled with energy electron loss spectroscopy (EELS), the elemental composition of the catalyst can be revolved in the atomic scale.

Characterisation methods are generally classified into bulk or surface techniques. Bulk techniques such as x-ray diffraction provide information on the properties of the catalyst as a whole, whilst surface techniques are usually limited to a few layers of the surface of the catalyst. However, since most active sites of the catalyst are situated on the surface, surface techniques can provide crucial information on the workings of a catalyst.

2.2 X-ray Diffraction (XRD)

X-ray diffraction is one of the most commonly used techniques for nanoparticles catalyst characterisation. It is a bulk technique that provides information on the composition, crystal

structure and the crystallite size of the nanoparticles[2]. XRD employs the scattering of x-rays by the structure of an ordered material with an atomic spacing similar to the incident x-ray wavelength.

Typically, the incident x-rays are generated by bombarding Cu with high-energy electrons produced from a tungsten filament at high voltage, resulting in the ejection of its electrons (typically from the K shell). Electrons from higher level shells then undergo a transition to fill the empty electron holes, resulting in the generation of an x-ray spectrum. The x-ray spectrum is subjected to a collimator and a monochromator to focus and filter the spectrum producing an x-ray beam with a specific wavelength.

When the incident x-ray is focussed into a solid sample consisting of ordered crystallographic planes, the x-ray is diffracted creating constructive and destructive interferences (Figure 2.1). In a typical x-ray diffractometer, the diffraction pattern is obtained by moving the x-ray detector over a wide range of angles. The relationship between the constructive interferences and the interplanar spacings of the sample crystal lattice is expressed by the Bragg's Law (Equation 2.1).

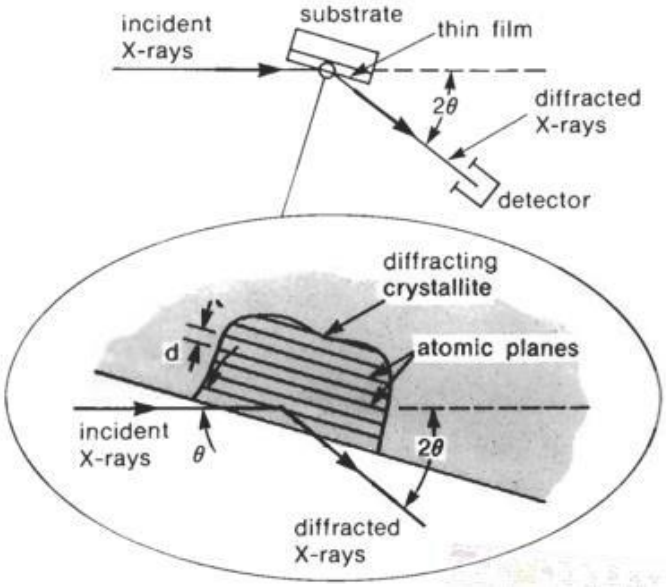

Figure 2.1 A schematic of XRD instrument depicting the diffraction of x-rays by sample consisting of ordered crystallographic planes[3].

$$n\lambda = 2d \sin\theta \qquad \text{Equation 2.1}$$

where *n* is an integer representing the order of diffraction, λ is the wavelength of incident x-ray, *d* is the interplanar spacing and θ is the diffraction angle, which is also referred to as Bragg angle. The diffraction pattern can be used as a fingerprint to identify known crystal structures, through comparison of their peak positions and intensities. For a cubic crystal structure, the d spacing is related to its lattice parameter by Equation 2.2.

$$\frac{1}{d^2} = \frac{h^2+k^2+l^2}{a^2} \qquad \text{Equation 2.2}$$

where *d* is the interplanar spacing, *h*, *k* and *l* are the Miller indices of the Bragg plane and *a* is the lattice parameter.

When the sample consists of an extended crystal structure with long range ordering, the constructive interference occur only at the Bragg angles while all other angles experience destructive interference, thus producing an XRD pattern with sharp peaks. However, when long range ordering is absent, in the case of nanoparticles, the constructive and destructive interferences became less pronounced which leads to peak broadening. The degree of broadening is related to the particle size, hence the mean particle size of nanoparticles sample can be calculated using the Scherrer equation (Equation 2.3)

$$L = \frac{K\lambda}{\beta \cos\theta} \qquad \text{Equation 2.3}$$

where L is the volume weight average crystallite size of the particles, λ is the incident x-ray wavelength, β is the peak width at half maximum peak intensity, θ is the Bragg angle and K is the shape factor (normally 1).

2.3 Electron Microscopy

Electron microscopy uses a beam of high energy electrons to produce high resolution images of a sample. It works similarly to an optical microscope, except instead of visible light, electron microscopy utilises electrons which have a small de Broglie wavelength. The use of high energy electrons with a wavelength below 1 Å allows a resolution of up to 0.1 nm, which is a magnification of up to 10^6 times of the original sample. Hence, electron microscopy is an ideal technique to characterise nanoparticles, as it provides direct imaging of the nanoparticles, resulting in information on their particle size and morphology. The advances in electron microscopy have led to the development of 3 types of electron microscope[3]:

- Transmission electron microscope (TEM)
- Scanning electron microscope (SEM)
- Scanning transmission electron microscope (STEM)

An electron microscope typically consist of an illumination system, magnification system, objective lens system, sample stage and image analysis system (Figure 2.2). The illumination system contains an electron gun to generate a beam of electrons by passing a current through a tungsten filament or LaB_6 crystal and at least one electromagnetic condenser lens to convert the electron beam into parallel rays of electrons. High-angle electrons is also filtered out using a condenser aperture. The electrons are then focussed through a thin-film sample, usually less than 200 nm thick. In the TEM system, the electrons are transmitted through the sample and projected to a screen where the image is displayed. The data can be recorded by replacing this screen with a charge-coupled device (CCD) camera. In SEM system, the electrons interact with the sample resulting in the emission of secondary electrons which are captured by a detector and used to create an image. In both cases, objective lenses and aperture are usually fitted before the electrons reach the detector to focus and filter them further thus enhancing the resolution of the image. STEM on the other hand combines both TEM and SEM which allows it to detect both transmitted electrons and secondary electrons.

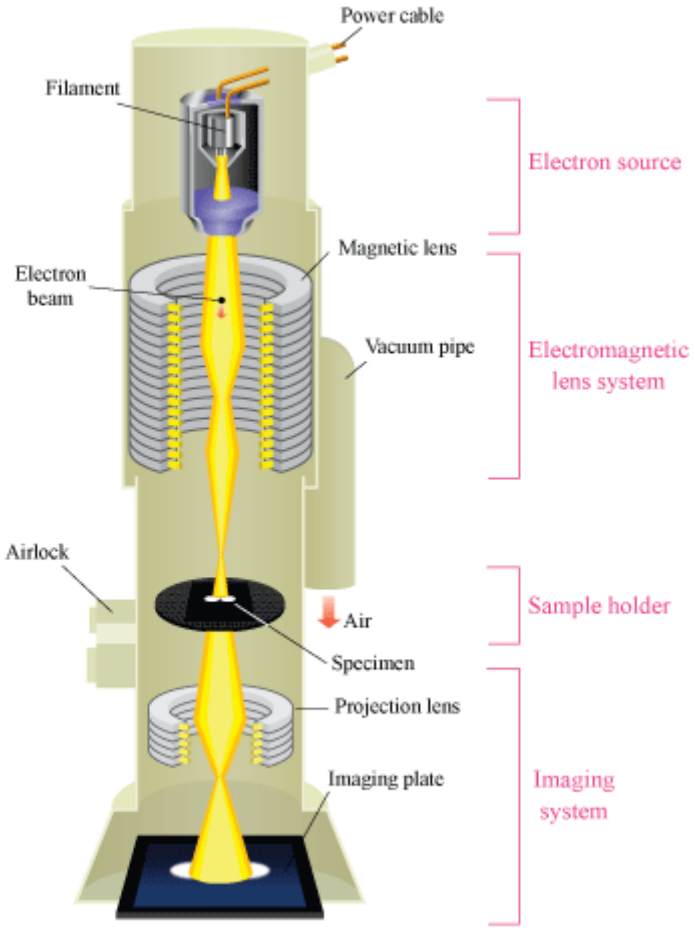

Figure 2.2 A schematic of a TEM instrument[4].

In TEM, the image created by the transmitted electrons is a bright field image where areas rich in sample appear dark due to the scattering of electrons and vice versa. The scattering of the electrons depends on the atomic number of the atom. Heavier atoms with large nuclei scatter more electrons, resulting in darker regions compared to lighter atoms. This is referred to as Z-contrast. In contrary, an SEM image is produced by secondary electrons resulting in dark field image, where the contrast of the image is reversed as opposed to bright field image. Bright field and dark field imaging can be used in parallel to clarify the composition of complex samples with multiple elements.

2.4 Energy Dispersive X-ray Spectroscopy (EDX)

Energy Dispersive X-ray Spectroscopy (EDX) is a technique for elemental analysis used in conjunction with electron microscopy, in particular TEM and STEM. This technique is not only capable of qualitatively and quantitatively determining the surface elemental composition of a sample, it also provides the position of the elements present.

In electron microscopy, when the sample is exposed to a beam of electrons, a range of possible interactions can occur (Figure 2.3). One possibility is the beam of electrons may excite an electron from an inner shell of the surface atom, causing it to be ejected and creating an electron hole. An electron from a higher energy outer shell can then fill this hole and the difference in energy between the outer shell and the inner shell may be released in the form of x-ray. The energy of the x-ray emitted is a distinctive characteristic of a specific element, hence different elements could be differentiated. In EDX, the energy spectrum of the x-rays emitted from the sample is compared with the spectral database, where the qualitative elemental composition of the focussed area of the sample can be determined. The quantitative analysis is obtained by monitoring the counts of energy-specific charge/voltage pulses on the detector.

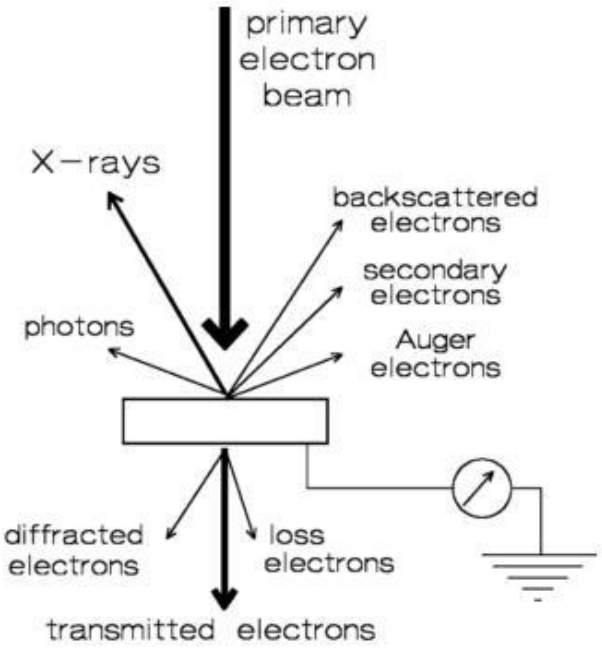

Figure 2.3 The possible interactions of beam of electrons when projected to a thin sample[5].

2.5 Electron Energy Loss Spectroscopy (EELS)

Similar to EDX, electron energy loss spectroscopy (EELS) is a characterisation technique coupled with electron microscopy, used to determine the positional elemental composition of the sample. However, EELS utilises the kinetic energy of the scattered electrons to determine the elements present in a sample. As mentioned in the previous section, a number of events can occur when a beam of electrons is focussed onto the sample. The incident electrons can be scattered elastically, where the kinetic energy is conserved or inelastically, where the electrons loses its kinetic energy through interaction such as inner shell ionisation. In EELS, the energy loss is measured by an electron spectrometer producing the electron energy loss spectrum. The energy loss of the incident electrons is specific to each element and also its oxidation state, thus EELS not only provides information on the elements present in the sample, but also the oxidation state of these elements. This is because the energy loss is the product of primary

interactions of the incident electrons, whereas the x-ray produces is the consequence of the initial energy loss which is termed secondary interaction, thus more information is retained in EELS compared to EDX.

2.6 X-ray Photoelectron Spectroscopy (XPS)

X-ray photoelectron spectroscopy (XPS) is a surface sensitive characterisation technique to identify the elemental composition of a surface and also the electronic state of the surface atoms, thus the oxidation state of the elements can be differentiated[2]. The surface sensitivity of XPS makes it an invaluable characterisation technique for catalysts as most of the reactions involved in solid catalysis occur on the surface. The importance of XPS was marked when Kai Siegbahn was awarded the Nobel Prize in Physics in 1981 for developing the technique.

In XPS, x-rays are used to excite an electron from a core shell of the surface atom, resulting in the ejection of the electron, referred to as 'photoemission' (Figure 2.4). The kinetic energy of the photoemitted electron is measured and it is related to its binding energy (Equation 2.4), which corresponds to specific orbitals of a particular element.

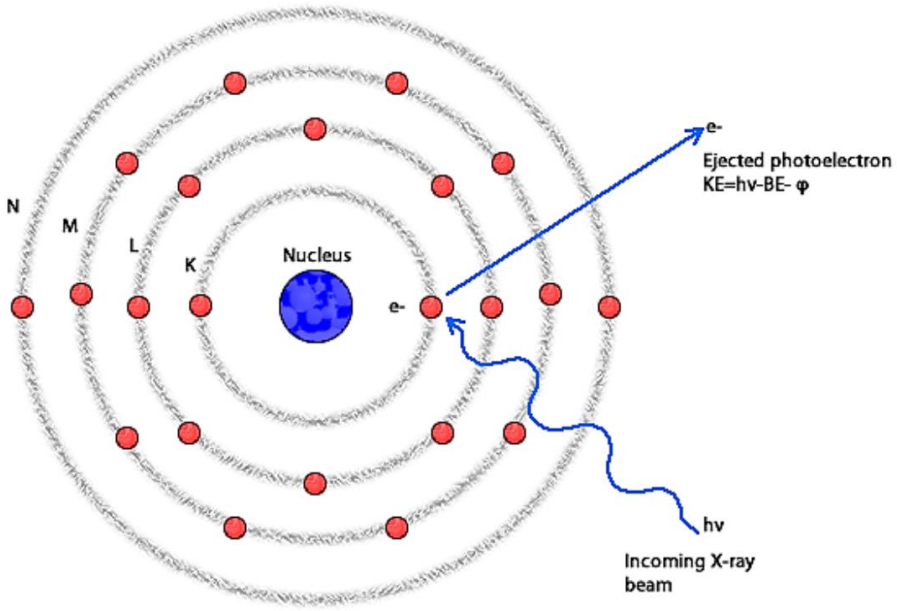

Figure 2.4 The photoemission process of an electron upon excitation by x-ray beam[6].

$$E_k = hv - E_b - \varphi \qquad \text{Equation 2.4}$$

where E_k is the kinetic energy of the photoemitted electron, h is the Planck's constant, v is the frequency of the incident x-ray, E_b is the binding energy of the photoemitted electron and φ is the work function of the spectrometer. The kinetic energy of the photoemitted electron is relatively low, hence the photoemitted electrons from the bulk atoms have insufficient energy to escape due to inelastic collisions with the atoms in the sample, resulting in the shallow sampling depth of XPS. The x-ray source for XPS is generated similarly to XRD, with the exception that Al or Mg is typically used instead of Cu as a source of x-ray resulting in radiation of much lower energy.

Because XPS is a surface sensitive technique, ultra-high vacuum (UHV) is usually required to avoid contamination of the surface. However, ambient pressure XPS have been recently

developed which allows XPS measurements to be performed in *operando* using low pressure of a desired gas[7].

2.7 Gas Chromatography (GC)

Gas chromatography (GC) is an analytical method which makes use of the separation of mixtures of gases and volatile compounds. In a gaseous continuous flow reactor for catalyst testing, GC is often used to analyse the gas outlet so that the reactants and the products can be identified and quantified with high precision and sensitivity.

GC applies the principle that different components of a mixture travel across a stationary phase at different rates under the influence of a mobile phase. The mobile phase is usually an inert carrier gas (N_2 or He) that transports the sample mixture through a column containing a stationary phase, consisting of microscopic layer of liquid or polymer on an inert solid support. The gaseous mixture interact with this stationary phase resulting each component being eluted at a different time, known as the retention time. The retention time of the components can be varied and optimised by changing the type, temperature and length of the column, the length of the column and the gas flow of the carrier gas. A detector is used to monitor the outlet gas after the sample gas mixture is passed through the column, thus providing the retention time and the amount of each gas present in the sample.

The most commonly used detectors for GC are the flame ionisation detector (FID) and the thermal conductivity detector (TCD). FID utilises electrodes placed adjacent to a flame fuelled by H_2/air mixture. The flame is used to pyrolyse any organic or hydrocarbon components present in the gaseous sample mixture, which creates cations and electrons that generates a

current between the electrodes. This results in a peak signal in the chromatogram, where the peak area corresponds to the concentration of the component in the gaseous mixture. However, FID is limited to the detection of organic and hydrocarbon components only. On the other hand, TCD works by using a filament to monitor the changes in thermal conductivity of the gas outlet in reference to the carrier gas. Since all atoms or molecules have different thermal conductivities compared to the typical carrier gas (N_2 or He), a TCD can be used to detect any component other than the carrier gas. Some TCD use two carrier gases so that all components can be detected.

2.8 Pulse Chemisorption

Pulse chemisorption is a characterisation technique used to measure the surface area of a catalyst. As most catalyst reactions occur on the surface of the catalyst, the quantification of its surface area is crucial and it is needed for calculations of catalyst efficiency, such as turnover frequency (TOF). Depending on the pulse gas used for the chemisorption, surface area of different parts of the catalyst can be determined. Using adsorbate gas that can bind to both metal and support of the catalyst such as N_2 allows determination of the total surface area of the catalyst, whereas adsorbate gases such as CO and H_2 are usually used to selectively bind to the metal surface, hence providing the surface area of the supported metal nanoparticles (active surface area). For the metal selective gas adsorbates, other than the active surface area, the metal dispersion and the particle size of the metal particles can also be calculated.

In a typical pulse chemisorption instrument, an inert carrier gas (typically He) is flowed through a sample packed-bed and pulses of a known volume of adsorbate gas is injected into the carrier gas stream until the surface of the sample is saturated with the adsorbate gas. The gas outlet is

monitored by a thermal conductivity detector (TCD) where the volume of gas adsorbed by the sample can be obtained by analysing the peak area of the pulse signals (Figure 2.5a). Generally, the peak areas of the 6th pulse onwards are used as a reference, as the gas adsorption by the sample from those pulses are regarded negligible (Figure 2.5b), hence the peak area corresponds to the known injected volume of the adsorbate gas.

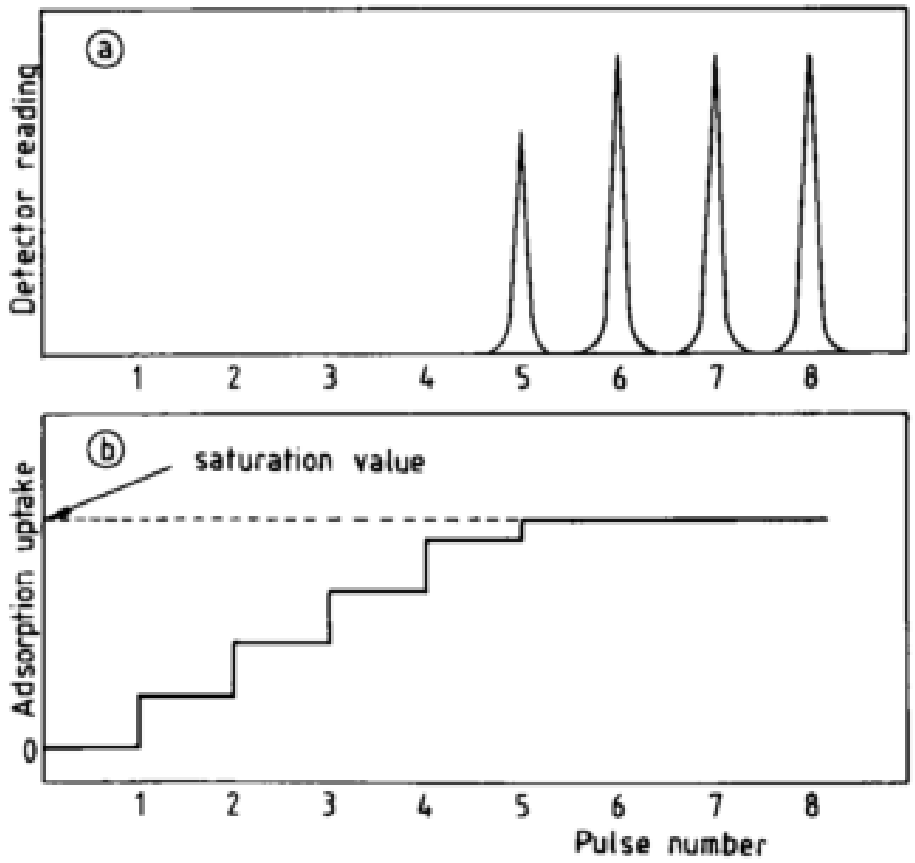

Figure 2.5 a) A typical profile of pulse chemisorption. b) The corresponding uptake of adsorbed gas in reference to the saturation value[8].

For a CO chemisorption, the metal dispersion, active surface area and metal particle size can be calculated using the following equations:

$$V_{chem} = \frac{V_{ads}}{24.7895} \div m \qquad \text{Equation 2.5}$$

$$\text{Metal dispersion (\%)} = \frac{V_{chem} \cdot \text{SF} \cdot \text{MW}}{c/_{100}} \times 100 \qquad \text{Equation 2.6}$$

$$\text{Metal surface area (per 1 g catalyst)},\ \text{A}_\text{c}(\text{m}^2/\text{g}) = V_{chem} \cdot \text{N}_\text{A} \cdot \text{SF} \cdot \sigma_m \cdot 10^{-18}$$

Equation 2.7

$$\text{Metal surface area (per 1 g metal)}, \text{A}_\text{m}(\text{m}^2/\text{g}) = \frac{\text{A}_\text{c}}{c/_{100}}$$

Equation 2.8

$$\text{Mean particle diameter}, \text{S}_\text{m}(\text{nm}) = \frac{6c}{\text{A}_\text{c} \times 100 \times \rho \times 10^6} \times 10^9$$

Equation 2.9

where V_{chem} is the of number of moles of adsorbed gas per 1 g of sample (mol g^{-1}), V_{ads} is the volume of adsorbed gas (l), m is the mass of sample (g), SF is the stoichiometry factor, MW is the atomic weight of the supported metal (g), c is the percentage weight of supported metal, NA is the Avogadro's number, σ_m is the supported metal cross section area (nm^2) and ρ is the supported metal density (g cm^{-3}). For CO chemisorption on supported Pd samples, SF is 1, σ_m is 0.0787 nm^2 and ρ is 12.023 g cm^3.

2.9 Temperature Programmed Reduction (TPR)

Temperature programmed reduction is used to determine the thermodynamic properties of a solid catalyst under reducing conditions. This characterisation technique provides information on the types of reducible species present in a catalyst and the temperatures at which they occur,

giving an indication of their reduction activation energies. It can also be used to determine the oxygen vacancy formation tempearture of a catalyst, especially when the catalyst involves metal oxides. In samples with variable oxidation state, TPR can be used to evaluate the temperature of the change in oxidation state.

TPR consists of passing a continuous gas stream of H_2 or H_2 mixed with an inert gas, through a quartz reactor tube containing the sample packed-bed and into a detector to analyse the gas outlet. The quartz reactor is placed in a temperature controlled furnace where the temperature of the sample is programmed based on the rate of increase in temperature (ramp) and the initial and final temperatures at which the TPR measurements are performed. For an accurate TPR measurement, the sample is usually pretreated with an inert gas at a specific temperature to remove any surface contaminants.

A TCD detector is usually used to monitor the gas outlet, where a change in concentration of H_2 in reference to the H_2 gas supply would give a signal peak. In the case of H_2 uptake, the TCD gives a positive peak whereas evolution of H_2 from the sample results in a negative peak.

2.10 Electron Paramagnetic Resonance Spectroscopy (EPR)

Electron paramagnetic resonance is a technique used to study materials with unpaired electrons[2]. Although most applications of EPR are to study the unpaired electrons in organic and inorganic radical and transition metal complex systems, it can also be used to determine the presence of oxygen vacancies in a catalyst material. Upon formation of an oxygen vacancy, the O_2^- superoxide radical is given off as O_2, leaving a trapped unpaired electron in the oxygen vacancy, which results in an EPR signal.

EPR employs the excitation of electrons by an external magnetic field which causes the electron's magnetic moment to align itself in either parallel ($m_s = -\frac{1}{2}$) or anti-parallel ($m_s = +\frac{1}{2}$) to the field, resulting in two possible energy states (Figure 2.6). This effect is referred to as Zeeman splitting and the energy difference between the two states is given by Equation 2.10. As the intensity of the applied magnetic field increases, the energy difference between the two states increases until it resonates with the applied microwave radiation, leading to absorption of photons, giving the EPR signal.

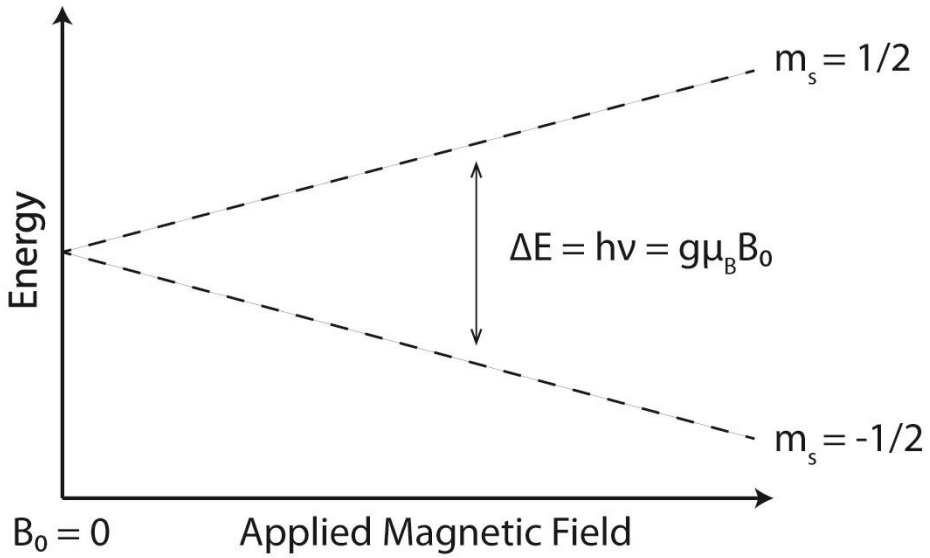

Figure 2.6 The splitting of electron's magnetic moment known as Zeeman splitting[9].

$$\Delta E = h\nu = g\mu_B B_0 \qquad \text{Equation 2.10}$$

where h is the Planck's constant, ν is the frequency of the microwave radiation, g is the g-factor, μ_B is the Bohr magneton and B_0 is the applied magnetic field.

2.11 Mass spectrometry (MS)

Mass spectrometry is an analytical technique to identify and quantify the chemicals present in a sample[2]. This is done by ionising the chemicals of the sample into charged ion fragments by bombarding them with electrons, and accelerating the charged ions with an electric field (Figure 2.7). They are also subjected to a magnetic field that causes the ions to be deflected and the degree of deflection depends on the mass-to-charge ratio of the ions, where fragments with higher mass-to-charge ratio experiences less deflection. Hence, this enables the separation of the different fragments. An extraction system then removes the deflected ions and subjects them to a mass analyser to 'sort' the fragments by their charge-to-mass ratio, based on their degree of deflection and finally to a detector, typically an electron multiplier to produce a signal on the MS. Since MS uses the basis of charge-to-mass ratio of the fragments, it can be used to differentiate different isotopes of an element.

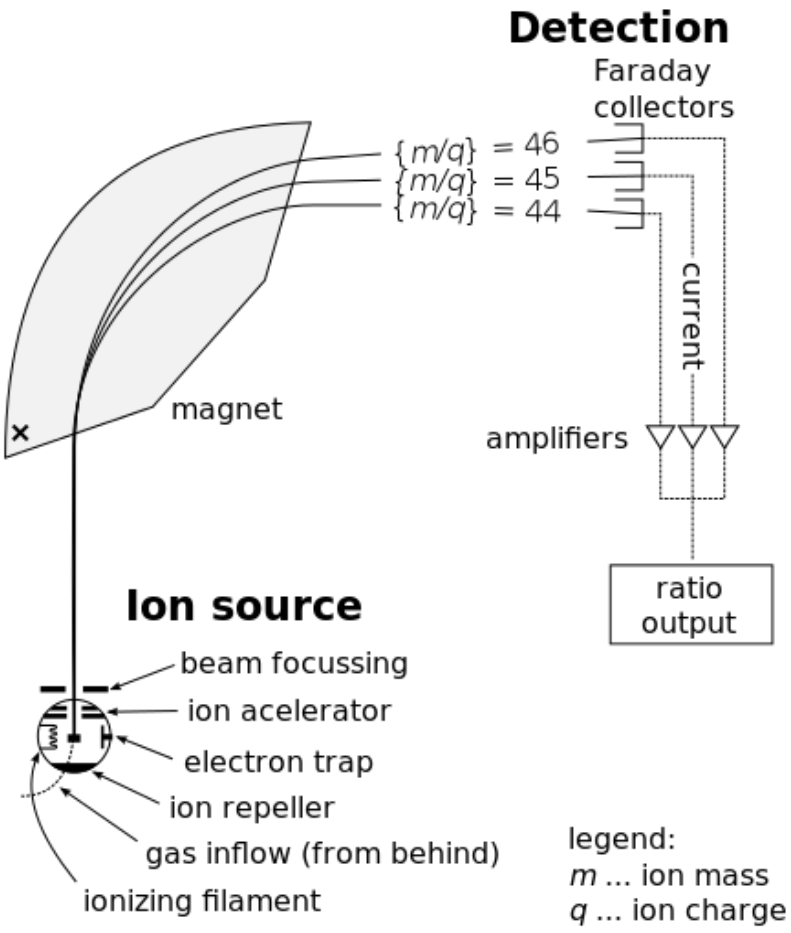

Figure 2.7 A schematic of a MS instrument showing different degree of deflection of components with different change-to-mass ratio[10].

2.12 Pulse Isotopic Exchange (PIE)

The Pulse Isotopic Exchange (PIE) is a technique used to determine the surface exchange rate of an oxide material to investigate its oxygen mobility properties[11]. It is achieved by pulsing known amounts of labelled $^{18}O_2$ isotope through a packed-bed of sample, which is in equilibrium with an O_2-containing carrier gas (Figure 2.8). The gas outlet is analysed by MS to monitor the labelled $^{18}O_2$ uptake and exchanged $^{16}O^{18}O$ gas. The measurements are taken at various temperatures, hence the activation energy of surface oxygen exchange can be derived.

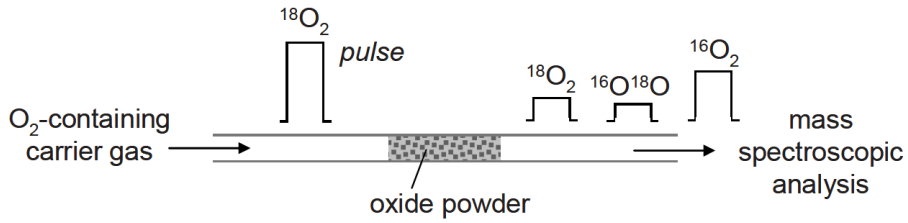

Figure 2.8 A schematic of pulse isotopic oxygen exchange experiment[11].

The peak areas of $^{18}O_2$ and $^{16}O^{18}O$ are used to calculate the mole fraction of ^{18}O, so that the rate of surface oxygen exchange can be derived using the following equations:

$$f_{g,o}^{18} = f_{g,o}^{36} + 0.5 f_{g,o}^{34} = {A_{g,o}^{36}}/{A_{g,o}^{Ne}} + 0.5\,{A_{g,o}^{34}}/{A_{g,o}^{Ne}} \quad \text{Equation 2.11}$$

$$f_{g,i}^{18} = f_{g,o}^{18}(60°\text{C}) = {A_{g,o}^{36}(60°\text{C})}/{A_{g,o}^{Ne}(60°\text{C})} + 0.5\,{A_{g,o}^{34}(60°\text{C})}/{A_{g,o}^{Ne}(60°\text{C})}$$

Equation 2.12

where $f_{g,o}^{18}$ is the mole fraction of ^{18}O at the gas outlet, $f_{g,o}^{36}$ and $A_{g,o}^{36}$are the mole fraction and peak area respectively of the $^{18}O_2$ at the gas outlet, $f_{g,o}^{34}$ and $A_{g,o}^{34}$ are the mole fraction and peak area respectively of the $^{16}O^{18}O$ at the gas outlet, $A_{g,o}^{Ne}$ is the peak area of Ne gas at the outlet, which is used as an internal standard. The mole fraction of ^{18}O at the gas inlet, $f_{g,i}^{18}$ is given by mole fraction of ^{18}O at the gas outlet when the pulse measurement is performed at 60 °C, as it is assumed that at that temperature, there is no oxygen exchange between the labelled $^{18}O_2$ and the surface of the sample. With $f_{g,o}^{18}$ and $f_{g,i}^{18}$, the rate of surface oxygen exchange can be calculated with Equation 2.13.

$$R_o = -\frac{2p\mathrm{O}_2}{\mathrm{R}S_r} \cdot \frac{F}{T} \ln\left(\frac{f_{g,o}^{18}}{f_{g,i}^{18}}\right) \qquad \text{Equation 2.13}$$

where R_o is the surface exchange rate (mol O m^{-1} s), $p\mathrm{O}_2$ is the partial pressure of oxygen, R is the gas constant, S_r is the surface area of the oxide sample, F is the gas flow rate and T is the temperature.

2.13 References

1. R. C. Jin, *Nanotechnology Reviews*, 2012, **1**, 31-56.
2. D. Shriver and P. Atkins, *Inorganic Chemistry*, Oxford University Press, 4th edn., 2006.
3. C. R. Brundle, C. A. Evans Jr. and S. Wilson, *Encyclopedia of Materials Characterization*, Butterworth-Heinemann, 1992.
4. http://www.hk-phy.org/atomic_world/tem/tem02_e.html).
5. J. W. Niemantsverdriet, *Spectroscopy in Catalysis: An Introduction*, Wiley-VCH, 2007.
6. https://wiki.utep.edu/pages/viewpage.action?pageId=51217144).
7. F. Tao, *Chemical Communications*, 2012, **48**, 3812-3814.
8. J. L. G. Fierro, *Spectroscopic Characterizaton of Heterogeneous Catalysts - Chemisorption of Probe Molecules*, Elsevier, 1990.
9. http://chemwiki.ucdavis.edu/Physical_Chemistry/Spectroscopy/Magnetic_Resonance_Spectroscopies/Electron_Paramagnetic_Resonance/EPR%3A_Theory).
10. K. M. Revesz and J. M. Landwehr, *Rapid communications in mass spectrometry : RCM*, 2002, **16**, 2102-2114.
11. H. J. M. Bouwmeester, C. Song, J. Zhu, J. Yi, M. van Sint Annaland and B. A. Boukamp, *Physical Chemistry Chemical Physics*, 2009, **11**, 9640-9643.

3 Experimental Methods

Contents

3.1 Syntheses

3.1.1 Ceria morphologies

The ceria morphologies were synthesised using surfactant-free hydrothermal method based on the methods used by Mai *et. al.* and Zhou *et. al.*[1, 2]. In a 50 ml beaker, 0.744 mg of $Ce(NO_3)_3.6H_2O$ was added to 30 ml of 6M NaOH solution in DI water. The mixtures were stirred vigorously for 30 minutes to allow the formation of $Ce(OH)_3$ precipitate, where the precipitate turned into light purple. The precipitate mixture was then transferred to Teflon-lined stainless steel digestion bomb. The digestion bomb was placed in a preheated oven where the precipitate mixture was subjected to hydrothermal treatment. Ceria rods and cubes were obtained by hydrothermal treatment at 100 °C and 180 °C, respectively for 24 hours. Following the hydrothermal treatment, the digestion bomb was left to cool to room temperature before filtering the ceria morphologies product. The product was washed with 1 L of DI water under filtration to ensure that the excess NaOH was washed off completely. Finally the product was dried under a stream of N_2 for 24 hours.

3.1.2 Pd deposition

Pd nanoparticles were deposited onto the ceria cubes and rods supports with the deposition-precipitation method. In a 250 mL round-bottomed flask, 5 mg of $Pd(NO_3)_2$ and 198 mg of ceria were added into 40 mL of water. The mixture were stirred and then dispersed under sonication for 1 hour. The mixture was then adjusted to pH 12 by the addition of 0.1 M NaOH to form the $Pd(OH)_2$ precipitate. After that, the flask was sealed and N_2 was bubbled through for 30 minutes to purge the air out. To reduce the Pd^{2+} to Pd^0, the gas was switched from N_2 to

H_2. H_2 gas was kept bubbling into the mixture for 2 hours where the formation of Pd^0 could be observed when the nanoparticles turned black. After the reduction, the gas was switched back to N_2 for 30 minutes. Finally the product was filtered, washed with 1 L of DI water and dried under a stream of N_2 for 24 hours. This product was labelled as 1% Pd/ceria.

3.2 Catalyst Testing

3.2.1 Methane oxidation

The methane oxidation catalyst testing was carried out in a continuous flow reactor operated under atmospheric pressure. The Pd/ceria catalyst was packed in a fixed bed between two layers of quartz wool in a quartz glass tube with internal diameter of 7 mm, where it was placed in a vertical temperature controlled furnace for variation of reaction temperature. CH_4/air/N_2 mixture was pre-mixed with mass flow controllers, then passed through the reactor tube and finally the output gas mixture was fed into GC-Methanator with FID detector for product analysis. The GC was calibrated so the peak areas can be used to calculate the concentration of the gases.

Two conditions of methane oxidation were used; oxygen lean conditions and oxygen rich conditions. Under oxygen lean conditions, methane to oxygen ratio of 8:1 was used. This was achieved by gas mixture of 6.65 % air, 10.64 % CH_4 and 82.71 % N_2 by volume with a total flow rate of 150 mL/min. Under oxygen rich conditions, premixed 0.1% methane in air gas mixture was used, which gave methane to oxygen ratio of 1:200. A flow rate of 30 mL/min was used. For the safety of the reactor, it was ensured that the methane to oxygen ratio was not within the methane explosive limit, which is 5 – 15 % in air. Under lean conditions, the dilution of the reactant gases with N_2 was a precautionary measure.

3.2.1.1 Activation energy

50 mg of Pd/CeO_2 samples were used for both oxygen rich and oxygen lean conditions. The reaction was allowed to settle for 30 minutes at the desired temperature before taking the gas product analysis, where the amount of CH_4, CO_2 and CO were quantified. The temperature of the reaction was varied from room temperature to 350 °C. At each temperature, 3 consecutive consistent readings were taken, where each point was based on the mean value of 3 similar GC readings, to ensure that the reaction has settled after the change in temperature. The performance of the catalysts were expressed by their percentage methane conversion and selectivity of products, where

$$\text{Methane conversion}\ (\%) = \frac{[\mathrm{CH_4}]_{initial} - [\mathrm{CH_4}]_{final}}{[\mathrm{CH_4}]_{initial}} \times 100\%$$

Equation 3.1

$$\text{CO Selectivity}\ (\%) = \frac{[\mathrm{CO}]}{[\mathrm{CO_2}]+[\mathrm{CO}]}$$

Equation 3.2

3.2.1.2 Active Sites limitation

For the active sites limitation test, the reaction was performed at a fixed temperature of 350 °C. The mass of 1% Pd/ceria cubes was varied until the reaction was saturated with the catalyst active sites, indicated by a constant conversion reading upon the increase of catalyst mass. For each catalyst mass, the reaction was allowed to settle for 30 minutes before the gas outlet was taken for GC analysis, where 3 consecutive consistent readings were taken. The percentage methane conversion were also expressed as the rate, where

$$\text{Rate } (s^{-1}) = \text{ number of } CH_4 \text{molecules converted per second}$$

Equation 3.3

3.2.1.3 Deactivation Test

Catalyst deactivation test was performed with a reaction temperature of 350 °C. Under the oxygen rich conditions, 2 mg of catalyst was used whilst 20 mg of catalyst was used under the oxygen lean conditions. In the active sites limitation test, these masses fell under the mass region where the active sites of Pd were limited. The gas outlet was analysed with GC at 10 minutes intervals for 5 hours and another regular intervals after 24 hours. The final percentage conversion was then used to obtain the turnover frequency of the catalyst (TOF), where

$$\text{TOF } (s^{-1}) = \frac{\text{converted } CH_4 \text{ molecules per second}}{\text{surface area } \times \text{Pd loading} \times \text{mass} \times \text{Pd packing density}}$$

Equation 3.4

3.2.2 Gas-Phase Formic Acid Decomposition

The catalytic gas-phase formic acid decomposition test reaction was performed in an atmospheric pressure continuous flow reactor, based on the set up employed by Halawy *et. al.*[3]. N_2 carrier gas with the flow rate of 40 mL/min was bubbled through liquid formic acid in a saturator that was kept isothermal at 5 °C using benzene and dry ice mixture. Based on the formic acid vapour pressure, this resulted in 1.7% of formic acid in N_2, which is composed of 0.42 mL/min of formic acid and 39.58 mL/min of N_2. The reactant mixture was passed through a sample fixed-bed in a quartz glass reactor tube, placed in a temperature controlled furnace

for reaction temperature variation. The gas outlet was flowed through a -15 °C cold trap consisting of ethylene glycol and dry ice mixture before entering the GC-TCD for product analysis, where H_2, CO and CO_2 could be quantified. The GC was calibrated so the concentration of the product gases could be derived from the integrated peak areas obtained from the GC.

3.2.2.1 Activation energy

For the activation energy test, 50 mg of catalyst sample was used and the reaction temperature was varied between room temperature and 150 °C. At each temperature, the reaction was allowed to settle for 30 minutes before the GC sampling, where 3 consecutive consistent GC readings were taken. The performance of the catalysts were expressed by their percentage formic acid conversion, where

$$\text{Formic acid ceonversion } (\%) = \frac{[\text{HCOOH}]_{initial} - [\text{HCOOH}]_{final}}{[\text{HCOOH}]_{initial}} \times 100\% \qquad \text{Equation 3.5}$$

$$\text{CO Selectivity } (\%) = \frac{[\text{CO}]}{[\text{CO}_2]+[\text{CO}]} \qquad \text{Equation 3.6}$$

3.2.2.2 Active Sites Limitation

The active site limitation was carried out with 1% Pd/ceria cubes sample with the reaction temperature of 150 °C. In this test, the mass of the sample was varied until the activity of the catalyst stayed constant upon increasing the sample mass, denoting that the active sites were in

excess. At each mass, 3 consecutive consistent readings of GC was taken. The percentage methane conversion were also expressed as the rate, where

$$\text{Rate } (s^{-1}) = \text{ number of formic acid molecules converted per second}$$

Equation 3.7

3.2.2.3 Deactivation Test

Deactivation test involved using 6 mg of 1% Pd/ceria sample and the reaction was left to run up to 24 hours. Product sampling was done at 15 minutes intervals for the first 150 minutes and after 24 hours of reaction time. The final percentage conversion was then used to obtain the turnover frequency of the catalyst (TOF), where

$$\text{TOF } (s^{-1}) = \frac{\text{converted formic acid molecules per second}}{\text{surface area } \times \text{Pd loading} \times \text{mass} \times \text{Pd packing density}}$$

Equation 3.8

3.3 Characterisation Techniques

3.3.1 X-ray Diffraction (XRD)

Powder XRD patterns were obtained with a PANalytical X'Pert Pro diffractometer operating at 40 kV and 30 mA. The sampling program was ran at 2θ angles between 25° to 75° with 0.004° step size at 15 seconds per step. The sample powder was pressed onto an aluminium sampling plate to ensure an even dispersion and thickness of sample.

3.3.2 Transmission Electron Microscopy (TEM) and Scanning Transmission Electron Microscopy (STEM)

TEM images were taken with JEOL 2010 and JEOL 2000FX for the high resolution images, situated at Begbroke Science Park, Department of Materials. The Jeol 2000FX was operated under the supervision of Dr. Neil Young of Department of Materials, University of Oxford. The STEM-EELS experiments were perfomed by Dr. Simon Fairclough using SuperSTEM at Daresbury, with a collaboration with the Department of Materials, Oxford. All the TEM samples were prepared by sonicating 1 mg of sample in 10 mL of methanol for 30 minutes to disperse the particles. They were then drop casted onto holey carbon coated Cu grid and dried. For the SuperSTEM sample preparation, the sample grids were pre-cleaned by 4 hours backout under vacuum to avoid any contamination. Before running the STEM-EELS measurement, the prepared sample grids were pre-treated by heating them to 140 °C under vacuum.

3.3.3 CO pulse chemisorption

CO pulse chemisorption measurements were carried out using Quantachrome Instruments ChemBET Pulsar TPR/TPD Automated Chemisorption Analyser. In a reactor tube, 20 mg of sample was made into a packed-bed between two quartz wool plugs. Helium was used as a carrier gas with a flow rate of 20 mL/min and 100% CO was used as a titrant gas. The samples was pre-treated under H_2 for 1 hour at various temperatures and then cooled before the CO pulse chemisorption measurements were taken. The CO was pulsed 7 times with a pulse volume of 72 μL. The detector current was set at 150 mA with the attenuation of 1.

3.3.4 Electron Paramagnetic Resonance (EPR)

The EPR measurements were carried out by Dr. Qin Lu with EMXmicro at the CAESR ESR Facility, University of Oxford. 20 mg of sample was used and the powder sample was inserted into the EPR sample tube. The measurements were under microwave frequency of 9.37 GHz.

3.3.5 Temperature Programmed Reduction (TPR)

TPR measurement were performed with Quantachrome Instruments ChemBET Pulsar TPR/TPD Automated Chemisorption Analyser. 20 mg of sample was inserted into a reactor tube to create a packed-bed between 2 quartz wool plugs. The sample was pre-treated by heating in He for 1 hour and then cooled before the TPR measurement was taken. H_2 with a flow rate of 100 mL/min was used as a reducing gas. The TPR measurement was taken at temperatures from room temperature to 1000 °C at a ramping rate of 10 °C/min. The detertor was set at 150 mA with the attenuation of 1.

3.3.6 Ambient Pressure X-ray Photoelectron Spectroscopy (AP-XPS)

AP-XPS measurements were carried out by Dr Junjun Shan, in collaboration with Associate Professor Franklin Tao at University of Notre Dame with their in-house AP-XPS instrument. The sample were first scanned under ultra-high vacuum (UHV). For the reduced conditions, the sample was reduced by 1 Torr H2 gas to 500 °C and then cooled to 100 °C where the XPS measurement was taken. For the oxidised conditions, the sample was then oxidised by 1 Torr of O_2 at 300 °C for 3 hours and cooled to 100 °C before the measurement was taken.

3.3.7 Pulse Isotopic Exchange (PIE)

PIE experiments were performed by Dr. Wei Chen, in collaboration with Professor Ian Metcalfe's group at School of Engineering and Advanced Materials, Newcastle University. The sample was loaded into a packed-bed in a reactor tube with 3 mm in diameter and placed into a temperature-controlled furnace. A gas mixture of 21% O_2 in Ar was flowed through the sample at a flow rate of 20 mL/min. Before the PIE measurements were taken, the sample was heated to 450 °C to remove any surface contaminants and then cooled to 60 °C. The samples were injected with 0.5 mL of pulse gas consisting of 22% $^{18}O_2$, 20% Ne and 58% Ar, where the Ne was used as an internal standard. The measurements were taken at temperatures between 425 – 550 °C at 25 °C intervals. For the non-equilibrium test, the pre-treatment involved reducing the sample with 5% H_2/Ar at 20 mL/min at 350 °C for 30 minutes followed by cooling the sample to room temperature and purging reactor with Ar for 30 minutes.

3.4 References

1. H.-X. Mai, L.-D. Sun, Y.-W. Zhang, R. Si, W. Feng, H.-P. Zhang, H.-C. Liu and C.-H. Yan, *The journal of physical chemistry. B*, 2005, 109, 24380-24385.

2. K. Zhou, X. Wang, X. Sun, Q. Peng and Y. Li, *Journal of Catalysis*, 2005, 229, 206-212.

3. S. A. Halawy, S. S. Al-Shihry and M. A. Mohamed, *Catalysis Letters*, 1997, 48, 247-251.

4 Ceria Morphologies Syntheses and Pd Deposition

Contents

4.1 Introduction

Tuning the morphology of ceria has been a challenging task, due to its isotropic nature[1-5]. Thus synthesis methods used for other anisotropic oxides to fabricate their morphologies cannot be applied to ceria. In the last decade, advances in synthesising different morphologies of ceria have been made where the synthesis of ceria nanoparticles with cube[1, 6-9], rod[1, 6-9], octahedron[2, 6, 8-11], wire[12-15], sheet[16, 17], plate[18, 19] and tube[20, 21] morphologies were reported. There were various methods used in the shape-controlled preparation of ceria which includes solvothermal treatment[1, 22, 23], microemulsion[24, 25], sol-gel[15], microwave[26, 27] and thermal decomposition[28]. The solvothermal technique, which includes hydrothermal method, has shown to be the most effective and economical method[29, 30], hence it was the most commonly used for fabricating ceria morphologies. Several modifications have also been made in an attempt to produce ceria morphologies with a narrow size distribution, well defined crystallographic surface facets and high shape selectivity by adding mineraliser, stabilising agent or surfactant[18, 19, 30-32].

This research involves the use of these ceria morphologies as a support for metal nanoparticles, where the effect of different surface facets of the ceria support could be studied. Therefore, the synthesis of ceria morphologies with well-defined crystallographic facets is vital. As the ceria morphologies were used as a metal nanoparticles support, the ceria morphologies had to be nano-sized to achieve a high surface area. It was also important for the ceria support to have a narrow size distribution for consistency of the study. As this research was concentrated to investigate the different effects of ceria (110) and (100) surfaces have on the supported metal nanoparticles, the morphologies which expose those surface facets were synthesised.

4.2 Ceria Morphologies

4.2.1 Method

The syntheses of ceria morphologies were based on the methods applied by Mai *et. al.*[1] and Zhou *et. al.*[23] who used hydrothermal method without the use of surfactants. The details of the synthesis method were covered in Chapter 3. In short, $Ce(NO_3)_3.6H_2O$ precursor was used as Ce^{3+} source and precipitated using NaOH in DI water. The precipitate mixture was subjected to hydrothermal treatment in a teflon-lined stainless steel digestion bomb. Hydrothermal temperatures of 100 °C and 180 °C for 24 hours would yield ceria nanoparticles with rod and cube morphologies respectively.

4.2.2 Results and Discussions

Figure 4.1 shows the XRD profiles of the synthesised ceria cubes and rods. They were also compared with the XRD profile of a commercial ceria sample. A comparison of the XRD profiles indicated that the synthesised ceria cubes and rods resulted in CeO_2 as their profiles were similar with that of the commercial CeO_2 sample. The profiles were indexed using Bragg's Law and all correspond to the fluorite structure of CeO_2 with a lattice parameter of 5.4153 Å[33, 34]. The XRD profile of the ceria rods showed some apparent peak broadening which gave an initial indication that the ceria rods sample was comprised small nanoparticles.

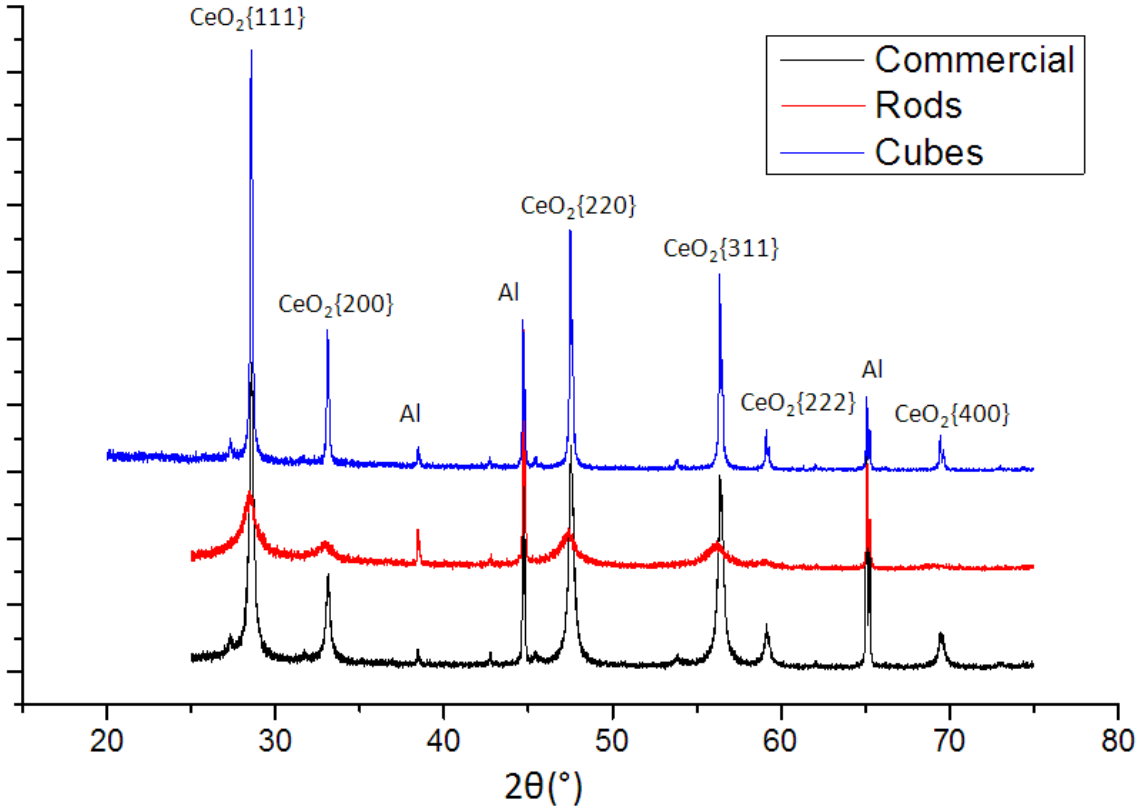

Figure 4.1 XRD profiles of synthesised ceria cubes and rods compared with commercial CeO_2.

XRD technique could also be used to distinguish the different morphologies as shown in previous study by comparing the relative intensities between the peaks. However the XRD profiles of the ceria morphologies showed no significant difference in their peak intensities. Thus in this case, XRD could not be used to differentiate the morphologies of ceria.

On the other hand, TEM images of the samples revealed the morphologies of the ceria cubes and rods (Figures 4.2 a and b) and they confirmed the synthesised ceria particles have the expected morphologies. The particles size distribution were based from measurements of 150 particles. Both methods of synthesis produced relatively uniform and narrow distributions of particle sizes for synthesis methods without surfactants (Figures 4.2 c and d). The ceria cubes resulted in a mean length of 17.1 nm whereas the rods had a mean length of 80.2 nm and mean

diameter of 8.00 nm. Hence, the apparent broadening of the peaks for the ceria rod observed in its XRD profile might be due to the small diameters of the rods as opposed to their lengths[35].

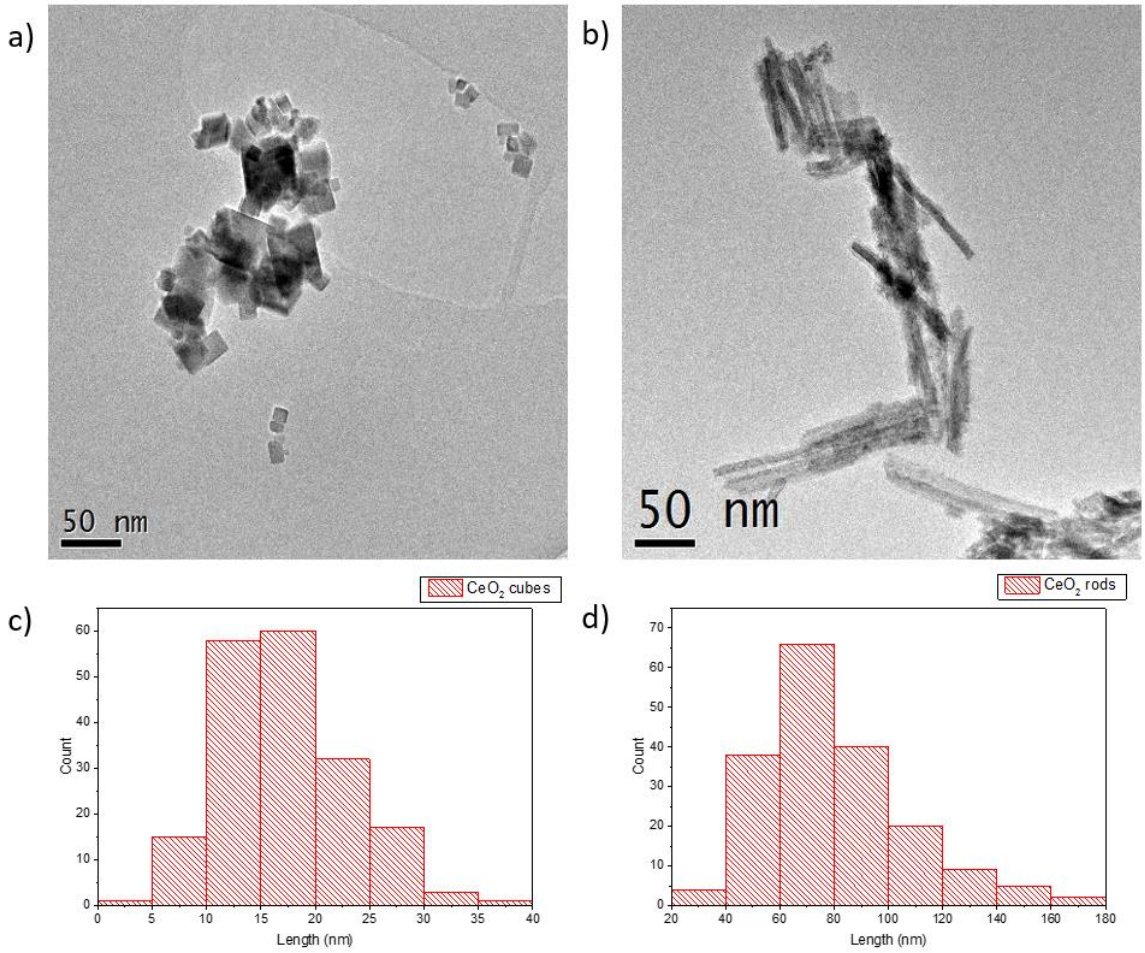

Figure 4.2 a) TEM image of ceria cubes b) TEM image of ceria rods. c) Particle size distribution of ceria cube d) Particle length distribution of ceria rods.

Based on these mean particle sizes, the cubes were calculated to have a surface area of 1754 nm^2 and 4433 nm^2 for the rods. Using the information from XRD where the lattice parameter of the unit cell of CeO_2 as 5.4153 Å, a particle of ceria cube has a mass of 3.6×10^{-17} g and a particle of rod has a mass of 2.9×10^{-17} g. Hence, these gave a theoretical surface area of 48 m^2/g for the cubes and 72 m^2/g for the rods. In addition, BET calculations of N_2 adsorption measurements of ceria morphologies, the cubes sample had a BET surface area of 28 m^2/g and the rods sample 89 m^2/g. In comparison between the two methods of surface area

measurements, both techniques showed that the ceria rods have higher surface area than the cubes. However, the BET calculation of the N_2 adsorption method would give a more accurate representation of the surface area as the measurement was taken based on 1 g of sample compared to the mean average over 150 particles of sample. The TEM measurements indicated an underestimation in the cubes mean particle size whilst an overestimation for the rods.

High resolution TEM was used to investigate the surface facets exposed by the morphologies. Figure 4.3a shows a high resolution TEM image of a ceria cube particle. The Fast Fourier Transform (FFT) of the image (Figure 4.3b) was compared with the FFT of a theoretical model of ceria and the surface exposed by the cube corresponded to the (100) surface (Figures 4.3 c and d). Hence, this gave an indication that the ceria cubes predominantly expose the (100) surface.

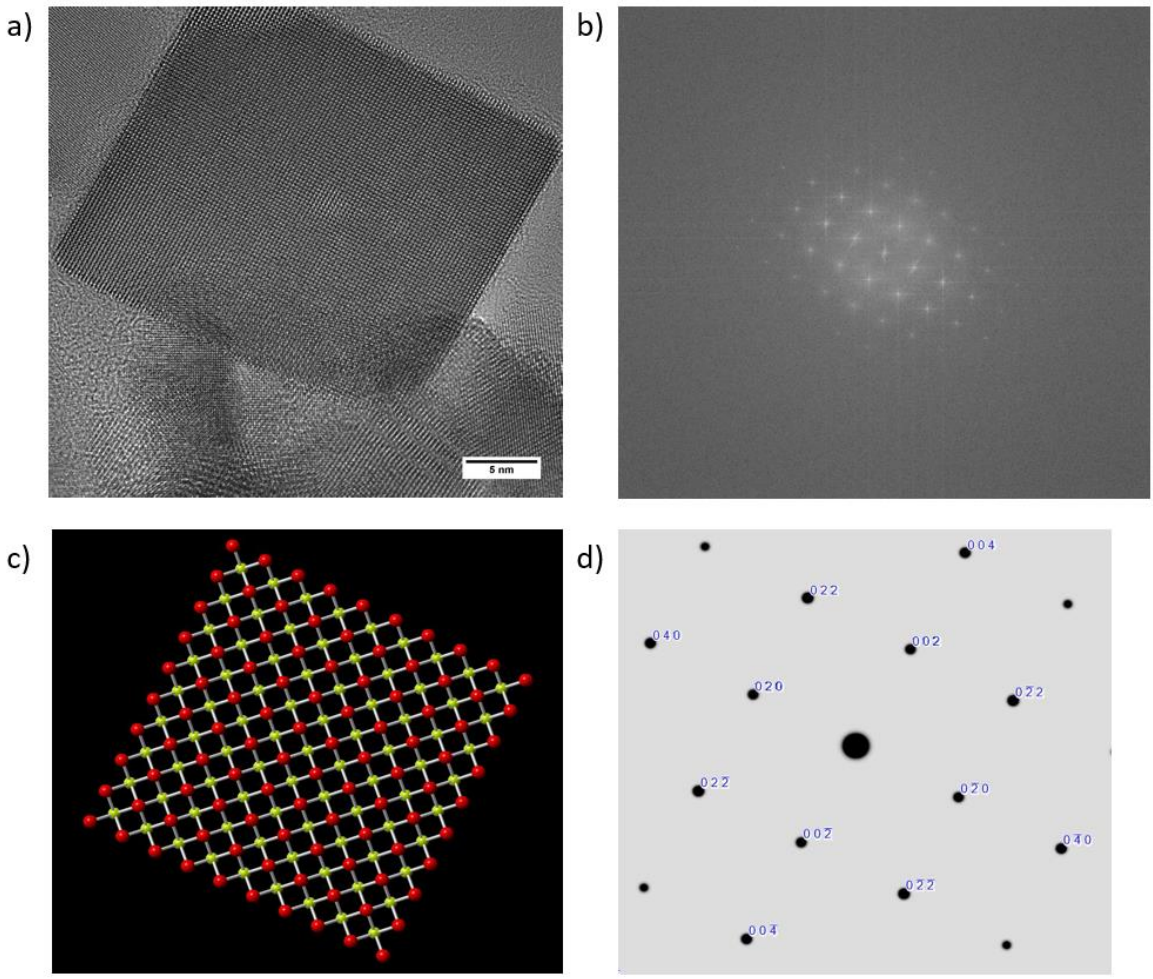

Figure 4.3 a) High resolution TEM image of ceria cube particle. b) FFT of the HR-TEM image. c) Theoretical model of ceria cube exposing the (100) surface. d) FFT of the ceria cube theoretical model.

Figure 4.4a shows the high resolution TEM image of a rod particle. It's FFT (Figure 4.4b) corresponded to the FFT of the ceria theoretical model set along the (110) direction indicating that the rods predominantly expose the (110) surface (Figures 4.4 c and d).

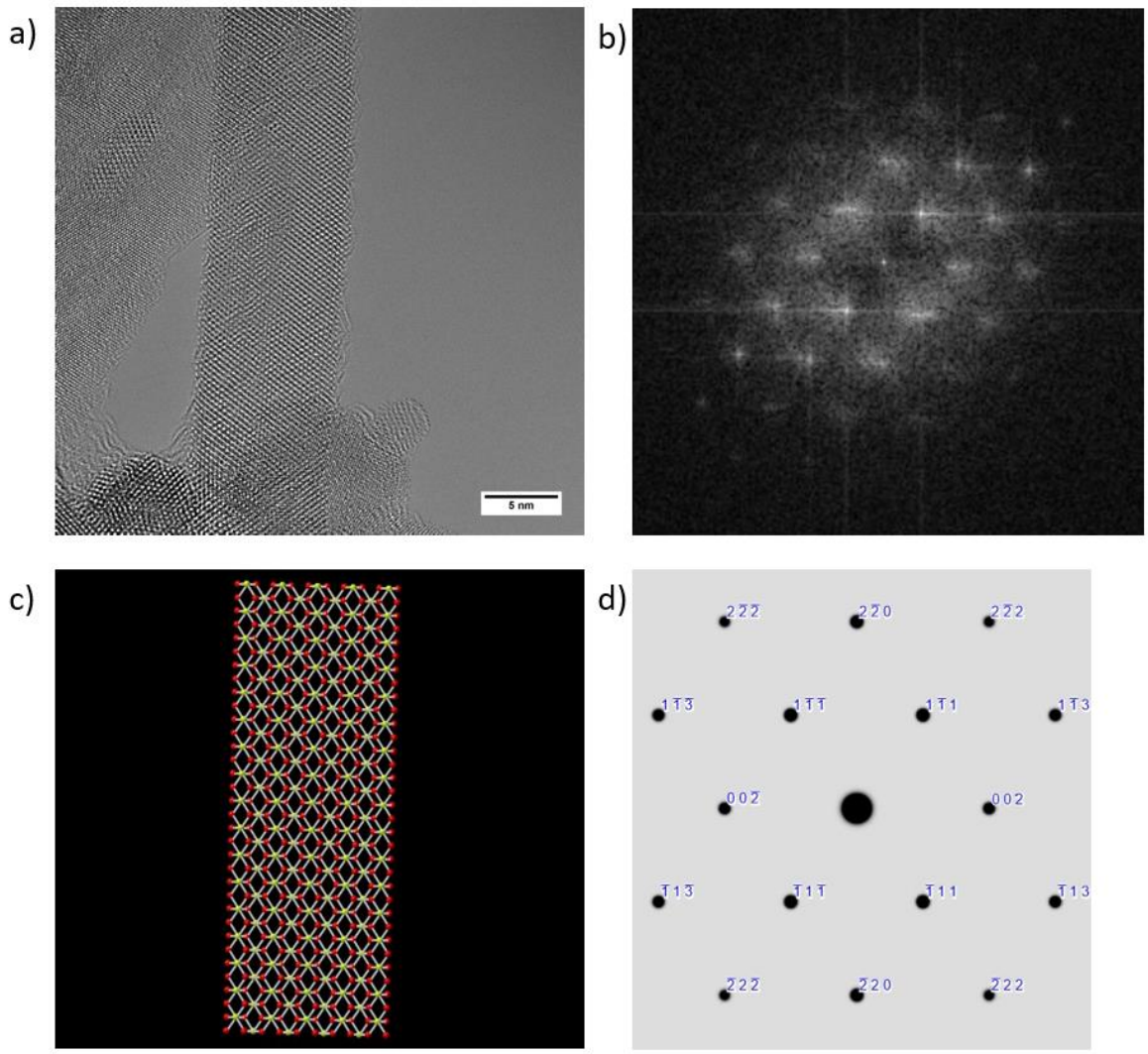

Figure 4.4 a) High resolution TEM image of ceria rod particle. b) FFT of the HR-TEM image. c) Theoretical model of ceria cube exposing the (110) surface. d) FFT of the ceria rod theoretical model.

In spite of the isotropic nature of CeO_2, ceria morphologies that expose surface facets with higher surface energy could be achieved with this hydrothermal method. According to Gibbs-Wulff theorem, the equilibrium morphology of a nanoparticle is the one that minimises the surface energy[32, 36]. Thus, according to this theorem, the exposed surface facets of these ceria morphologies should be the most stable surface which is the (111)[37-39]. However, this theorem is only taking thermodynamic factors into consideration. For particle growth, both kinetics and thermodynamics play important roles in the final shape of the particle[36]. Hence, this indicated

that the hydrothermal method was governed by kinetics, where both rods and cubes resulted in higher energy surfaces[35, 36, 40].

The hydrothermal synthesis of these morphologies followed two stages: the nucleation from the precursor by precipitation with the addition of the base and the crystal growth of the seeds into these nanoparticles during the hydrothermal treatment[35, 41]. The nucleation occurred when the $Ce(NO_3)_3.6H_2O$ was precipitated with NaOH in water (Equation 4.1) shown by the formation a light purple precipitate[42]. This precipitation is a sol-gel process where pH is an important factor[43]. Figure 4.5 shows a typical rate of hydrolysis and condensation reactions for a metal hydroxide/oxide. For nucleation to occur, the pH needs to be in the region where hydrolysis rate is minimised and condensation rate is maximised. In the case of $Ce(OH)_3$, the pH in which this occurs is 12[42]. According to previous studies, this high pH could also favour the oxidation the Ce^{3+} to Ce^{4+} [42, 44]. However, as pH 14 was used due to excess NaOH, the high concentration of $(OH)^-$ could supress this oxidation process[1, 23, 45]. This agreed with the observation that upon stirring, the precipitate did not turn to yellow, which suggested that Ce^{4+} was not formed.

$$Ce^{3+}_{(aq)} + 3OH^-_{(aq)} \rightarrow Ce(OH)_{3(s)} \qquad \text{Equation 4.1}$$

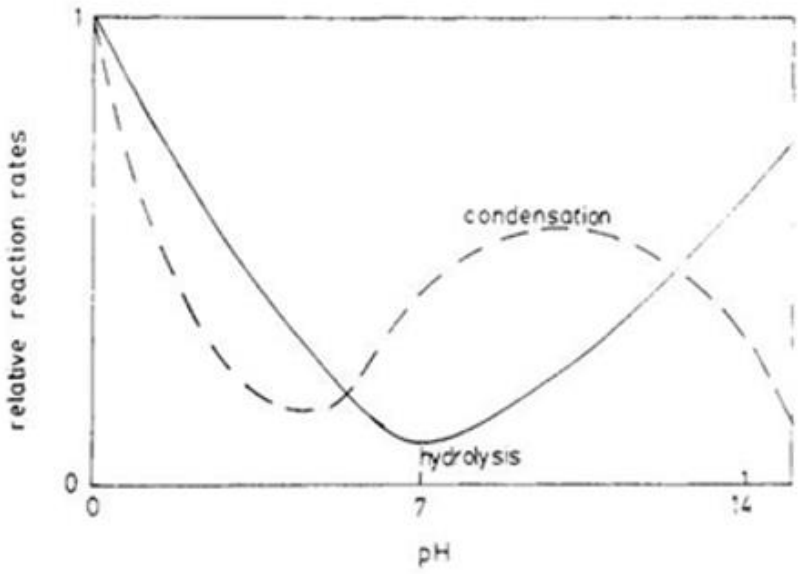

Figure 4.5 A schematic of the pH dependence on the rates of hydrolysis and condensation reactions in precipitation process[43].

There has been numerous work published investigating the growth mechanism of the ceria morphologies from their nuclei during the hydrothermal treatment[35, 36, 42, 46]. There are generally two types of mechanism for particle growth: Ostwald ripening or oriented attachment. Ostwald ripening (dissolution/recrystallisation) occurs through the dissolution of small particles followed by precipitation onto other particles, forming larger particles. Oriented attachment, on the other hand, involved the attachment of two or more particles which shared a crystallographic orientation which was induced by collision and coalescence[46].

Ostwald ripening has been the most accepted mechanism for the growth of the nuclei into these morphologies. Mai et. al. suggested that the anisotropic Ce^{3+} must have been maintained during the growth stage for anisotropic crystal growth as opposed to the isotropic Ce^{4+} [1]. With high OH^- concentration, the rate of Oswald ripening was enhanced for the $Ce(OH)_3$ nuclei to grow anisotropically, hence producing the rod morphology at 100 °C. On the other hand, when the temperature was increased to 180 °C, the high temperature favoured the oxidation and

dehydration of $Ce(OH)_3$ into CeO_2, hence both Oswald ripening and oxidation reaction resulted in the formation of the cube morphology (Figure 4.6).

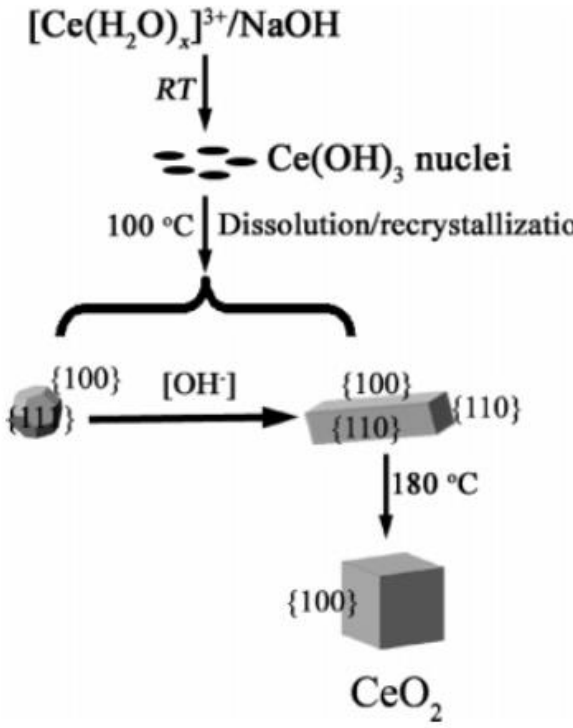

Figure 4.6 Proposed mechanism of the syntheses of ceria cube and rods[1].

However, Taniguchi *et. al.* and Lin *et. al.* argued that oriented attachment also play a major role in the growth of ceria particles[35, 46]. They suggested that the Ce^{3+} precursor favoured the oriented attachment mechanism and at higher pH, the solubility of Ce^{3+} is very low, thus minimising the Oswald ripening mechanism. Even with high aggregation of particles at pH 14, where collision is disfavoured, oriented attachment could still take place producing rod-like structure[35], which could be an alternative explanation to the formation of the ceria rods. Nevertheless, there is no clear cut evidence on which one of these two mechanisms is the dominant process as this requires more investigation into the properties of the nanocrystal structure such as their pore structures, twin boundaries, defects and dislocations.

4.2.3 Ceria morphologies thermal stability

As these ceria morphologies were used as a support for metal nanoparticles aimed for catalysis studies, they needed to be stable upon heat treatment at high temperature. In particular their shape must be stable to high temperature so that their exposed surfaces could be maintained. As the (111) surface is the most thermodynamically stable surface of ceria, high temperatures would be expected to change the less stable (100) and (110) surface to the more stable (111) surface. There would also be the issue of aggregation at high temperatures. Hence, these ceria morphologies were tested upon thermal treatment to ensure their surface stability and shape sustainability.

The ceria cubes and rods samples were thermally tested with TGA and in-situ XRD. TGA up to 1000 °C showed no weight loss for both samples indicating the ceria structure was stable from decomposition. In-situ XRD also showed no significant changes in their profiles upon heating to 800 °C suggesting the cubic fluorite structure was maintained upon heat treatment. The only apparent changes to the XRD profiles of both ceria cubes and rods were their peaks appeared to be narrower as the temperature was increased which implied the formation of larger particles as suggested by the Scherrer equation. These results agreed with previous studies where they observed that the ceria fluorite structure was stable up to its melting point[4, 5, 47].

Even though TGA and in-situ XRD showed the stability of the CeO_2 cubic fluorite structure up to 1000 °C, they did not provide any information about the size, shape and surface changes of the ceria nanoparticles. Hence, the ceria morphologies were heated up from 200 °C to 500 °C in 100 °C intervals under air atmosphere and their TEM images were taken. Their mean sizes and particle size distributions were calculated based on measurements of 150 particles.

Figure 4.7 shows the size distributions of the ceria cubes after the thermal treatment in air with their corresponding mean sizes (Table 4.1). From the TEM images, the cube morphology and its (100) surface were maintained at temperatures up to 500 °C. Generally, there was an increase in mean size with temperature. Also by comparison of their particle size distributions, higher temperatures led to the broadening of the distribution suggesting less size homogeneity.

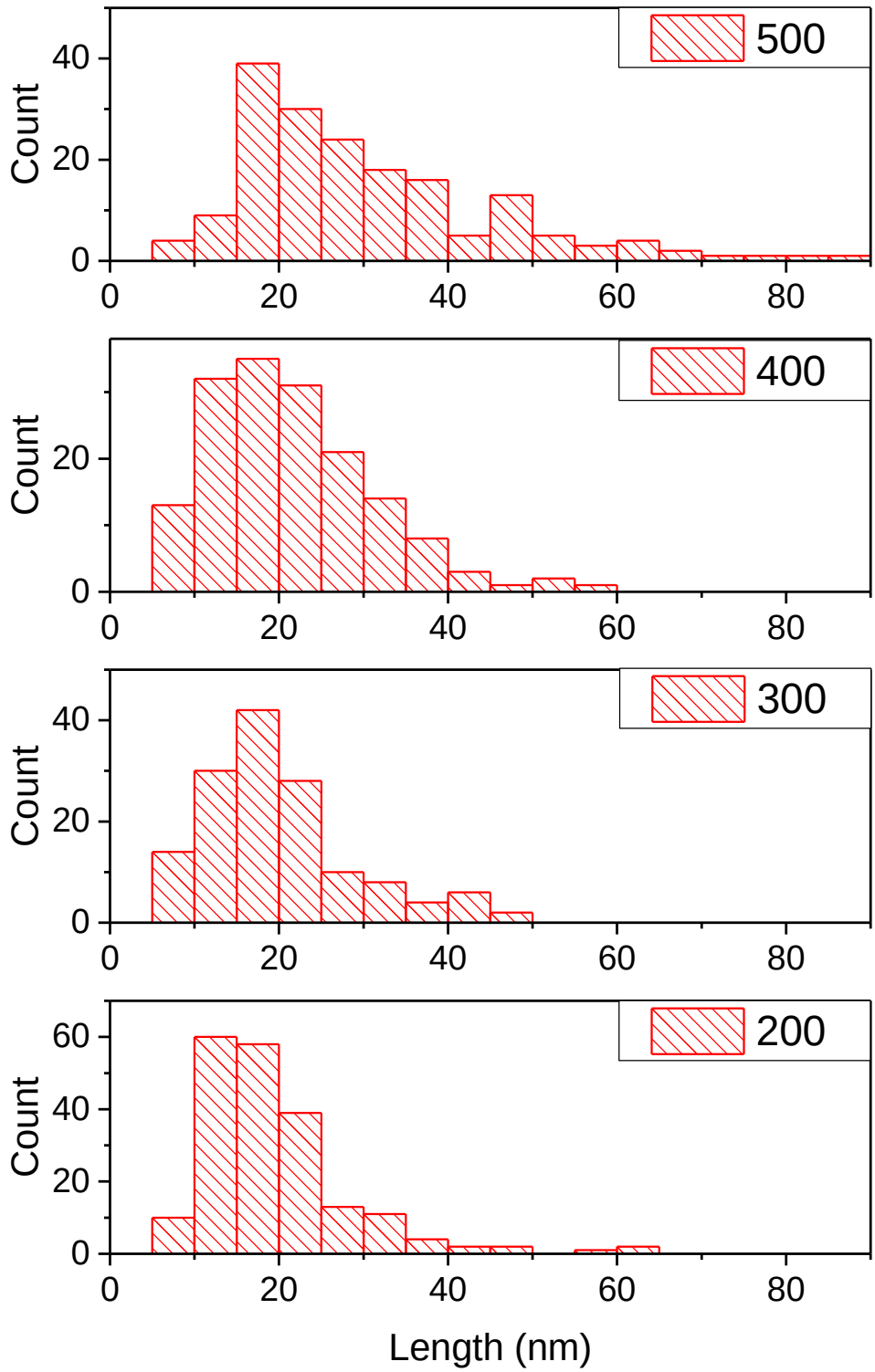

Figure 4.7 The particle size distributions of ceria cubes upon thermal treatment from 200-500 °C at 100 °C intervals, in air for 1 hour.

Temperature/°C	Mean Length/nm	Standard Deviation/nm
RT	17.1	6.1
200	19.6	8.9
300	19.8	8.9
400	21.6	9.8
500	30.3	15.2

Table 4.1 The mean lengths of the ceria cubes upon thermal treatment from 200-500 °C at 100 °C intervals, in air for 1 hour.

The similar trend can also be seen with the ceria rods, where increase in temperature caused the increase in their mean length and less size uniformity suggested by the broadening of the size distributions (Figure 4.8 and Table 4.2). However, as the cubes sample, the ceria rod shape is preserved and (110) was maintained as the predominant surface. Upon the heat treatment to 500 °C, the mean diameter of the rods were kept around 8 nm suggesting lengthwise growth of the ceria rod particles. This observation agreed with previous studies where ceria nanoparticles had minimal particle growth when calcined below 600 °C[5].

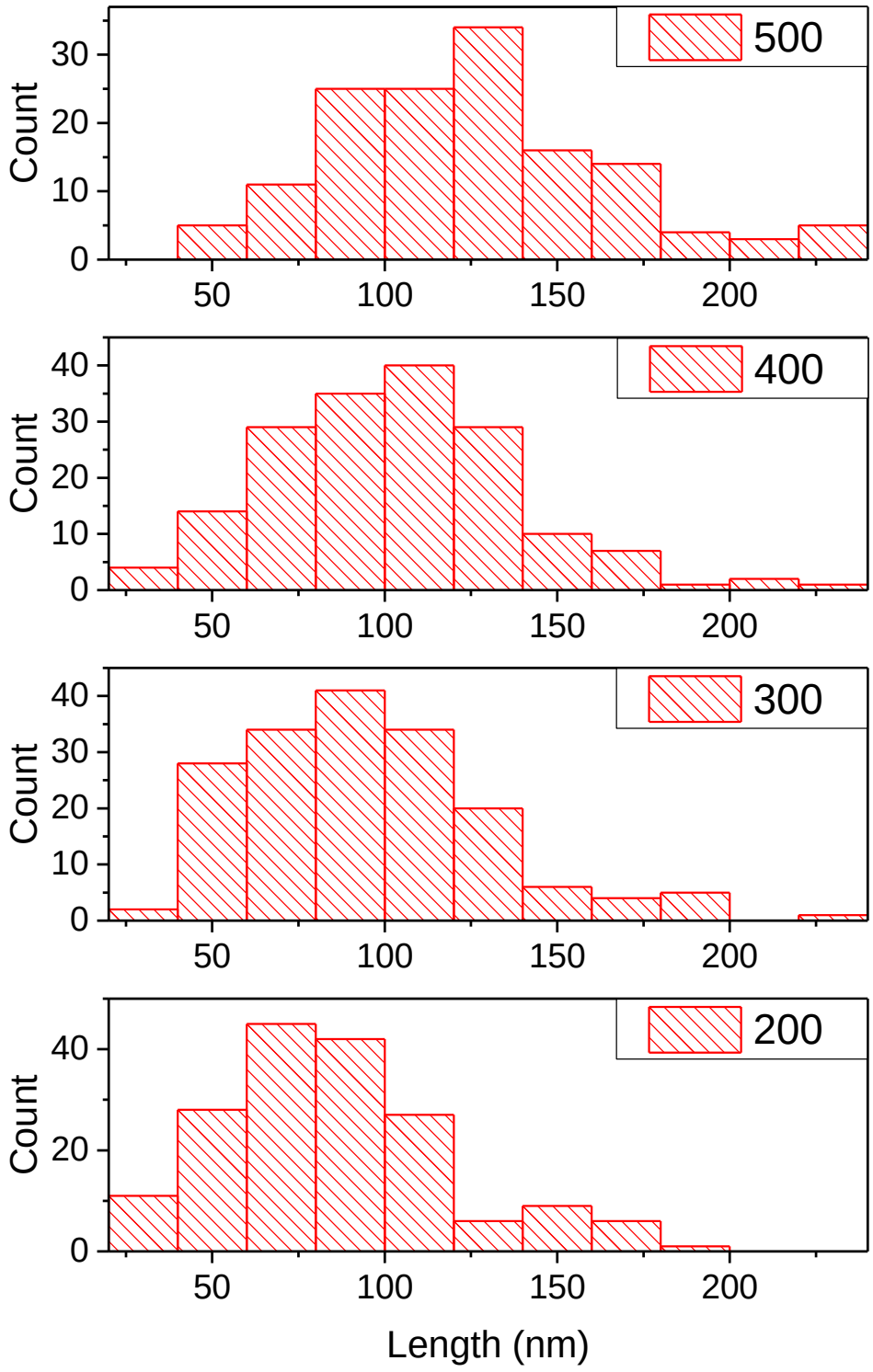

Figure 4.8 The particle size distributions of ceria rods upon thermal treatment from 200-500 °C at 100 °C intervals, in air for 1 hour.

Temperature/°C	Mean Length/nm	Standard Deviation/nm
RT	80.2	26.5
200	85.3	33.8
300	95.1	35.0
400	102.5	35.0
500	126.8	42.3

Table 4.2 The mean lengths of the ceria rods upon thermal treatment from 200-500 °C at 100 °C intervals, in air for 1 hour.

4.2.4 Conclusion

Ceria cubes and rods have been successfully synthesised using a facile template-free hydrothermal method to yield nanoparticles with well-defined (100) facets for the cubes and (110) for the rods. The hydrothermal methods also indicated to be size-controlled where narrow size distributions were achieved for both morphologies. Both ceria cube and rods were thermally tested and both of them showed stability up to 500 °C, the maximum testing temperature. Upon heating, both of the morphologies maintained their shape and had minimal particle growth.

4.3 Pd Deposition

4.3.1 Introduction

As Pd was to be deposited onto these ceria supports, various methods of deposition techniques need to be considered to ensure that small Pd nanoparticles could be formed with high stability and dispersion across the support. The method applied also needs to be able to maximise the well-known metal-support interaction between Pd and ceria[48-53]. There are a number of available methods reported to deposit small Pd nanoparticles into the ceria support, which mostly involve the bottom up approach.

The impregnation technique consisted of mixing the support with a solution containing the metal precursor. It can be done where the solution used does not exceed the pore volume of the support which is referred to as incipient wetness impregnation, or where the solution exceeds the pore volume, called wet impregnation. The support and metal precursor mixture is then aged for a specific time, dried and calcined. However this method involves a high calcination temperature for the precursor anion, for example nitrate to be decomposed[54].

Deposition-precipitation method consists of the precipitation of the metal precursor, typically using a base, which allows the nucleation of the metal oxide/hydroxide on the support. In this case, this process is pH dependent as to ensure the precipitation rate is higher than hydrolysis rate for the nuclei to be formed. The metal oxide/hydroxide would then be reduced to the metal form, usually by calcining in H_2 gas or by adding a reductant. Because of the pH dependence of the precipitation process, this method is usually only suitable for non-acidic oxides as high pH is typically needed for precipitation to occur[52].

Metal vapour deposition, where the precursor, usually organometallic is vaporised in a heated vacuum system and then deposited onto the support. After that, the deposited support is calcined in air to remove the organic ligands of the precursor. Even though this method has shown to be very efficient, it often use very expensive organometallic precursors[55, 56].

Solid grinding is one of the easiest deposition method. The solid precursor is simply grinded together with the support. The grinding can be done by mortar and pestle or by ball milling. Similar to the impregnation technique, the sample needs to be calcined at a high temperature to decompose the precursor anion. Another disadvantage of this method is particle size cannot be controlled properly[57].

With all these available methods of metal decomposition onto the support, the method that would be most favourable for this project is the one that could prepare stable well dispersed small Pd nanoparticles and where metal-support interaction is maximised. The method is also required to be performed at low temperatures to avoid aggregation or particle growth of the ceria support. For consistency, it is important for the method to produce a narrow particle size distribution for Pd nanoparticles.

4.3.2 Method

In order to fulfil the requirements needed for metal deposition, the deposition-precipitation technique was used. The full synthesis method is covered in Chapter 3. $Pd(NO_3)_2$ was used as Pd precursor which is mixed with the ceria cubes and rods supports to prepare 1% Pd loading. After the mixture was well mixed, the precipitation was performed by adding 0.1M NaOH to form a $Pd(OH)_2$ precipitate. The mixture was then bubbled with H_2 gas to reduce the $Pd(OH)_2$ to Pd^0 at room temperature. The mixture turned black implying the reduction of Pd^{2+} to Pd^0, as

Pd was known to reduce even at room temperature. The Pd deposited ceria morphologies were then, filtered, washed and dried.

4.3.3 Results

By comparing the XRD profile of 1% Pd/ceria cubes against profile of undeposited ceria cubes (Figure 4.9), there was no significant difference. This might be due to the Pd nanoparticles being highly dispersed or very small sized which causes peak broadening[58]. This shows XRD was not a suitable technique to characterise the deposited Pd on the ceria morphologies support. However, the XRD profile also suggested that there was no structural changes in the ceria support.

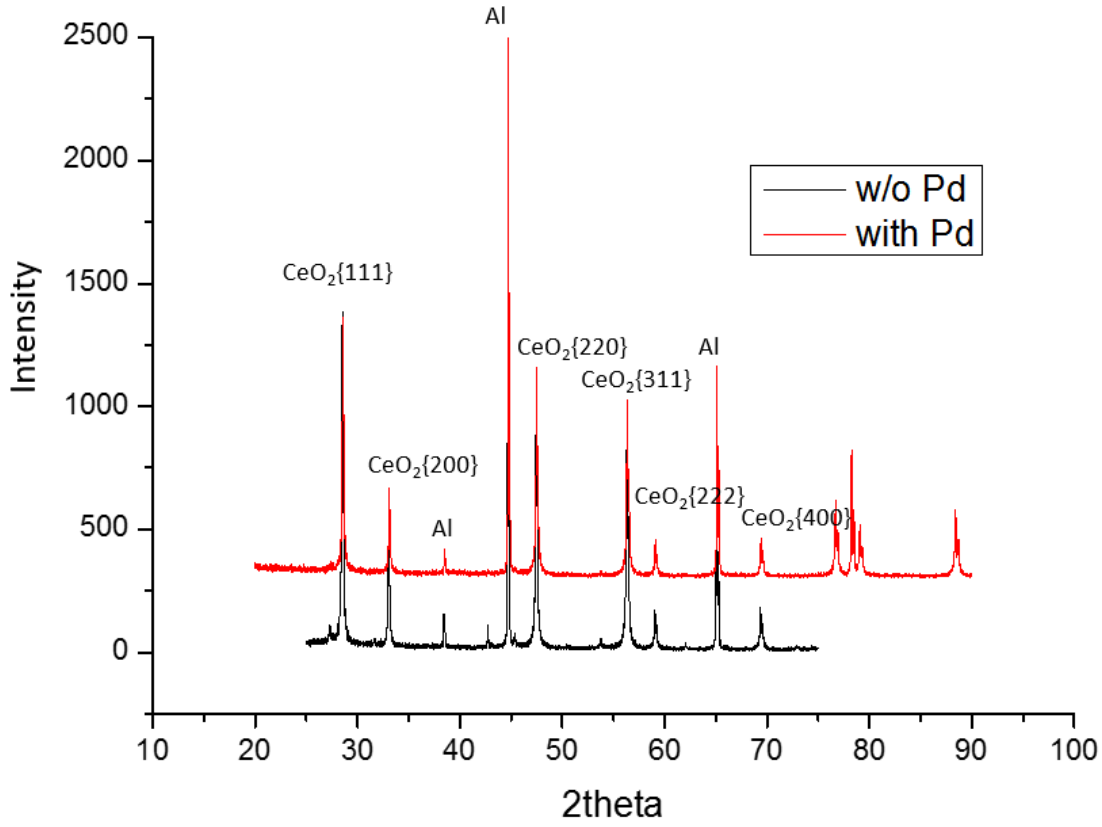

Figure 4.9 XRD profile of Pd deposited ceria cubes compared with that of non-deposited ceria cubes.

Hence, TEM was used to investigate the deposited Pd on the ceria supports. Figure 4.10a shows the TEM image of 1% Pd/ceria cubes, where the Pd nanoparticles could be identified by the darker spherical particles. EDX also agreed with the presence of Pd species in the sample indicating that the deposition-precipitation method successfully deposited small Pd nanoparticles onto the ceria cube support (Figure 4.10c). The particle size distribution of Pd was taken based on the measurements of 150 nanoparticles and it showed that the Pd nanoparticles deposited onto the ceria had a narrow distribution with a mean size of 2.1 ± 0.3 nm (Figure 4.10b). This mean particle size corresponds to the theoretical surface area of 238 m^2/g(Pd) and 2.38 m^2/g(catalyst).

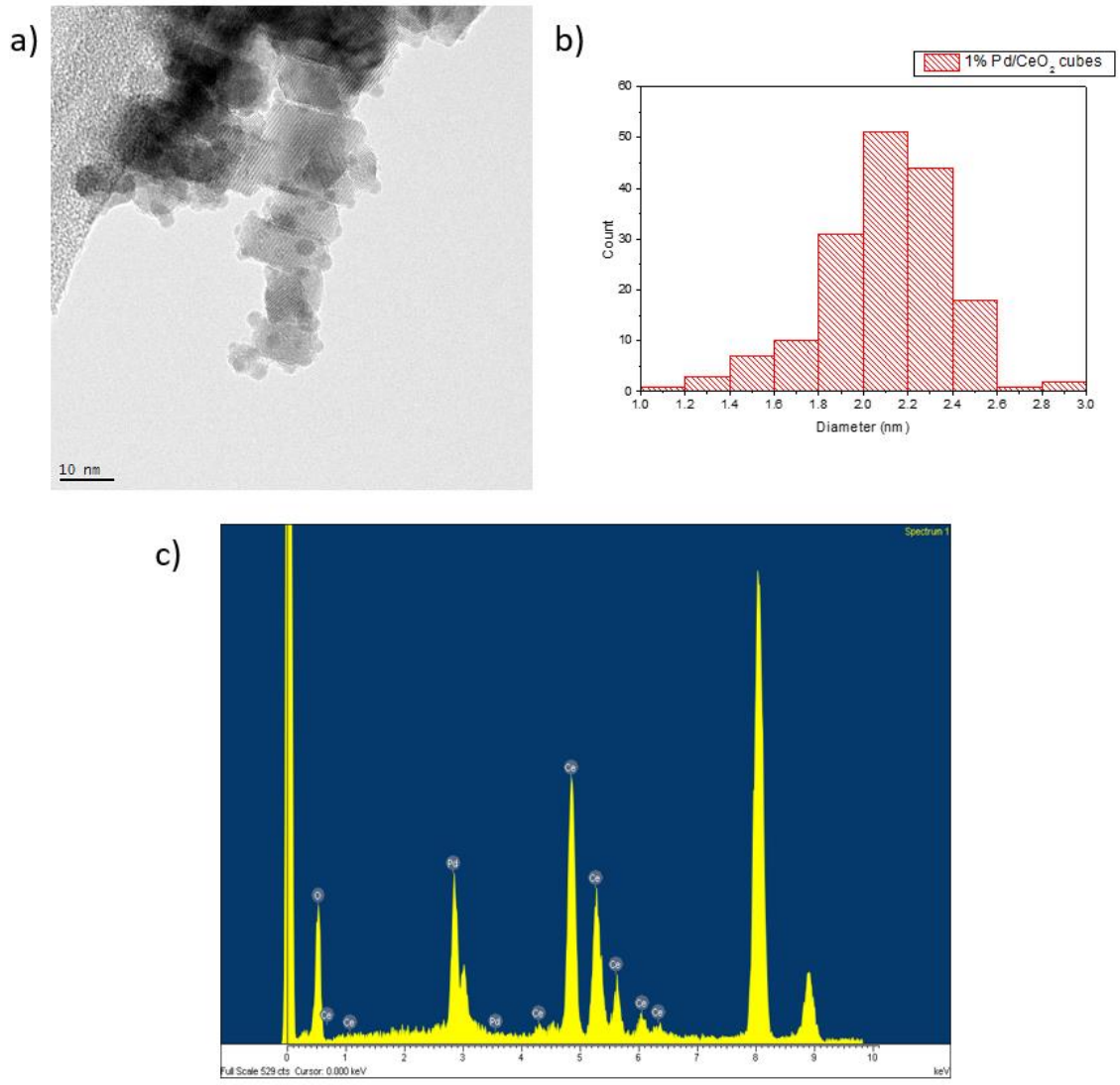

Figure 4.10 a) TEM image of 1% Pd deposited on ceria cubes and **b)** their particle size distribution. **c)** EDX of 1% Pd/Ceria cubes sample.

The Pd was also successfully deposited using the same deposition-precipitation method onto the ceria rods as shown in the TEM image and its corresponding EDX (Figures 4.11 a and c). Like previously, the deposited Pd also had uniform sizes as suggested by the Pd particle size distribution and had a similar mean size of 1.8 ± 0.3 nm (Figure 4.11b). Assuming that all the Pd particles were spherical, this would give a theoretical surface area of 274 m^2/g(Pd) and 2.74 m^2/g(catalyst).

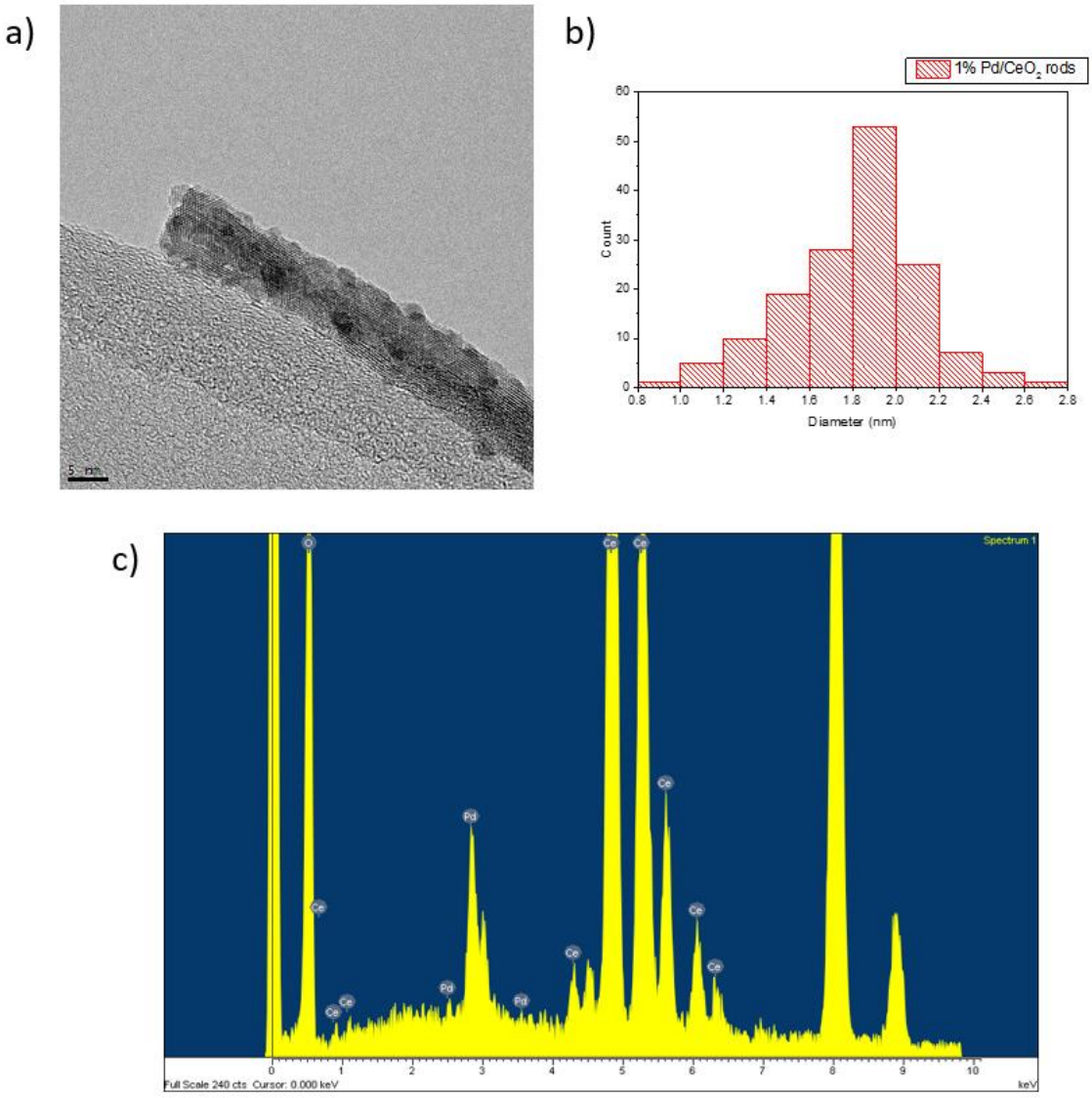

Figure 4.11 a) TEM image of 1% Pd deposited on ceria rods and **b)** their particle size distribution. **c)** EDX of 1% Pd/Ceria cubes sample.

As there is no significant difference in the Pd particle size on both the ceria cubes and rods, it could be assumed that the Pd particle size and surface area effects could be disregarded in the catalyst test reactions.

4.3.4 Pd/ceria thermal stability

As the ceria cubes and rods support has been shown to withstand heat treatment up to 500 °C, the Pd nanoparticles deposited on them needed to have the similar thermal stability as well. Because of their small sizes, they were expected to aggregate into bigger particles more easily compared to their ceria support. Hence, their thermal stability was tested by heating in air for 1 hour at temperatures up to 500 °C in 100 °C intervals and their TEM images were taken. The sizes of 150 Pd nanoparticles were then measured and their particle size distributions and mean sizes were calculated (Figures 4.12, 4.13 and Table 4.3).

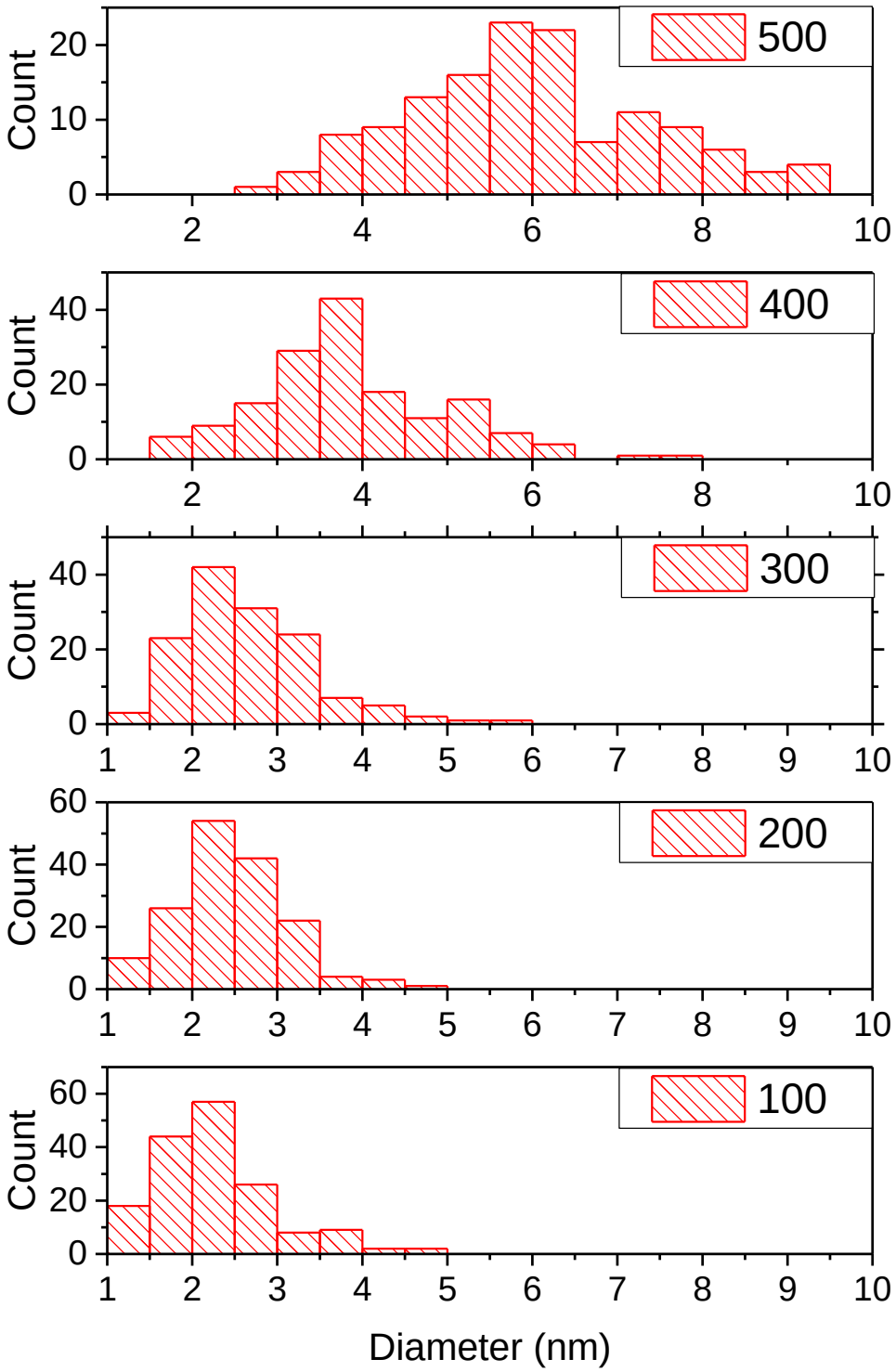

Figure 4.12 The particle size distributions of 1% Pd nanoparticles deposited on ceria cubes subjected under thermal treatment in air for 1 hour at 100-500 °C at 100 °C intervals.

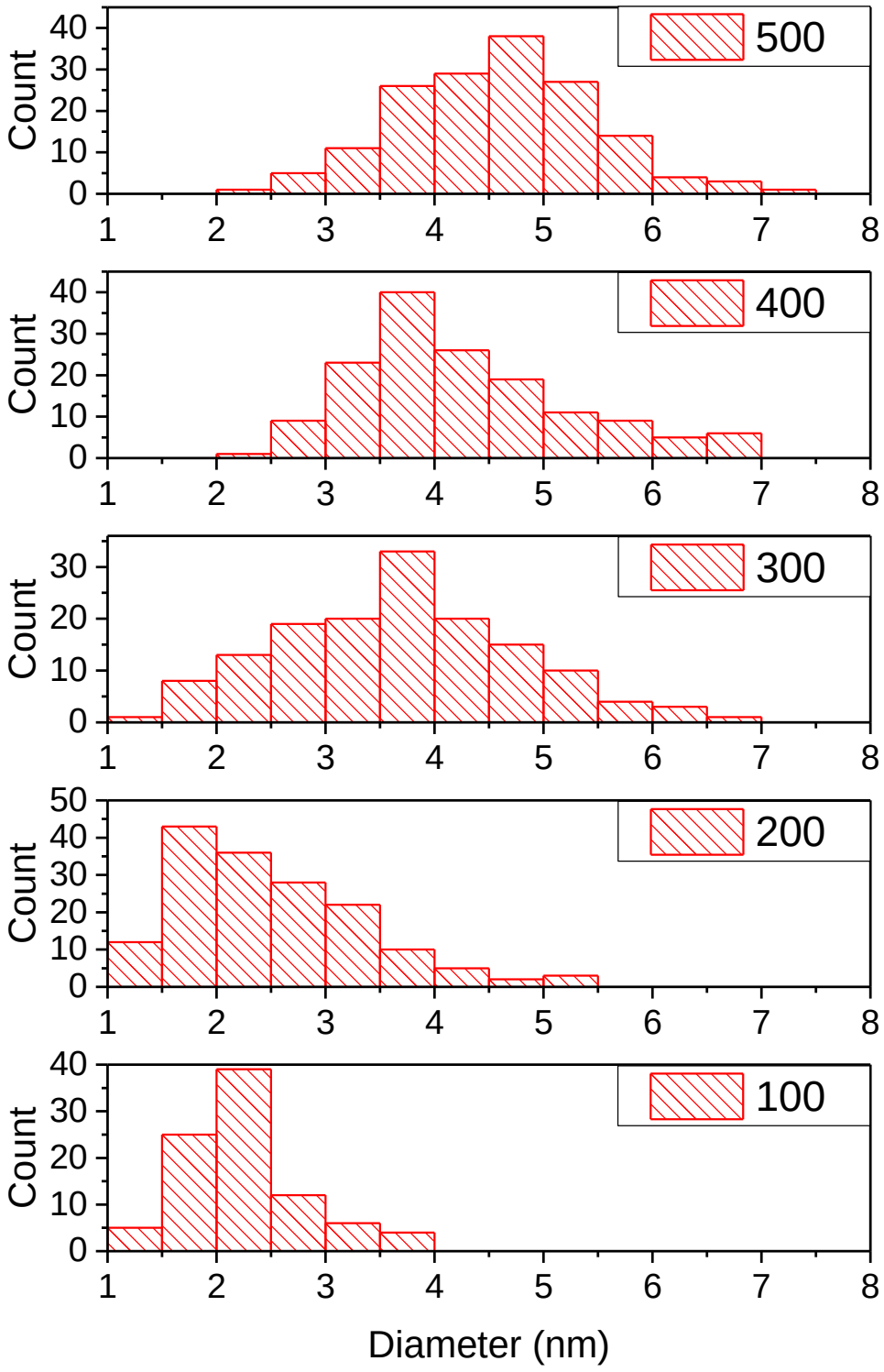

Figure 4.13 The particle size distributions of 1% Pd nanoparticles deposited on ceria rods subjected under thermal treatment in air for 1 hour at 100-500 °C at 100 °C intervals.

Temperature	1% Pd/ceria cubes			1% Pd/ceria rods		
	TEM (nm)	Standard deviation (nm)	CO chemisorption (nm)	TEM (nm)	Standard Deviation (nm)	CO pulse chemisorption (nm)
100	2.3	0.7	2.4	2.9	1.1	2.1
200	2.5	0.6	1.7	2.5	0.9	2.1
300	2.7	0.8	2.7	3.7	1.1	2.9
400	3.9	1.1	5.9	4.3	1.0	4.0
500	6.1	1.6	5.6	4.6	0.9	6.2

Table 4.3 The Pd mean particles sizes based on 150 particles measured by TEM and Pd particles sizes measured by CO chemisorption at different temperatures.

In general, the increase in temperature of calcination increased the size of the Pd nanoparticles deposited on both ceria cube and rod supports. Nevertheless, both maintained mean sizes below 10 nm upon heat treatment up to 500 °C. The broadening of their size distributions indicated that the Pd nanoparticles became less uniform as the temperature was increased.

The mean sizes obtained by the size distributions were also compared with the mean sizes measured by the CO pulse chemisorption method (Table 4.3). The heat treatment was introduced during the pretreatment, where the samples were heated under H_2 for one hour and then cooled before the CO chemisorption measurements were made. It was assumed that all the chemisorbed CO used for the measurement of Pd nanoparticles mean sizes were chemisorbed onto the Pd. The ceria support was also assumed to be inert in the CO pulse measurement. Both methods of Pd mean size measurement indicated the increase in size as the temperature was increased and their values were in agreement with each other. However, their particles sizes did not exceed 10 nm and the increase in sizes were minimal at temperatures

below 400 °C. The agreement in the values of Pd mean sizes suggested that the ceria had insignificant role in the chemisorption of CO.

4.3.5 Conclusion

1% Pd nanoparticles were deposited onto the ceria cubes and rods using deposition-precipitation technique. The deposition method used were able to successfully deposit small Pd^0 nanoparticles with a mean size of about 2 nm and a narrow particle size distribution for both supports. Furthermore, the Pd nanoparticles were well-dispersed throughout both ceria cubes and rods supports. They were also thermally stable up to 400 °C where particle growth was minimal. Hence the 1% Pd/ceria cubes and rods would be sufficiently stable as catalysts when subjected to high temperatures.

4.4 References

1. H.-X. Mai, L.-D. Sun, Y.-W. Zhang, R. Si, W. Feng, H.-P. Zhang, H.-C. Liu and C.-H. Yan, *The journal of physical chemistry. B*, 2005, **109**, 24380-24385.
2. Z. Wang and X. Feng, *The Journal of Physical Chemistry B*, 2003, **107**, 13563-13566.
3. Y. C. Zhou and M. N. Rahaman, *Journal of Materials Research*, 1993, **8**, 1680-1686.
4. M. Hirano and E. Kato, *Journal*, 1996, **79**, 777-780.
5. M. Hirano and E. Kato, *Society*, 1999, **88**, 786-788.
6. T. Désaunay, G. Bonura, V. Chiodo, S. Freni, J. P. Couzinié, J. Bourgon, a. Ringuedé, F. Labat, C. Adamo and M. Cassir, *Journal of Catalysis*, 2013, **297**, 193-201.
7. S. Agarwal, L. Lefferts, B. L. Mojet, D. a. J. M. Ligthart, E. J. M. Hensen, D. R. G. Mitchell, W. J. Erasmus, B. G. Anderson, E. J. Olivier, J. H. Neethling and A. K. Datye, *ChemSusChem*, 2013, **6**, 1898-1906.
8. S. Wang, L. Zhao, W. Wang, Y. Zhao, G. Zhang, X. Ma and J. Gong, *Nanoscale*, 2013, **5**, 5582-5588.
9. J. Han, H. J. Kim, S. Yoon and H. Lee, *Journal of Molecular Catalysis A: Chemical*, 2011, **335**, 82-88.
10. S. Agarwal, L. Lefferts and B. L. Mojet, *ChemCatChem*, 2013, **5**, 479-489.
11. E. Aneggi, D. Wiater, C. de Leitenburg, J. Llorca and A. Trovarelli, *ACS Catal.*, 2014, **4**, 172-181.
12. B. Tang, L. Zhuo, J. Ge, G. Wang, Z. Shi and J. Niu, *Chemical communications (Cambridge, England)*, 2005, DOI: 10.1039/b500708a, 3565-3567.
13. M. Yada, S. Sakai, T. Torikai, T. Watari, S. Furuta and H. Katsuki, *Adv. Mater.*, 2004, **16**, 1222-1226.
14. R. J. La, Z. A. Hu, H. L. Li, X. L. Shang and Y. Y. Yang, *Materials Science and Engineering A*, 2004, **368**, 145-148.

15. G. S. Wu, T. Xie, X. Y. Yuan, B. C. Cheng and L. D. Zhang, *Materials Research Bulletin*, 2004, **39**, 1023-1028.

16. B. Liu, B. Liu, Q. Li, X. Du, M. Yao, Z. Li, R. Liu, D. Liu, X. Zou, H. Lv, D. Li, B. Zou, T. Cui and G. Zou, *J. Alloy. Compd.*, 2011, **509**, 6720-6724.

17. X. Han, L. Li and C. Wang, *Crystengcomm*, 2012, **14**, 1939-1939.

18. D. Wang, Y. Kang, V. Doan-Nguyen, J. Chen, R. Küngas, N. L. Wieder, K. Bakhmutsky, R. J. Gorte and C. B. Murray, *Angewandte Chemie (International ed. in English)*, 2011, **50**, 4378-4381.

19. C. Pan, D. Zhang and L. Shi, *Journal of Solid State Chemistry*, 2008, **181**, 1298-1306.

20. J. J. Miao, H. Wang, Y. R. Li, J. M. Zhu and J. J. Zhu, *Journal of Crystal Growth*, 2005, **281**, 525-529.

21. W.-Q. Han, L. Wu and Y. Zhu, *Journal of the American Chemical Society*, 2005, **127**, 12814-12815.

22. R. I. Walton, *Prog. Cryst. Growth Charact. Mater.*, 2011, **57**, 93-108.

23. K. Zhou, X. Wang, X. Sun, Q. Peng and Y. Li, *Journal of Catalysis*, 2005, **229**, 206-212.

24. Y. Huang, Y. Cai, D. Qiao and H. Liu, *Particuology*, 2011, **9**, 170-173.

25. S. Y. Yao, W. Q. Xu, a. C. Johnston-Peck, F. Z. Zhao, Z. Y. Liu, S. Luo, S. D. Senanayake, A. Martínez-Arias, W. J. Liu and J. a. Rodriguez, *Physical Chemistry Chemical Physics*, 2014, **16**, 17183-17183.

26. S. Hilaire, L. Luo, F. Rechberger, F. Krumeich and M. Niederberger, *Zeitschrift Fur Anorganische Und Allgemeine Chemie*, 2014, **640**, 733-737.

27. Y. Tao, F. H. Gong, H. Wang, H. P. Wu and G. L. Tao, *Materials Chemistry and Physics*, 2008, **112**, 973-976.

28. B. Bakiz, F. Guinneton, J. P. Dallas, S. Villain and J. R. Gavarri, *Journal of Crystal Growth*, 2008, **310**, 3055-3061.

29. W. Shan, H. Guo, C. Liu and X. Wang, *Journal of Rare Earths*, 2012, **30**, 665-669.

30. L. Yan, R. Yu, J. Chen and X. Xing, *Cryst. Growth Des.*, 2008, **8**, 1474-1477.

31. T. S. Sreeremya, A. Krishnan, K. C. Remani, K. R. Patil, D. F. Brougham and S. Ghosh, *ACS Applied Materials & Interfaces*, 2015, **7**, 8545-8555.

32. Z. Yang, K. Zhou, X. Liu, Q. Tian, D. Lu and S. Yang, *Nanotechnology*, 2007, **18**, 185606-185606.

33. A. Trovarelli, *Comments on Inorganic Chemistry*, 1999, **20**, 263-284.

34. D. R. Mullins, *Surface Science Reports*, 2015, **70**, 42-85.

35. M. Lin, Z. Y. Fu, H. R. Tan, J. P. Y. Tan, S. C. Ng and E. Teo, *Crystal Growth and Design*, 2012, **12**, 3296-3303.

36. K. Zhou and Y. Li, *Angewandte Chemie - International Edition*, 2012, **51**, 602-613.

37. T. X. T. Sayle, S. C. Parker and C. R. a. Catlow, *Surface Science*, 1994, **316**, 329-336.

38. J. C. Conesa, *Surface Science*, 1995, **339**, 337-352.

39. M. Nolan, S. Grigoleit, D. C. Sayle, S. C. Parker and G. W. Watson, *Surface Science*, 2005, **576**, 217-229.

40. Y. Xiong and Y. Xia, *Adv. Mater.*, 2007, **19**, 3385-3391.

41. T. K. Sau and A. L. Rogach, *Adv. Mater.*, 2010, **22**, 1781-1804.

42. V. Morris, P. G. Fleming, J. D. Holmes and M. a. Morris, *Chemical Engineering Science*, 2013, **91**, 102-110.

43. H. D. Gesser and P. C. Goswami, *Chemical Reviews*, 1989, **89**, 765-788.

44. L. Chen, P. Fleming, V. Morris, J. D. Holmes and M. A. Morris, *J. Phys. Chem. C*, 2010, **114**, 12909-12919.

45. Q. Wu, F. Zhang, P. Xiao, H. S. Tao, X. Z. Wang, Z. Hu and Y. N. Lu, *J. Phys. Chem. C*, 2008, **112**, 17076-17080.

46. T. Taniguchi, K. I. Katsumata, S. Omata, K. Okada and N. Matsushita, *Crystal Growth and Design*, 2011, **11**, 3754-3760.

47. X. Gao, C. Chen, S. Ren, J. Zhang and D. Su, *Cuihua Xuebao/Chinese Journal of Catalysis*, 2012, **33**, 1069-1074.

48. J. Y. Luo, M. Meng, H. Xian, Y. B. Tu, X. G. Li and T. Ding, *Catalysis Letters*, 2009, **133**, 328-333.

49. C. Sun, H. Li and L. Chen, *Energy & Environmental Science*, 2012, **5**, 8475-8475.

50. S. Bernal, J. J. Calvino, M. A. Cauqui, J. M. Gatica, C. Larese, J. A. P. Omil and J. M. Pintado, *Catal. Today*, 1999, **50**, 175-206.

51. N. Acerbi, S. C. E. Tsang, G. Jones, S. Golunski and P. Collier, *Angewandte Chemie (International ed. in English)*, 2013, **52**, 7737-7741.

52. W. J. Shen and Y. Matsumura, *Journal of Molecular Catalysis A: Chemical*, 2000, 165-168.

53. M. Cargnello, J. J. Delgado Jaén, J. C. Hernández Garrido, K. Bakhmutsky, T. Montini, J. J. Calvino Gámez, R. J. Gorte and P. Fornasiero, *Science (New York, N.Y.)*, 2012, **337**, 713-717.

54. A. Trovarelli, *Catalysis Reviews*, 1996, **38**, 439-520.

55. M. M. Forde, L. Kesavan, M. I. bin Saiman, Q. He, N. Dimitratos, J. A. Lopez-Sanchez, R. L. Jenkins, S. H. Taylor, C. J. Kiely and G. J. Hutchings, *ACS Nano*, 2014, **8**, 957-969.

56. O. V. Yazyev and A. Pasquarello, *AIP Conference Proceedings*, 2010, **1199**, 543-544.

57. H. Okatsu, N. Kinoshita, T. Akita, T. Ishida and M. Haruta, *Appl. Catal. A-Gen.*, 2009, **369**, 8-14.

58. Y. Gao, W. Wang, S. Chang and W. Huang, *ChemCatChem*, 2013, **5**, 3610-3620.

5 Catalyst Testing

Contents

5.1 Methane combustion

5.1.1 Introduction

With the high demand for cleaner fuel, methane gas has become an attractive fuel alternative due to its low carbon dioxide emissions as one molecule of methane produces only one molecule of CO_2 (Equation 5.1)[1]. It also benefits from low emission of NO_x[2]. Hence methane natural gas is widely used as fuel for power generation in gas turbine combustion engines and even in natural gas vehicles[2-4]. However, because methane has a greenhouse effect 20 times higher than carbon dioxide[5], the release of unburnt methane presented a problem[4]. Over the last few decades, methane concentration in the atmosphere has increased rapidly with 50-65% of methane emission accounted from power generation[6]. Therefore, there is a need of technologies to react this unburnt methane in the exhausts before it is released into the atmosphere.

However, due to its high thermal stability, the complete combustion of methane requires a high temperature of over 600 °C, which is not feasible with the temperature in the exhausts[7]. Hence catalysts were used to lower the combustion temperature. Combustion of methane over heterogeneous catalysts, in particular noble metal based catalysts, has been extensively studied and Pd based catalysts have proven to be the most active at low temperatures[1, 2, 4, 8]. Metal oxide systems were also attempted, but they showed low activities and required temperatures of more than 500 °C to achieve complete combustion[9, 10]. It is also important that complete combustion is obtained because incomplete combustion resulted in the production of poisonous CO gas (Equation 5.2).

$$CH_4 + 2O_2 \rightarrow CO_2 + 2H_2O \quad \Delta H = -890.2\ kJmol^{-1} \qquad \text{Equation 5.1}$$

$CH_4 + 1.5O_2 \rightarrow CO + 2H_2O \quad \Delta H = -757.0\ kJmol^{-1}$ Equation 5.2

Figure 5.1 shows a proposed Langmuir-Hinselwood type mechanism for the combustion of methane on noble metal catalysts[8, 11]. Under this mechanism, dissociative adsorption of methane produced a methyl or methylene radical by removing hydrogen atoms. As oxygen adsorption is faster than that of methane, the radicals can react with adsorbed oxygen to produce CO_2 with direct oxidation or formaldehyde species. The formaldehyde would then decompose into CO and H and the CO would react with the adsorbed O to produce CO_2.

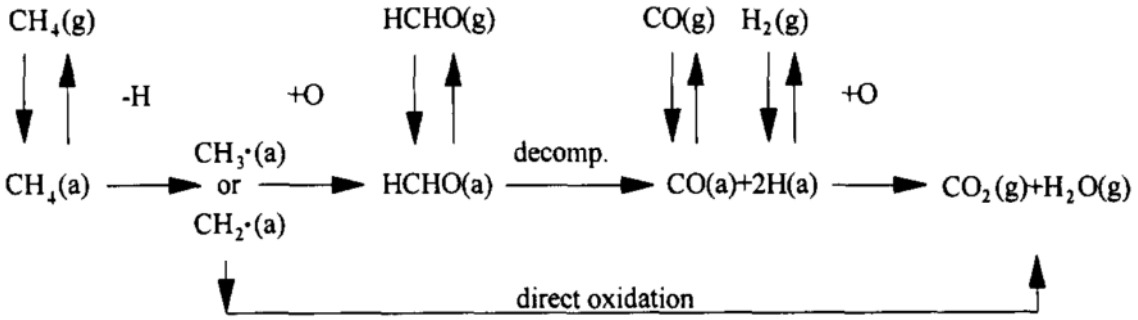

Figure 5.1 Proposed mechanism for the catalytic combustion of methane[11].

The 1% Pd/ceria cubes and rods were tested as catalysts for the methane combustion reaction. The aim was to achieve complete combustion at temperatures lower than 500 °C, thus making the catalysts a possible candidate for exhaust catalysis. To simulate the conditions in the exhaust, the catalysts were tested under oxygen rich conditions, where oxygen is in excess with respect to methane and under oxygen lean conditions where oxygen is the limiting reactant. In addition, with this study, the effect of different surface facets of ceria as the Pd support under the catalytic methane combustion reaction could be investigated.

5.1.2 Experimental details

The catalyst testing on the methane combustion reaction was tested with a continuous flow reactor. Under the oxygen rich conditions, a premixed 0.1% methane in air gas mixture was used, which gave methane to oxygen ratio of 1:200. A flow rate of 30 ml/min was used. Under the oxygen lean conditions, the methane to oxygen ratio of 8:1 was applied. Using mass flow controllers, CH_4, air and N_2 gas were mixed to achieve the total flow rate of 150 ml/min composing of 10.64% of CH_4, 6.65% of air and 82.71% of N_2. The continuous flow reactor was performed at atmospheric pressure. Under both conditions, the gas mixtures were passed through a catalyst fixed bed and the resultant gas was analysed by GC-Methanator with FID detector. More details of the experiment were covered in Chapter 3.

5.1.3 Activation energy

The activation energy study was carried out by running the methane combustion reaction at stepwise temperatures from room temperature to 350 °C. Each percentage conversion point was based of the mean value of 3 consecutive consistent readings from the gas chromatograph to ensure that the reaction has stabilised after the temperature change. The activation energy study was done with a high catalyst to substrate ratio, where 50 mg of sample was used. As the catalyst was in excess, there was a surplus of active sites, hence poisoning effects did not play any significant role.

5.1.3.1 Oxygen Rich Conditions

Figure 5.2 shows the percentage conversion of the catalytic methane combustion at stepwise temperatures. The conversion was 100% selective towards CO_2, as no detectable amount of

CO were produced. Hence, oxygen rich conditions indicated to favour the complete combustion of methane, as expected from a high oxygen content in the reaction mixture.

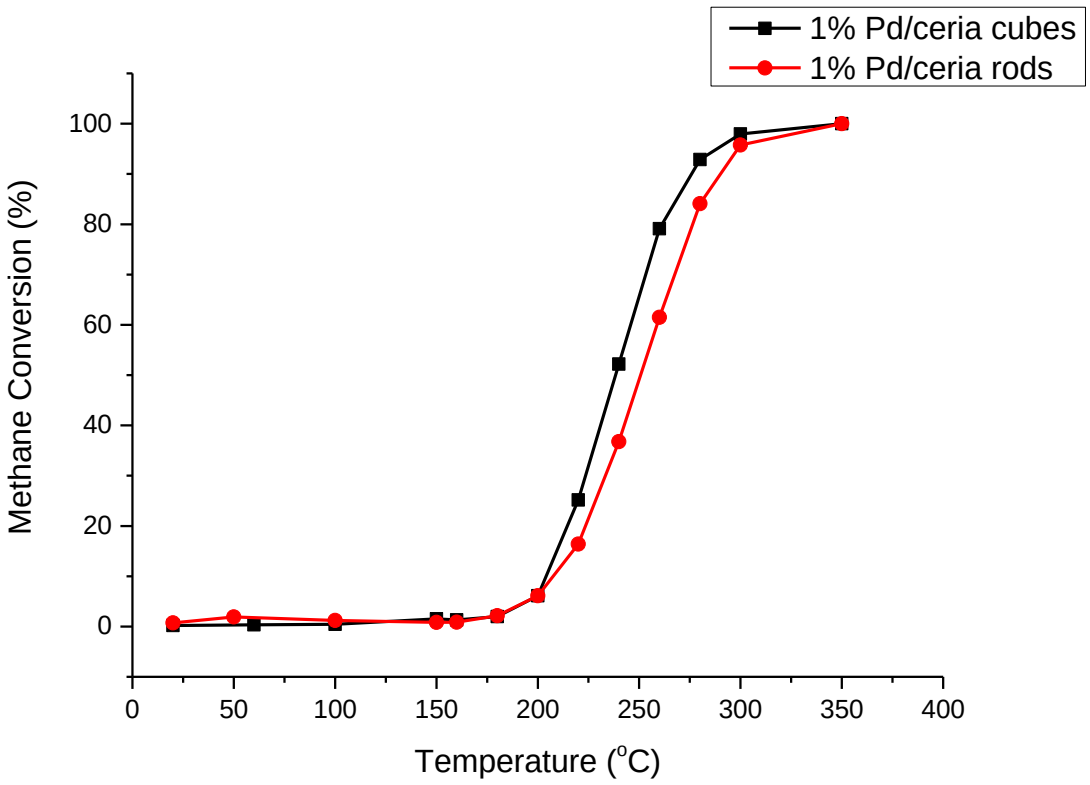

Figure 5.2 Percentage conversion of methane combustion reaction at stepwise temperatures catalysed by 50 mg of 1% Pd/ceria cubes (black) and rods (red) under oxygen rich conditions.

On comparing the 1% Pd/ceria cubes and rods, there was no significant difference in their reaction profiles, although it could be suggested that the 1% Pd/ceria cubes were slightly more active than the rods at temperatures between 220-300 °C. Their reaction profiles indicate that the combustion reactions initiated at around 200 °C and achieved 100% conversion at 350 °C.

Figure 5.3 shows the Arrhenius plot of the reaction profile between 200 °C and 260 °C. The activation energies calculated from the gradients were found to be 89 ± 14 $kJmol^{-1}$ for the 1% Pd/ceria cubes and 81 ± 5 $kJmol^{-1}$ for the 1% Pd/ceria rods. Their similar activation energies

suggested that both of the samples had the same rate determining step. Hence, it is inferred that the different morphologies of the ceria support have a minimal role on the activation energy of methane combustion and that bond cleavage was solely catalysed by the Pd nanoparticles. However, the rate determining step was expected to be the breaking of the C-H bond. When compared to the dissociation enthalpy of C-H bond which is 435 kJmol^{-1} [12, 13], the lower activation energies suggest that the bond breaking was assisted by the catalysts.

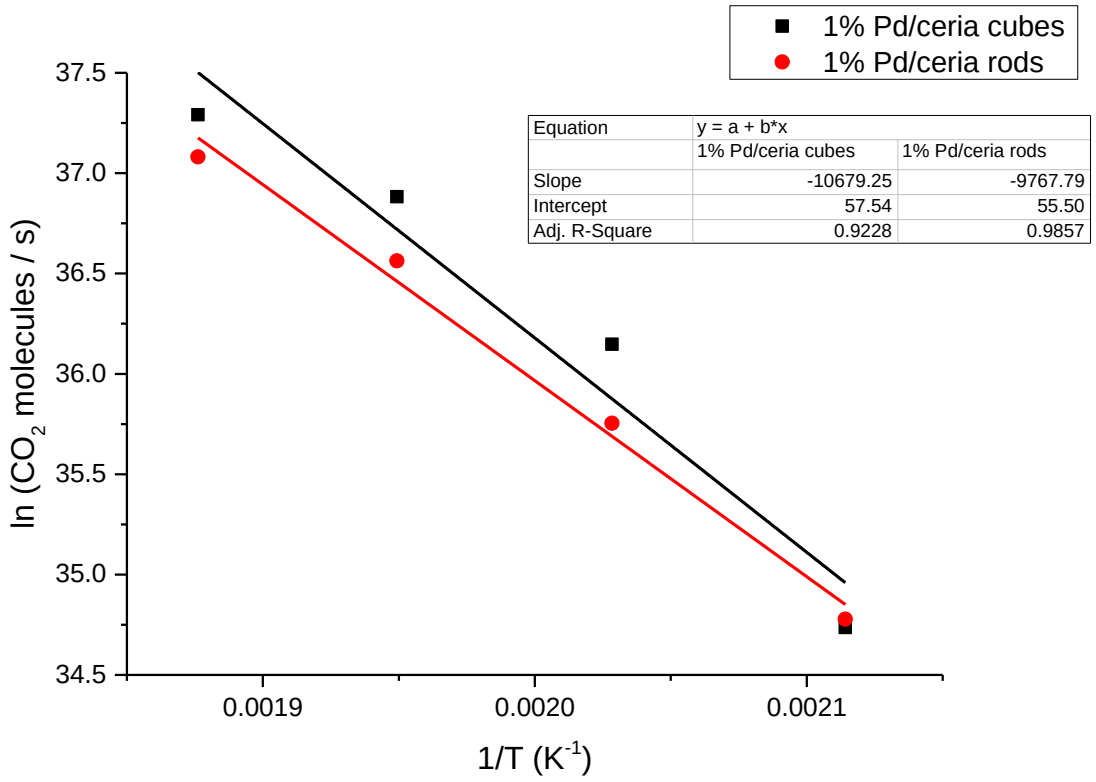

Figure 5.3 Arrhenius plot of the methane combustion reaction profile catalysed by 1% Pd/ceria cubes (black) and rods (red) at temperatures between 200 °C and 260 °C.

5.1.3.2 Oxygen Lean Conditions

Similar to the oxygen rich conditions, the reaction profile of the methane combustion reaction under oxygen lean conditions also began at around 200 °C and achieved maximum conversion at 350 °C for both 1% Pd/ceria cubes and rods (Figure 5.4). As the ratio of methane to oxygen

is 8:1, the methane conversion was limited by oxygen, therefore only a maximum of 6.25% conversion could be reached. Even though the majority of the products were CO_2, small amount of CO production was also observed, which could be due to the incomplete combustion of methane, as oxygen supply was limited (Figure 5.5). The CO production was more apparent at high temperatures, with CO selectivity of 3% reached at 350 °C.

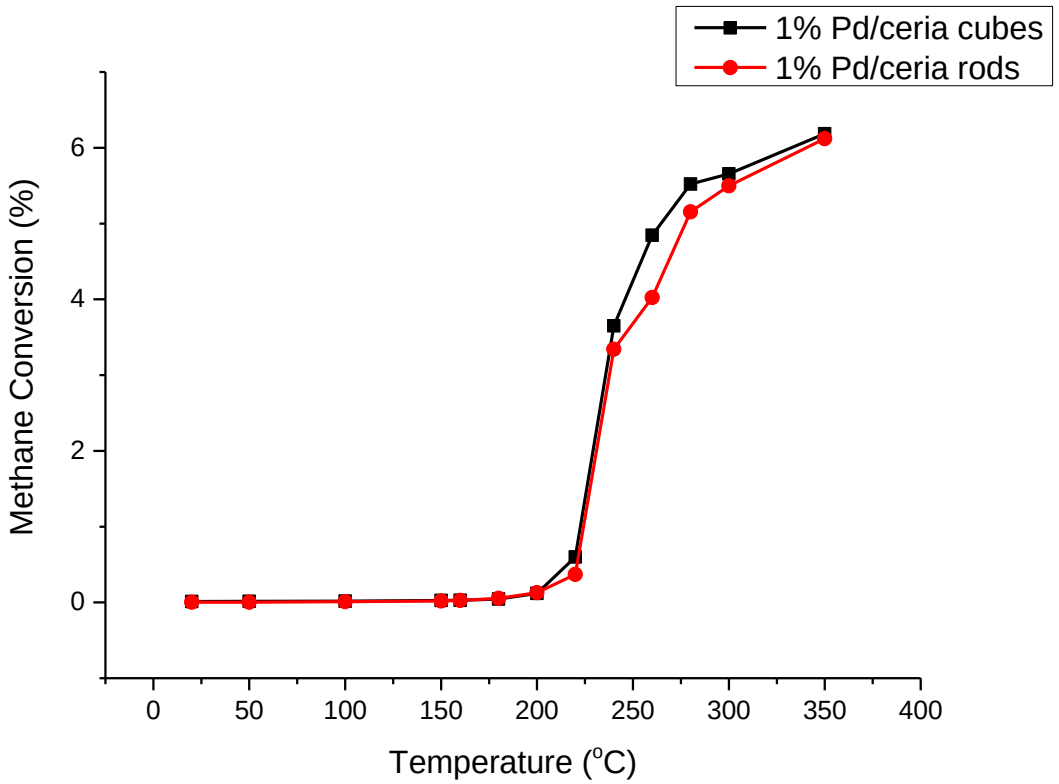

Figure 5.4 Percentage conversion of methane combustion reaction at stepwise temperatures catalysed by 50 mg of 1% Pd/ceria cubes (black) and rods (red) under oxygen lean conditions.

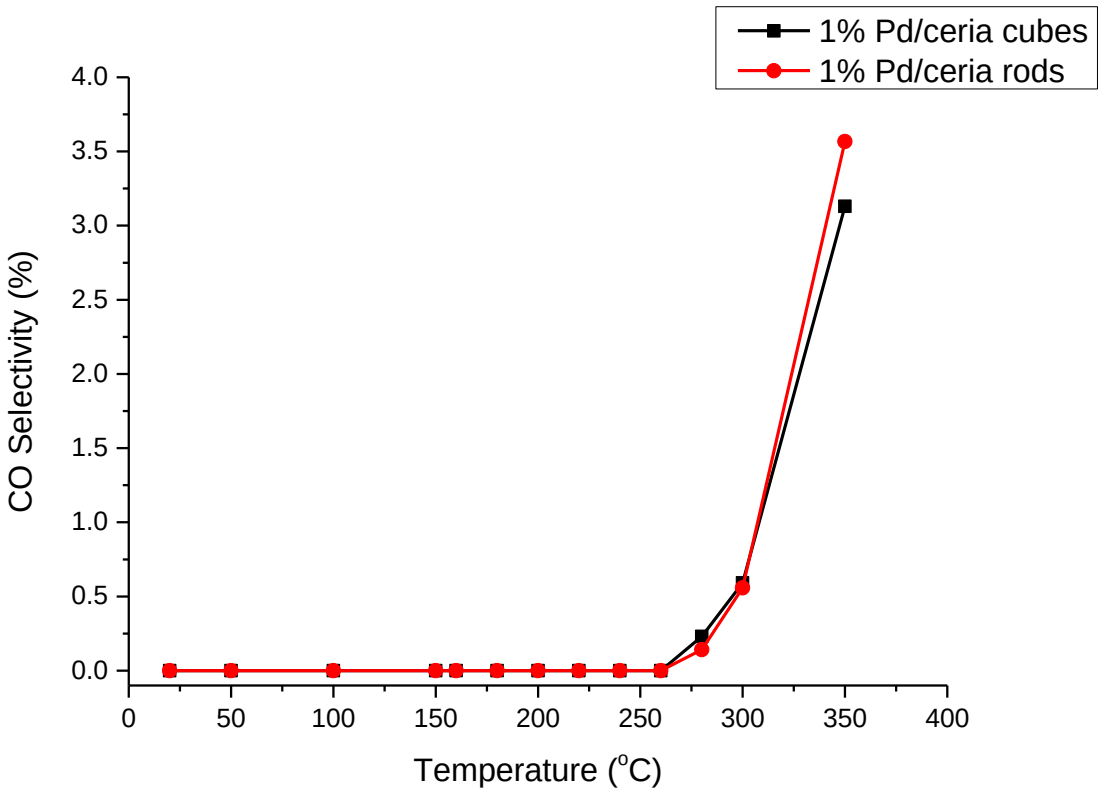

Figure 5.5 Percentage of CO selectivity of methane combustion reaction at stepwise temperatures catalysed by 1% Pd/ceria cubes (black) and rods (red) under oxygen lean conditions.

The Arrhenius plot was taken at the reaction temperatures between 160 – 220 °C for the 1% Pd/ceria cubes and rods and resulted in activation energies of 89 ± 18 kJmol^{-1} and 76 ± 7 kJmol^{-1} respectively (Figure 5.6). Similar to the oxygen rich conditions, within the errors of the calculation, their activation energies suggested to have no significant difference which signified that the reaction underwent the same reaction pathway with both two catalysts. The similarity of the activation energies under the two different conditions also indicated that the same reaction pathway was used irrespective of the oxygen concentration in the reaction.

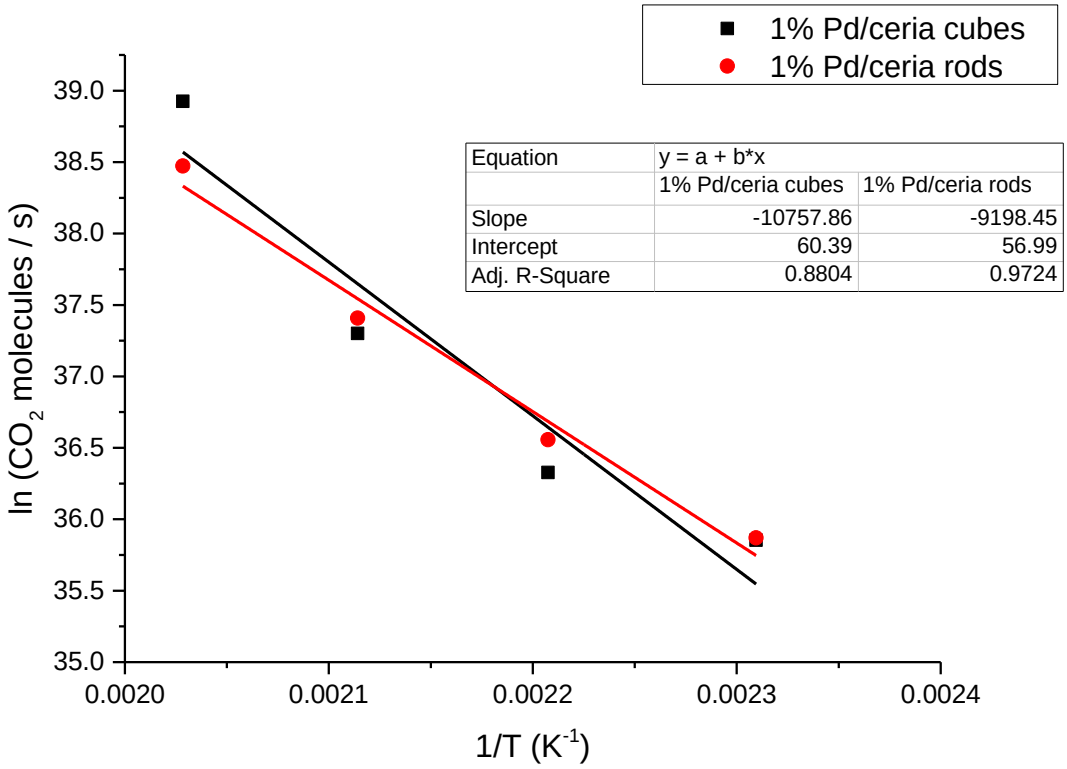

Figure 5.6 Arrhenius plot of the methane combustion reaction profile catalysed by 1% Pd/ceria cubes (black) and rods (red) at temperatures between 160 °C and 220 °C.

5.1.4 Active Site Limitation

The efficiency of a catalyst could only be tested when their active sites were limited and the reactants were in excess. The active sites can be limited by reducing the mass of the catalyst or increasing the proportion of the reactants, hence a high reactant to catalyst ratio was achieved. Under this regime of active site limitation, the conversion rate must be directly proportional to the mass of the catalyst. The direct proportionality between the mass of catalyst and its reaction rates is an indication that the reaction rate is governed by a true chemical step and free from diffusion limitations[14]. In this study, a series of different masses of 1% Pd/ceria cubes was used while the reactants flow rates were kept constant. The temperature of 350 °C was used as the activation energy studies showed that maximum conversion was achieved at that temperature.

For each mass of catalyst, the reaction was allowed to settle for 30 minutes before the gas product analysis was taken. A series of measurements were made until 3 consecutive consistent readings of the gas chromatograph were measured to ensure that the reaction had stabilised.

5.1.4.1 Oxygen Rich Conditions

Under oxygen rich conditions, the 1% Pd/ceria cubes catalyst remained active site limited from 0 mg up to 5 mg of catalysts (Figure 5.7). Although 100% conversion was not achieved at 5 mg, the direct proportionality between the mass and conversion did not withstand at masses larger than 5 mg, as the conversion rates started to plateau. Hence, due to the small concentration of methane at 30 ml/min flowrate, only 5 mg of 1% Pd/ceria cubes, corresponding to 0.05 mg of Pd nanoparticles, were needed to saturate the reaction with active sites.

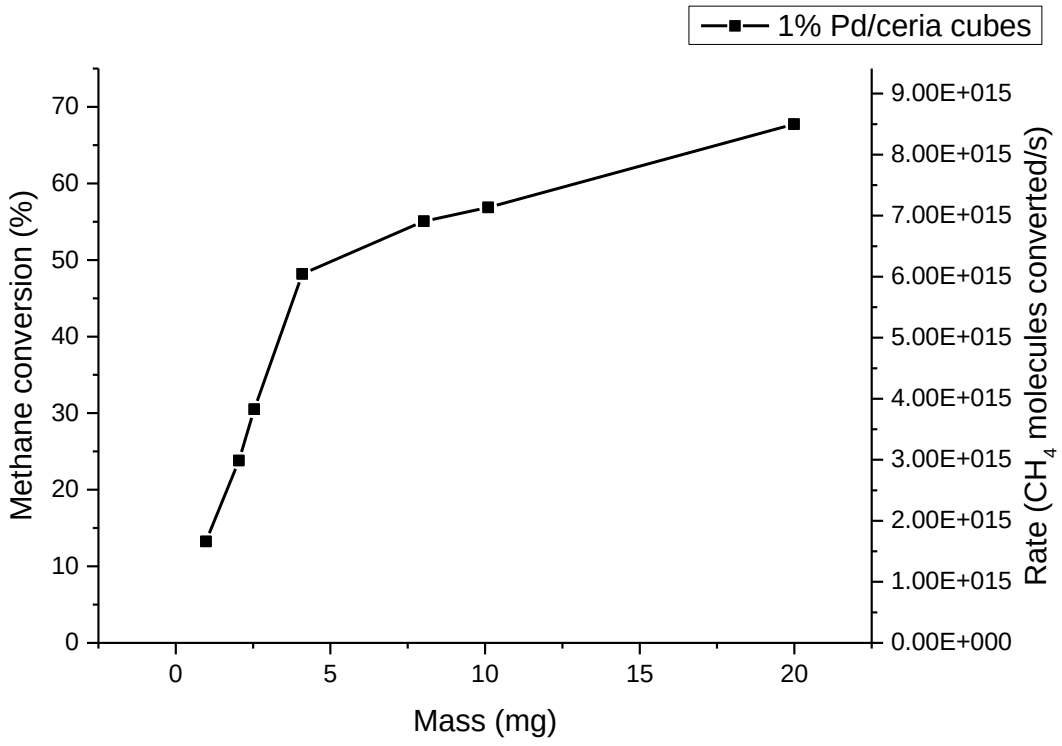

Figure 5.7 Percentage conversion and rates of methane combustion reaction catalysed by 1% Pd/ceria cubes of different masses under oxygen rich conditions at 350 °C.

5.1.4.2 Oxygen Lean Conditions

The active site limitation study was also performed under oxygen lean conditions, using the same catalyst, 1% Pd/ceria cubes (Figure 5.8). With a higher flow rate and also higher methane concentration compared to the oxygen rich conditions, the methane conversion was directly proportional to the catalyst mass from 0 mg until 25 mg, which correlated to 0.25 mg of Pd nanoparticles. As the mass increased beyond 25 mg, the conversion rate started to level off until maximum conversion of 6.25 % was attained with 72 mg of catalysts.

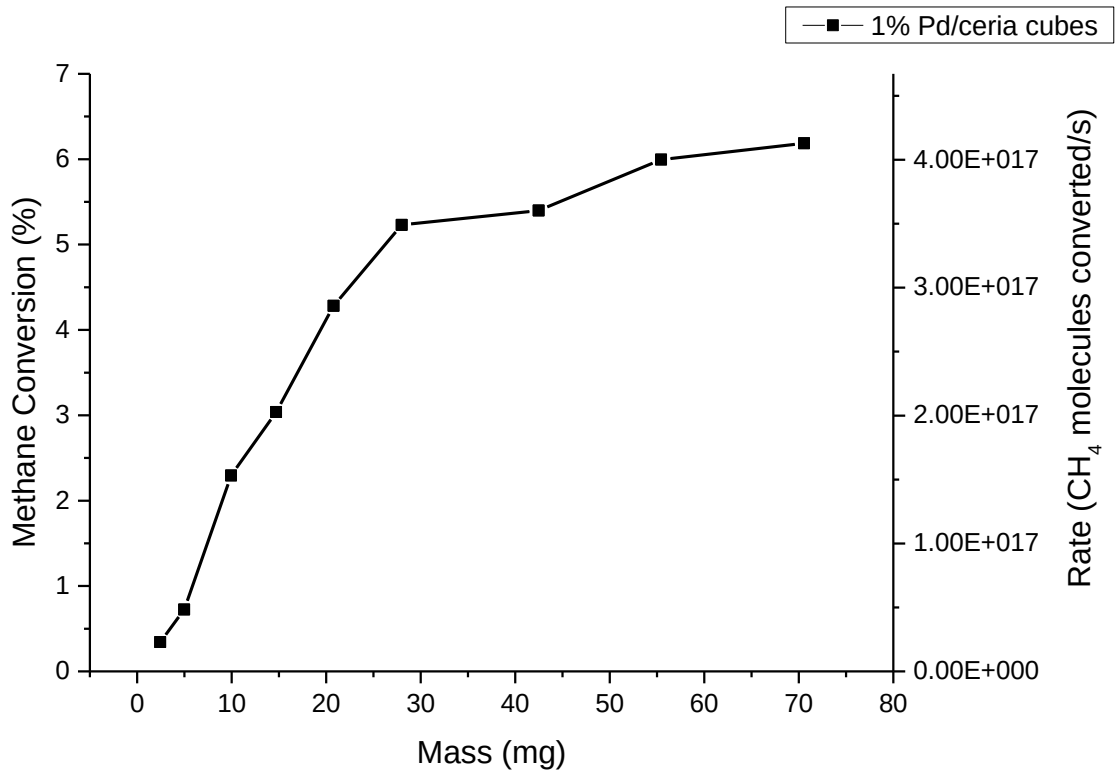

Figure 5.8 Percentage conversion and rates of methane combustion reaction catalysed by 1% Pd/ceria cubes of different masses under oxygen lean conditions at 350 °C.

5.1.5 Deactivation Test

The durability of the catalysts was investigated by running the methane combustion reaction for a prolonged period of time and using a catalyst mass where active sites were limited. In this case, the reaction were considered to achieve 'steady state' and poisoning effects had to be taken into consideration. The reaction was left to run for 24 hours, where the gas products were analysed by GC at 10 minutes intervals until 300 minutes. Another series of gas analyses were taken after 24 hours. As a control, the catalysts were also compared against 1% Pd/C, a catalyst with similar Pd particle size and where metal support interaction was absent, as the C support was known to be inert.

5.1.5.1 Oxygen Rich Conditions

For the oxygen rich conditions, the reaction was performed at 350 °C with 2 mg catalyst samples. According to the active site limitation study, 2 mg of catalyst at that temperature would result in 23% methane conversion. From figure 5.9, all the catalyst experienced apparent deactivation, especially the 1% Pd/C, being completely deactivated in less than 200 minutes after the start of the reaction.

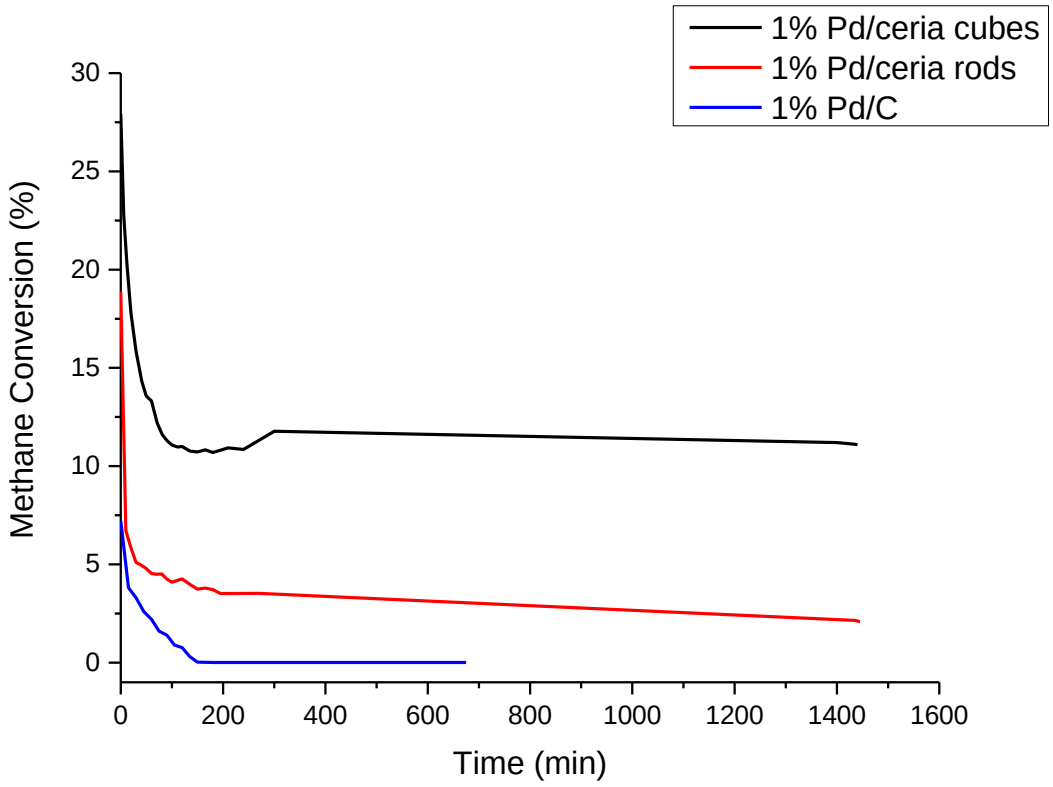

Figure 5.9 Percentage conversion with time of methane combustion reaction catalysed by 2 mg of 1% Pd/ceria cubes (black), rods (red) and 1% Pd/C (blue) under oxygen rich conditions at 350°C.

However, both 1% Pd/ceria cubes and rods did not suffer complete deactivation. Both reached a ‘steady state’ after 100 minutes when the conversion rate then remained constant throughout. The 1% Pd/ceria cubes settled at a conversion of 11% compared to the 1% Pd/ceria rods at 3%

conversion. These conversions corresponded to the turnover frequency (TOF) of 0.0449 s^{-1} and 0.0118 s^{-1} respectively. By comparison, the catalyst with cubes support performed nearly 4 times more active than with rods support and the results also indicated that 1% Pd/ceria cubes could withstand poisoning better than the rods.

5.1.5.2 Oxygen Lean Conditions

For oxygen lean conditions, 20 mg of catalyst samples were used. From active sites limitation study, a conversion of roughly 4% was expected with this amount of catalyst. Similar to the oxygen rich conditions, the 1% Pd/ceria cubes indicated to outperform the rods while the control catalyst, 1% Pd/C was completely deactivated after 400 minutes (Figure 5.10). Both the 1% Pd/ceria samples settled into their steady state after 200 minutes where the cubes and rods maintained the conversions of 2.9% and 2% respectively, as opposed to the expected 4%. The conversion rates correlated to TOF of 0.844 s^{-1} for the 1% Pd/ceria cubes and 0.470 s^{-1} for the 1% Pd/ceria rods. This suggested that the Pd catalyst with the ceria cubes support performed nearly 2 times better than the one with rods support. From the activation energy study, oxygen lean conditions was shown to produce CO which could poison the Pd catalyst. However, both the Pd/ceria cubes and rods catalysts indicated to be resistant from complete deactivation by CO.

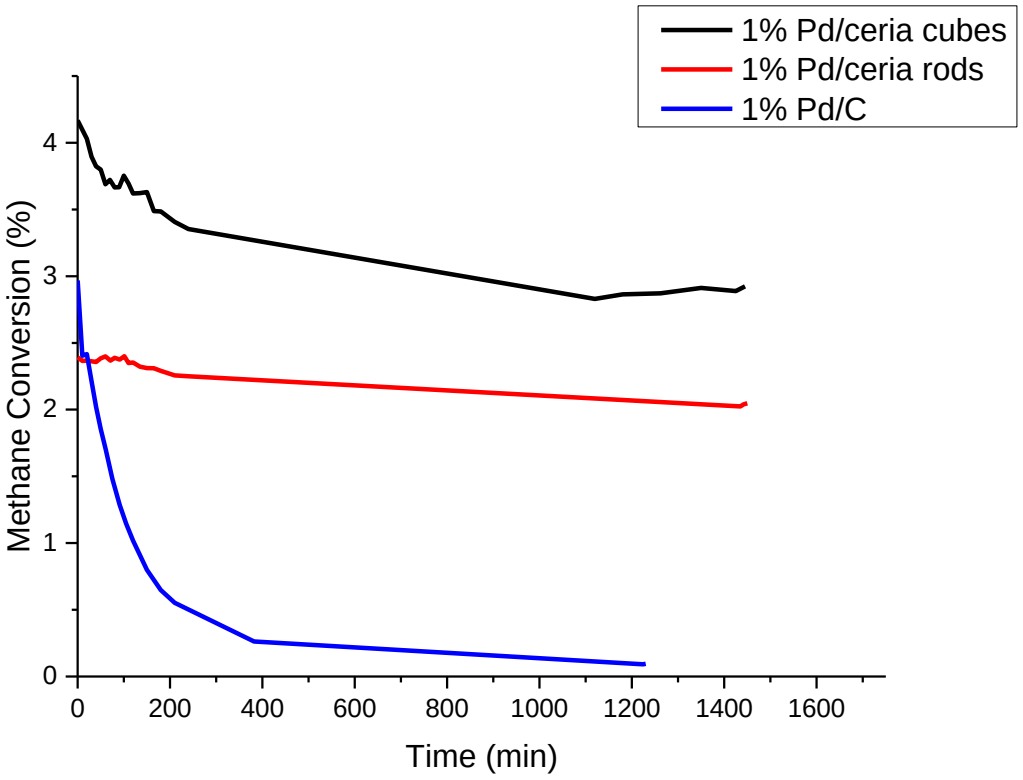

Figure 5.10 Percentage conversion with time of methane combustion reaction catalysed by 20 mg of 1% Pd/ceria cubes (black), rods (red) and 1% Pd/C (blue) under oxygen lean conditions at 350°C.

5.1.6 Discussion

In general, both the catalysts were able to achieve complete combustion at 350 °C, under both oxygen rich and lean conditions. It was also indicated that the ceria support could prevent them from being completely deactivated, especially the 1% Pd/ceria cubes which indicated that the deactivation was minimal.

As water is one of the main products of methane combustion, water poisoning was argued to be the biggest factor in deactivation of the catalyst, especially in oxygen lean conditions, due to the formation of $Pd(OH)_2$[1, 15, 16]. With ceria as a support, this water poisoning was not apparent, compared to the deactivation observed by 1% Pd/C. This might be due to the ceria

acting as an excellent oxygen storage reservoir and oxygen mobility properties, which promotes oxidation of the hydroxide anion. As 1% Pd/ceria cubes experienced lower deactivation compared to rods, it could be suggested that the (100) surface on the cubes facilitates the oxidation process more than the (110) surface on the rods. This oxidation process by the oxygen of ceria could also explain the minimal effect of CO poisoning, as the oxygen from the support could be used to oxidise the CO. Furthermore, ceria has been known to catalyse the oxidation of CO[17-19].

5.2 Gas Phase Formic Acid Decomposition

5.2.1 Introduction

Formic acid is a popular probe molecule for catalyst studies due to its simple chemical structure, hence it was one of the first adsorbates used to investigate Sabatiers' principle[20]. Because of its acidic properties, formic acid has also been used to probe basic sites on catalysts[21]. However, in the last decade, there has been a renewed interest in formic acid as material for hydrogen storage[22, 23].

Currently, due to the huge demand in clean energy technologies, hydrogen fuel has been one of the strongest contender to replace carbon based fuel, as it has zero carbon footprint and emits the harmless non-greenhouse product, water[24]. However, the biggest challenge faced by hydrogen fuel technology is its logistics. Hydogen being in the gas state at standard temperature and pressure imposed a problem for transportation and storage[25].

Various techniques have been attempted to rectify this problem which include high pressure storage cylinders and liquefied hydrogen[26, 27]. However, these methods had to resort to transporting and storing hydrogen under high pressure which is dangerous. Therefore, chemical methods have been explored where hydrogen can be used to synthesise a molecule, to 'store' the hydrogen and these chemicals are then decomposed to give out the stored hydrogen. Examples of well-known chemicals used for this purpose are borohydrides, hydrazine and formic acid, which are all in liquid state in standard temperature and pressure[25, 27].

One advantage of using formic acid as a hydrogen storage material is that hydrogen can be stored and released easily. The main decomposition products are H_2 and CO_2, which can be

released safely into the atmosphere[25]. Whereas other materials such as borohydride systems, the dehydrogenated products must be retained for subsequent rehydrogenation. Formic acid also benefits from being a carbon neutral process in the cycle of hydrogen storage and evolution (Figure 5.11).

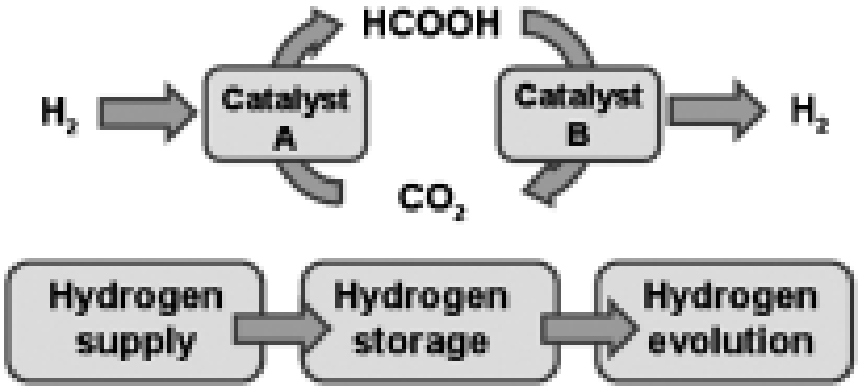

Figure 5.11 Hydrogen storage cycle of formic acid[25].

As most methods of producing formic acid from CO_2 involves homogeneous catalysts (Catalyst A)[25, 28], the decomposition of formic acid on the other hand, requires the use of heterogeneous catalysts (Catalyst B)[23, 25, 29-31]. Formic acid is known to decompose via 2 reactions: dehydrogenation and dehydration (Equations 5.3 and 5.4)[23]. As formic acid was aimed to be used as hydrogen storage materials, it is important for the catalyst to be selective towards the dehydrogenation process, thus maximising the hydrogen evolution. Selectivity towards the dehydrogenation process also limits the production of CO through the dehydration process, which is toxic to be released into the atmosphere and could possibly poison the catalyst.

Dehydrogenation:	$HCOOH \rightarrow H_2 + CO_2$	$\Delta G = -48.4\ kJmol^{-1}$	Equation 5.3
Dehydration:	$HCOOH \rightarrow H_2O + CO$	$\Delta G = -28.5\ kJmol^{-1}$	Equation 5.4

Other than selectivity, the catalyst is also required to decompose formic acid at a low temperature, thus making the process more economical. Noble metal based catalyst have shown to suit these criteria, in particular Pd based catalysts which showed spectacular activity and selectivity for formic acid decomposition[23]. Other catalyst materials have also been tested, such as metal oxide systems, however with these catalysts, the decomposition of formic acid could only be achieved at temperatures higher than 300 °C[32, 33], which is not ideal.

As Pd based catalyst have been shown to have promising reactivity towards the formic acid decomposition reaction, the performance of the 1% Pd/ceria cubes and rods were tested in a gas-phase formic acid decomposition reaction. It was aimed that these catalysts can decompose formic acid at low temperatures and also be selective towards the dehydrogenation reaction, thus making them a viable catalyst for this reaction. In addition, the effect of varying the surface of the ceria support had on this reaction could be investigated.

5.2.2 Experimental details

The detailed experimental method is covered in Chapter 3. The gas phase formic acid decomposition reaction was performed with a continuous flow reactor. In short, inert carrier gas, N_2 at 40 ml min^{-1}, was passed through a saturator of formic acid under isothermal temperature of 5 °C which resulted in 1.7% formic acid composition in N_2 mixture at atmospheric pressure. The reaction gas mixture was passed through a fixed bed containing the catalyst. The gas products were fed into GC-TCD to analyse the reaction products.

5.2.3 Activation Energy

The activation energy of the catalytic formic acid decomposition reaction was tested by performing the reaction at stepwise temperatures from room temperature until total conversion was obtained. For this study, a low reactant to catalyst ratio was used so poisoning effects could be disregarded as there was a surplus of active sites available. Hence, a catalyst mass of 50 mg was used. For each temperature, the reaction was allowed to stabilise for 30 minutes before a series of GC measurements were taken to analyse the reaction products. Figure 5.12 shows the reaction profiles of the formic acid decomposition reaction catalysed by 1% Pd/ceria cubes and rods. Both of the catalysts had similar reaction profiles, where the light off temperature occurred at 40 °C. The 1% Pd/ceria rods appeared to achieve full conversion at 100 °C compared to 120 °C for the cubes. However, when compared to a blank test, there was no conversion observed up to 300 °C. Therefore, the formic acid decomposition was definitely catalysed as the reaction temperature was significantly lowered by the catalysts.

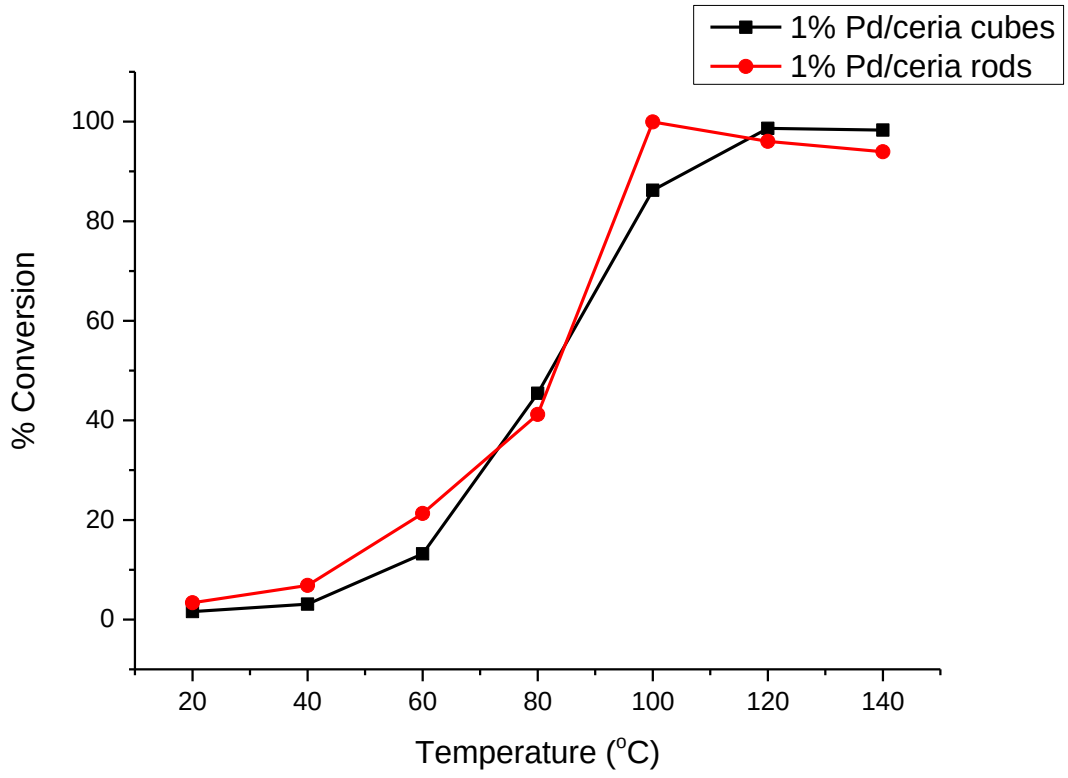

Figure 5.12 Percentage conversion of gas phase formic acid decomposition reaction catalysed by 50 mg of 1% Pd/ceria cubes (black) and rods (red) at stepwise temperatures.

From their Arrhenius plots in the range of the light off temperatures (20 °C - 80°C) (Figure 5.13), the activation energies calculated from their gradients corresponded to 48 ± 7 $kJmol^{-1}$ for the 1% Pd/ceria cubes and 43 ± 5 $kJmol^{-1}$ for the rods, which showed no significant difference between the two catalysts. Hence, their similar activation energies signified that the reaction pathway was the same for both catalysts. This similarity in their activation energy suggested that changing the morphologies has minimal effect on the rate determining step of the reaction.

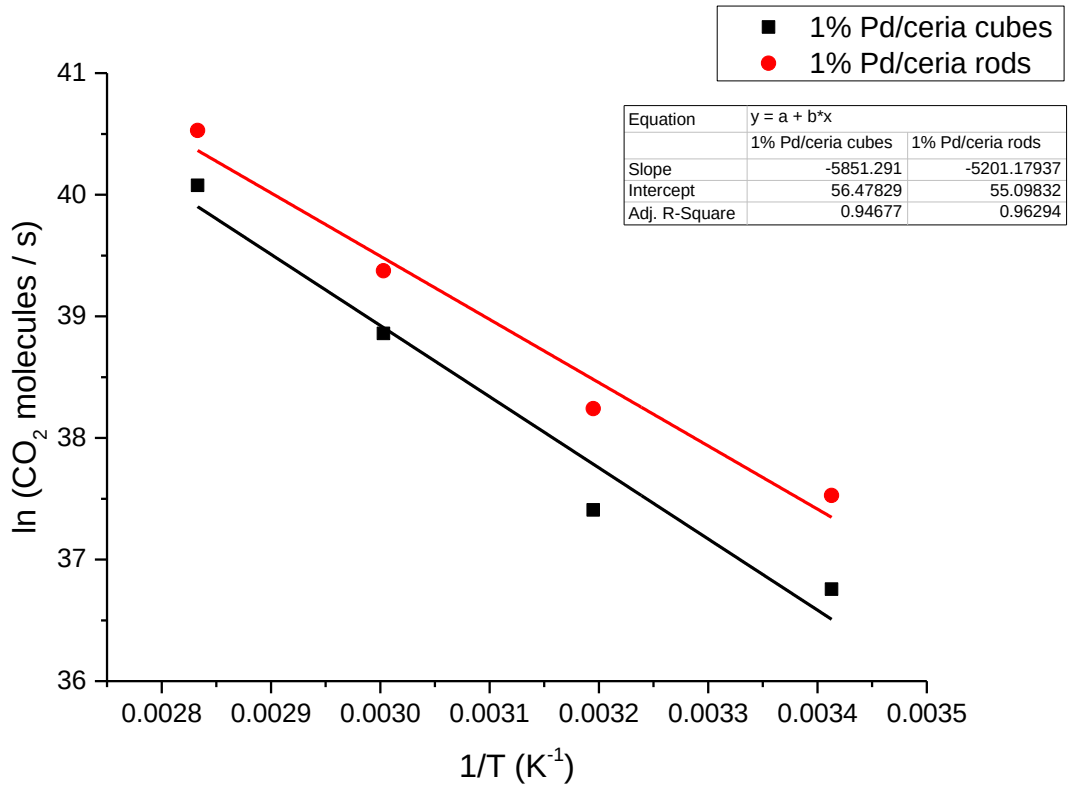

Figure 5.13 Arrhenius plots gas phase formic acid decomposition reaction of catalysed 1% Pd/ceria cubes (black) and rods (red) at temperatures 20-80 °C.

The rate determining step for formic acid decomposition was found to be the breaking of C-H bond[23, 34]. In the study by Tsang et. al., the labelled DCOOH formic acid resulted in 1.5 times decrease in the reaction rate, which is a typical kinetic isotope effect[23]. The acidic proton (O-H) was also exchanged with a deuterated proton, however the kinetic isotope effect was not observed signifying that the cleavage of O-H bond was not the rate determining step. Hence, with the activation energies of the formic acid decomposition found to be 48 $kJmol^{-1}$ and 43 $kJmol^{-1}$ for 1% Pd/ceria cubes and rods respectively, these results suggested that both samples catalysed the reaction, when compared to the energy required for breaking the C-H bond which is 435 $kJmol^{-1}$.

Throughout the whole series of temperatures tested, the majority of the products were CO_2 and H_2 which indicated that the dehydrogenation reaction was favoured as opposed to the dehydration reaction. However, the dehydration reaction became more apparent as the temperature was increased and CO production was observed (Figure 5.14). The CO production seemed to be more distinctive for the 1% Pd/ceria rods where a maximum dehydration selectivity of 6.7% was observed compared to a maximum of 3.8% for the cubes at 140 °C.

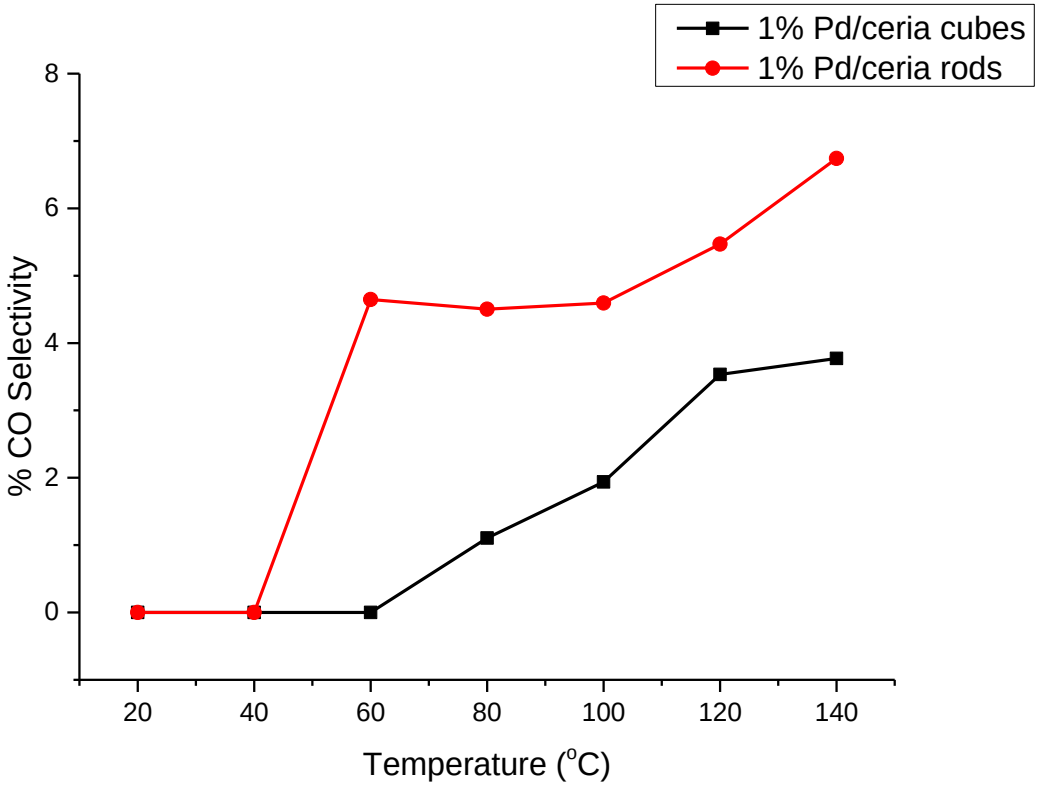

Figure 5.14 Percentage CO selectivity of gas phase formic acid decomposition reaction catalysed by 50 mg of 1% Pd/ceria cubes (black) and rods (red) at stepwise temperatures.

From FT-IR study, it was revealed that when formic acid was adsorbed onto metal surfaces, it dissociated and formed a formate species as an intermediate[35, 36]. The formate species generally bind onto the metal surfaces by two major binding modes: bridging and monodentate modes (Figures 5.15 a and b). The bridging mode where the formate was bound through two of the

oxygen atoms was argued to be the intermediate for of the dehydrogenation reaction whereas the monodentate mode where the formate was bound through a single oxygen atom was the intermediate of the dehydration reaction. The proportions of the monodentate and bridging modes of formic acid was dependent on the coordination sites of the Pd metal, as low coordinated surface sites preferred the monodendate mode whilst high coordinated sites preferred the bridging modes. However, it was shown that the Pd nanoparticles were similar in both of the ceria cubes and rods support. Hence their CO selectivities should also be similar, however this did not agree with the observed results.

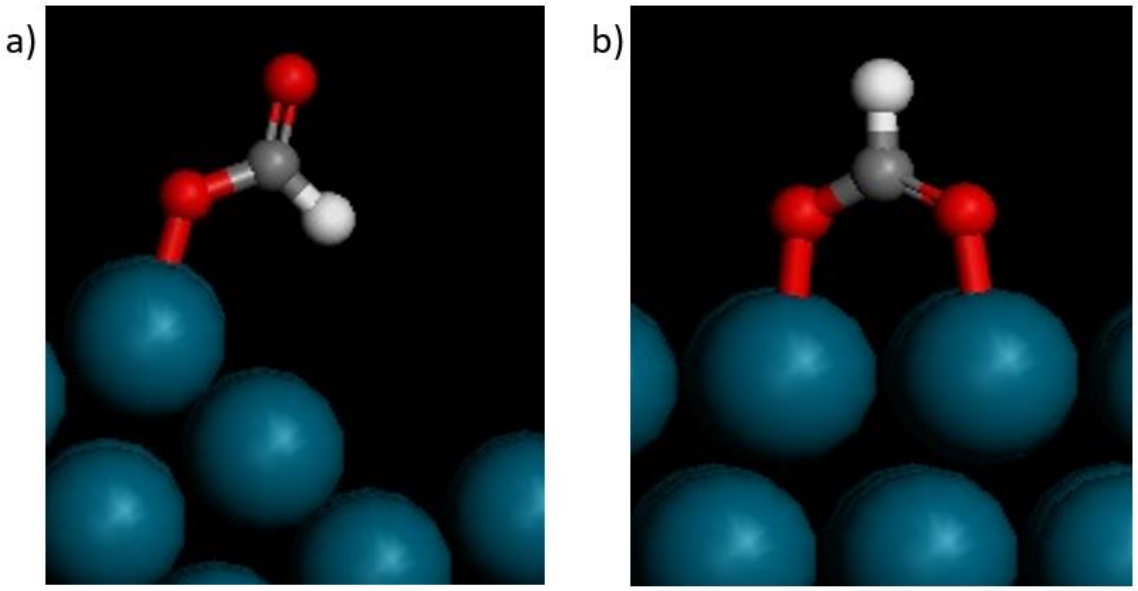

Figure 5.15 Binding modes of formate on a metal nanoparticle surface: a) Monodentate mode b) Bridging mode.

5.2.4 Active Site Limitation

Other than investigating the working temperature of these catalysts in the gas phase formic acid decomposition reaction, their active sites limitations also needed to be studied so their active sites could be maximised and high reactant to catalyst ratio could be achieved, thus maximising

efficiency. Different masses of 1% Pd/ceria cubes were used until the active sites were saturated, in which the conversion and the mass of catalyst were no longer directly proportional. The temperature of 150 °C was used for this active site limitation study.

Figure 5.16 showed that full conversion was obtained when 8 mg of catalyst was used and there was direct proportionality observed between the conversion and catalyst mass at masses below 8 mg. Therefore, to maximise the active sites under this reaction conditions, a catalyst mass of lower than 8 mg must be used.

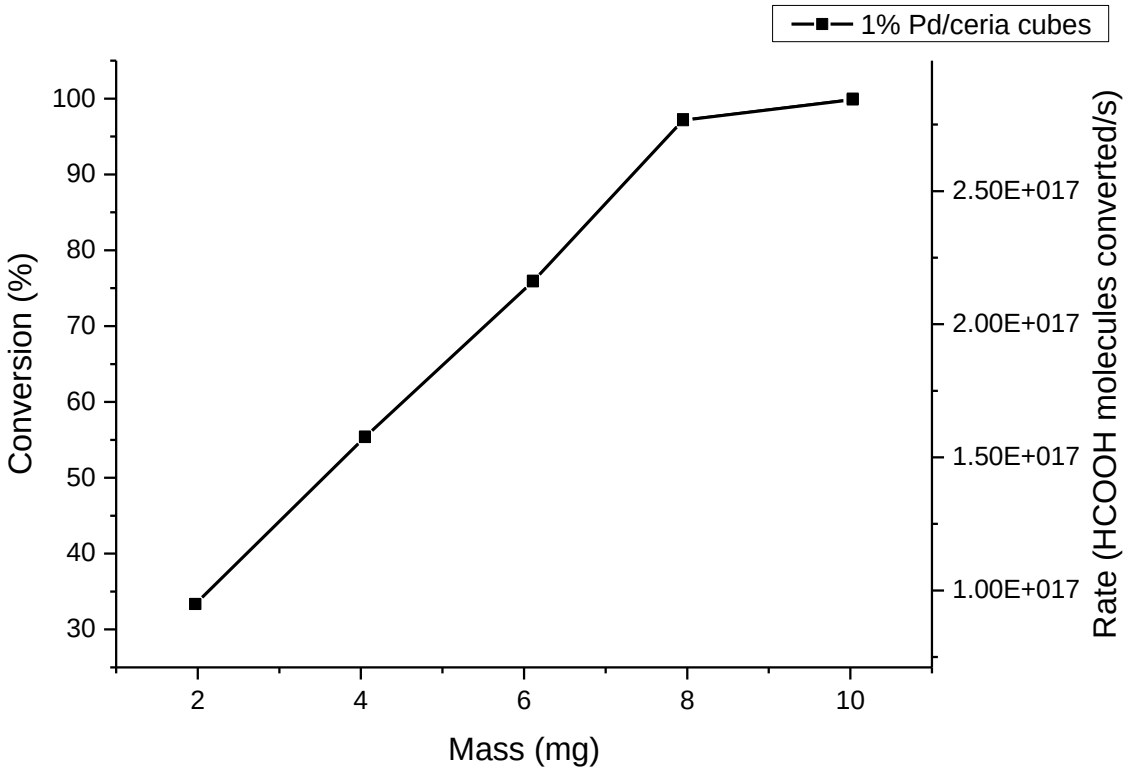

Figure 5.16 Percentage conversion and rates of gas phase formic acid decomposition reaction catalysed by 1% Pd/ceria cubes of different masses at 150 °C.

5.2.5 Deactivation Test

From the activation energy study, it was found that CO production via the dehydration reaction was more pronounced as the reaction temperature was increased. As CO could poison the catalyst, even at low concentrations, the susceptibility of the catalysts to the CO poisoning must be tested. The gas phase formic acid decomposition reaction was operated at 150 °C to maximise the CO production, hence the poisoning effects could be observed. For this test, a catalyst mass of 6 mg was used, where the reactants were in excess relative to the active sites.

To investigate the durability of the 1% Pd/ceria cubes and rods catalysts, the reaction was left to run over a period of 24 hours. Their reactivity was also compared with 1% Pd/C as a control catalyst, where there was no metal-support interaction due to the inert nature of the carbon support. Both the 1% Pd/ceria cubes and rods settled into their respective constant conversion rates after 100 minutes of reaction, which could be considered their 'steady state' (Figure 5.17). In comparison, the 1% Pd/C, appeared to deactivate instantly. Hence this signified the role of the ceria support preventing the catalyst from CO poisoning. The 1% Pd/ceria cubes, with 'steady state' conversion of 70% suggested to be more resistant to CO compared to the rods with a 62% conversion. Their conversion rates corresponded to the TOF of 1.997 s^{-1} and 1.571 s^{-1} respectively. Furthermore, when compared to the data obtained from the active site limitation study, a catalyst mass of 6 mg corresponded to the conversion of 73.9%, therefore the poisoning effect on the 1% Pd/ceria cubes appeared to be minimal.

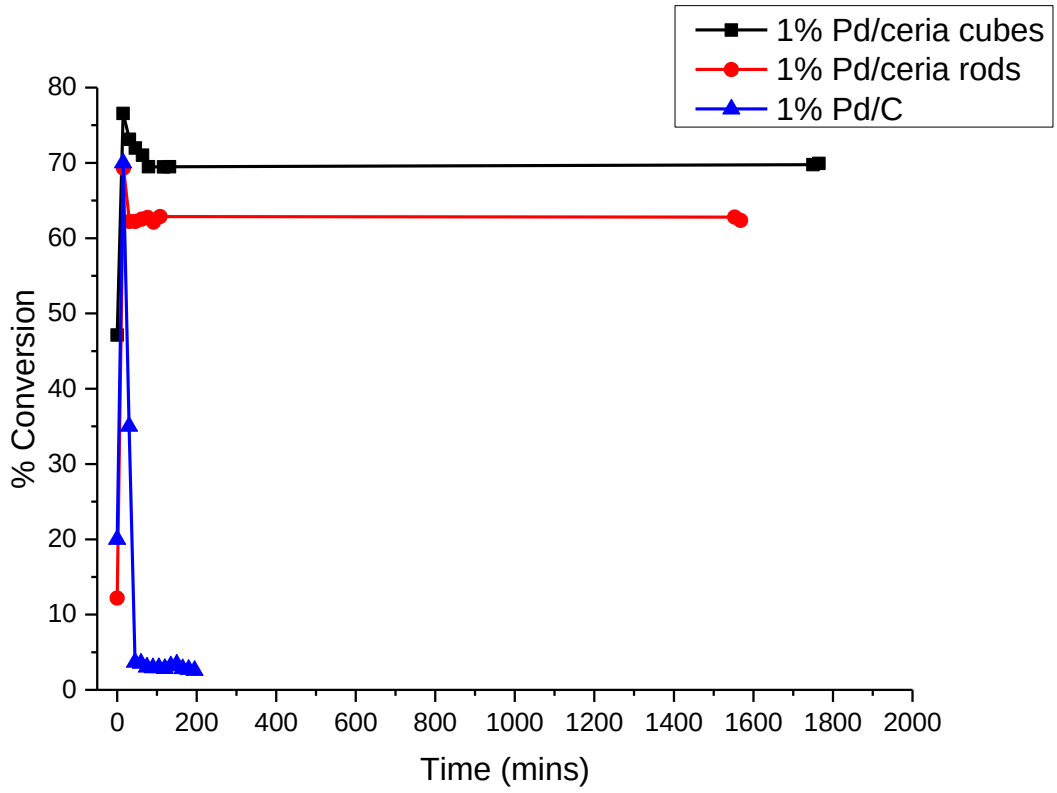

Figure 5.17 Percentage conversion with time of gas phase formic acid decomposition reaction catalysed by 6 mg of 1% Pd/ceria cubes (black), rods (red) and 1% Pd/C (blue) at 150°C.

5.2.6 Discussions

Both of the 1% Pd/ceria cubes and rods catalysts were able to decompose formic acid with their light off temperature at 40 °C and achieved complete decomposition at 120 °C. They also showed high selectivities towards the dehydrogenation reaction. These catalyst characteristics made both of these catalysts a promising catalyst for gas phase formic acid decomposition. Furthermore, both catalysts appeared to catalyse the reaction as their activation energies were much lower than the energy needed for C-H cleavage, which is the rate determining step.

Both catalysts appear to show resistance to deactivation by the CO poisoning, as usually the presence of CO in ppm level would be enough to poison a metal catalyst[37, 38]. This behaviour

was particularly apparent on the 1% Pd/ceria cubes as it signified minimal deactivation when the reaction had been running for 24 hours. The ceria cubes with the (100) surface and rods with the (110) surface might play a significant role in preventing the catalyst from being poisoned by CO, as when compared to an inert C support, the catalyst was deactivated immediately.

A similar characteristic was also observed in the catalytic methane combustion reaction, where the catalyst with the cubes support showed less deactivation and poisoning compared to the rods. This could be attributed to the oxygen mobility of the ceria with the surface oxygen was used to 'clean' the poison molecules off the Pd surface. The use of these mobile surface oxygen was also observed in previous studies in other catalysed reactions such as CO oxidation and soot combustion reactions[39-42].

The cleaning mechanism appeared to be dependent on the oxygen mobility of different ceria, which is determined by the ceria surfaces. Hence, the difference in oxygen mobility between the (100) surface in ceria cubes and (110) surface in rods might be the reason why the catalyst reached different conversion rates as 'steady state'. During the 'steady state', the rate of poisoning and the rate of cleaning by the ceria supports reached an equilibrium and the faster rate of cleaning would result in less poisoning of the Pd nanoparticles, therefore higher conversion rates and TOF (Figure 5.18). Since the rate of cleaning is attributed to the oxygen mobility of the ceria, the catalyst testing studies suggested that the (100) surface had faster oxygen mobility than the (110) surface.

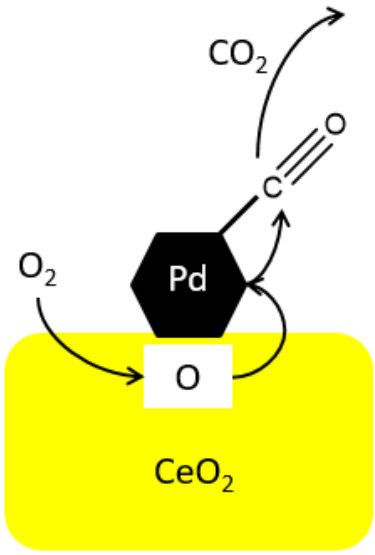

Figure 5.18 Proposed mechanism of the poison cleaning on the Pd nanoparticle by the ceria surface oxygen.

5.3 References

1. D. Ciuparu, M. R. Lyubovsky, E. Altman, L. D. Pfefferle and A. Datye, *Catalysis Reviews*, 2002, **44**, 593-649.
2. P. Gélin and M. Primet, *Applied Catalysis B: Environmental*, 2002, **39**, 1-37.
3. F. Arosio, S. Colussi, a. Trovarelli and G. Groppi, *Applied Catalysis B: Environmental*, 2008, **80**, 335-342.
4. M. Cargnello, J. J. Delgado Jaén, J. C. Hernández Garrido, K. Bakhmutsky, T. Montini, J. J. Calvino Gámez, R. J. Gorte and P. Fornasiero, *Science (New York, N.Y.)*, 2012, **337**, 713-717.
5. *Climate Change 2007: The Physical Science Basis*, Cambridge University Press, 2007.
6. D. Q. T. F. Stocker, G. K. Plattner, M. Tignor, S. K. Allen, J. Boschung, A. Nauels, Y. Xia, V. Bex and M. P. M., *Climate Change 2013: The Physical Science Basis. Contribution of Working Group I to the Fifth Assessment Report of the Intergovernmental Panel on Climate Change*, 2013.
7. A. J. Zarur and J. Y. Ying, *Nature*, 2000, **403**, 65-67.
8. J. H. Lee and D. L. Trimm, *Fuel Processing Technology*, 1995, **42**, 339-359.
9. M. Sun, G. Zou, S. Xu and X. Wang, *Materials Chemistry and Physics*, 2012, **134**, 912-920.
10. R. B. Anderson, K. C. Stein, J. J. Feenan and L. J. E. Hofer, *Industrial and Engineering Chemistry*, 1961, **53**, 809-812.
11. S. H. Oh, P. J. Mitchell and R. M. Siewert, *METHANE OXIDATION OVER NOBLE-METAL CATALYSTS AS RELATED TO CONTROLLING NATURAL-GAS VEHICLE EXHAUST EMISSIONS*, Amer Chemical Soc, Washington, 1992.
12. D. Shriver and P. Atkins, *Inorganic Chemistry*, Oxford University Press, 4th edn., 2006.

13. D. R. Lide and H. P. R. Frederikse, *CRC Handbook of Chemistry and Physics*, CRC, 78th edn., 1997.

14. G. C. Bond, *Heterogeneous Catalysis: Principles and Applications*, Oxford Science Publications, 2 edn., 1986.

15. W. R. Schwartz, D. Ciuparu and L. D. Pfefferle, *The Journal of Physical Chemistry C*, 2012, **116**, 8587-8593.

16. G. Lapisardi, L. Urfels, P. Gélin, M. Primet, a. Kaddouri, E. Garbowski, S. Toppi and E. Tena, *Catal. Today*, 2006, **117**, 564-568.

17. X. Wang, Z. Jiang, B. Zheng, Z. Xie and L. Zheng, *Crystengcomm*, 2012, **14**, 7579-7579.

18. K. Zhou, X. Wang, X. Sun, Q. Peng and Y. Li, *Journal of Catalysis*, 2005, **229**, 206-212.

19. C. Pan, D. Zhang and L. Shi, *Journal of Solid State Chemistry*, 2008, **181**, 1298-1306.

20. H. Knözinger and K. Kochloefl, in *Ullmann's Encyclopedia of Industrial Chemistry*, Wiley-VCH Verlag GmbH & Co. KGaA, 2000, DOI: 10.1002/14356007.a05_313.

21. H. Lauron-Pernot, *Catal. Rev.-Sci. Eng.*, 2006, **48**, 315-361.

22. A. Boddien and H. Junge, *Nat Nano*, 2011, **6**, 265-266.

23. K. Tedsree, T. Li, S. Jones, C. W. A. Chan, K. M. K. Yu, P. A. J. Bagot, E. A. Marquis, G. D. W. Smith and S. C. E. Tsang, *Nat Nano*, 2011, **6**, 302-307.

24. K. Bennaceur, B. Clark, F. M. Orr, T. S. Ramakrishnan, C. Roulet and E. Stout, *Oilfield Review*, 2005, 30-41.

25. S. Enthaler, J. von Langermann and T. Schmidt, *Energy & Environmental Science*, 2010, **3**, 1207-1217.

26. B. Sakintuna, F. Lamaridarkrim and M. Hirscher, *Int. J. Hydrog. Energy*, 2007, **32**, 1121-1140.

27. A. Züttel, *Materials Today*, 2003, **6**, 24-33.

28. S. Enthaler, *Chemsuschem*, 2008, **1**, 801-804.

29. X. Zhou, Y. Huang, W. Xing, C. Liu, J. Liao and T. Lu, *Chemical Communications*, 2008, DOI: 10.1039/b803661f, 3540-3542.

30. S. Zhang, O. Metin, D. Su and S. Sun, *Angew. Chem.-Int. Edit.*, 2013, **52**, 3681-3684.

31. A. Gazsi, T. Bansagi and F. Solymosi, *The Journal of Physical Chemistry C*, **115**, 15459-15466.

32. S. A. Halawy, S. S. Al-Shihry and M. A. Mohamed, *Catalysis Letters*, 1997, **48**, 247-251.

33. J. M. Trillo, J. M. Criado and G. Munuera, *Catalysis Reviews*, 1972, **7**, 51-&.

34. M. Ojeda and E. Iglesia, *Angew. Chem.-Int. Edit.*, 2009, **48**, 4800-4803.

35. K. Tedsree, A. T. S. Kong and S. C. Tsang, *Angew. Chem.-Int. Edit.*, 2009, **48**, 1443-1446.

36. G. Samjeske, A. Miki, S. Ye and M. Osawa, *J. Phys. Chem. B*, 2006, **110**, 16559-16566.

37. P. Trens, R. Durand, B. Coq, C. Coutanceau, S. Rousseau and C. Lamy, *Applied Catalysis B: Environmental*, 2009, **92**, 280-284.

38. P. Forzatti and L. Lietti, *Catal. Today*, 1999, **52**, 165-181.

39. E. Aneggi, D. Wiater, C. de Leitenburg, J. Llorca and A. Trovarelli, *ACS Catal.*, 2014, **4**, 172-181.

40. E. Aneggi, C. de Leitenburg and A. Trovarelli, *Catal. Today*, 2012, **181**, 108-115.

41. D. Terribile, J. Llorca, M. Boaro, C. Leitenburg, G. Dolcetti and A. Trovarelli, *Chemical Communications*, 1998, 1897-1898.

42. A. Trovarelli, C. de Leitenburg, M. Boaro and G. Dolcetti, *Catal. Today*, 1999, **50**, 353-367.

6 Ceria Surface Studies

Contents

6.1 Introduction

In Chapter 5, the methane combustion and gas-phase formic acid decomposition catalyst test reactions both demonstrated that the Pd catalyst with the ceria cubes support had superior catalytic activity, indicated by their higher TOF, than the rods support. This was hypothesised to be due to the better oxygen mobility of the cubes support to clean the poison species off the Pd nanoparticles compared to the rods. These variations in catalyst performance were attributed to the different ceria surfaces exposed by the cubes and the rods support. Previous studies also concluded that the differences observed in their catalysts results were associated with these different ceria surfaces[1-8]. In chapter 4, it was revealed that the cubes predominantly expose the (100) whilst the rods predominantly expose the (110) surface shown in Figure 6.1 a and b, respectively.

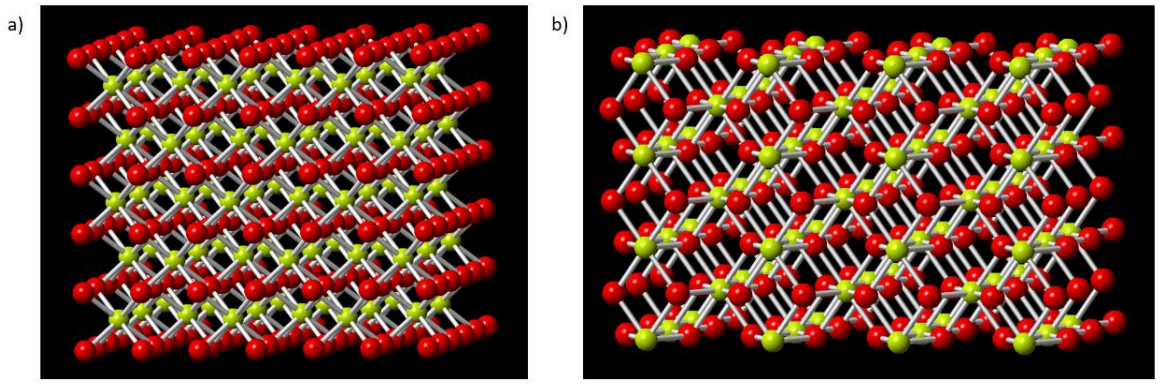

Figure 6.1 Structures of ceria surfaces a) (100) b) (110).

Hence, it is important to investigate the ceria surfaces in order to gain a better understanding in their surface characteristics. Since the increase in popularity of ceria as catalysts in the past decade, their surface chemistry has been studied extensively[9-13]. Computational studies usually investigated the stability of the surfaces[10, 12-14] whilst experimental studies involved using thin film of single crystal ceria to model these low-index ceria surfaces[11, 15-18]. However, in this

study, it was determined to study the ceria surfaces in their working catalyst state, which was in the form of nanoparticles.

Most of the ceria surface characteristics are influenced by their surface oxygen, hence giving the ceria properties such as oxygen mobility and reducibility of surface oxygen for oxygen vacancy formation. Therefore, in order to earn more in-depth knowledge of the ceria properties, it is essential to investigate the characteristics of the surface oxygen in the different ceria surfaces.

6.2 Electronic Paramagnetic Resonance (EPR)

Figure 6.2 shows the EPR profiles of the ceria cubes and rods supports. Both ceria morphologies gave significant EPR signals which corresponded to the g-value of 1.96. Compared to the g-value of a free electron which is 2.00[19, 20], their g-value suggested the presence of trapped electrons, which could arise from oxygen vacancies[21, 22]. Upon formation of an oxygen vacancy, the O_2^- superoxide radical is given off as O_2, leaving a trapped electron in the oxygen vacancy, V_o, which subsequently can reduce Ce^{4+} to Ce^{3+} (Equation 5.1)[23]. It had also been argued that the signal might be resulted from paramagenetic Ce^{3+}, however due to strong spin-orbit coupling and short relaxation times of the $4f^1$ states, it could only be observed at temperatures lower than 20 K[20-22].

$$Ce^{4+} - O_2^- \rightarrow Ce^{3+} - V_o + O_2 \qquad \text{Equation 5.1}$$

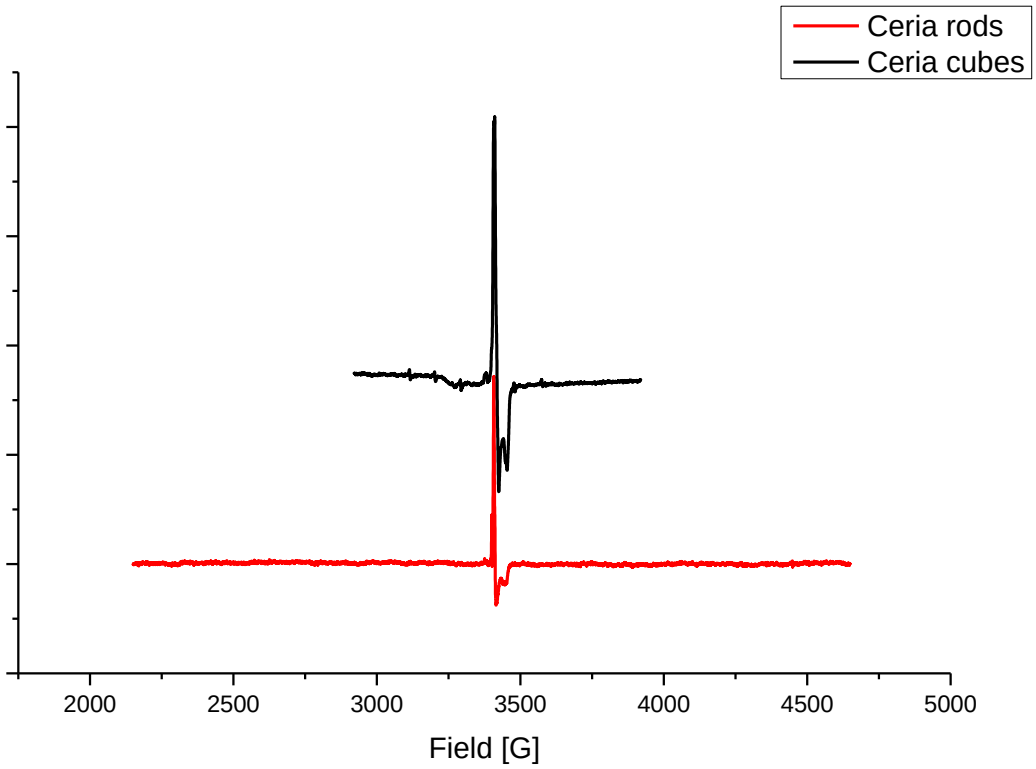

Figure 6.2 EPR spectra of ceria cubes (black) and rods (red).

This EPR result agreed with previous studies that claimed ceria easily releases oxygen to give oxygen vacancies, hence it has been used as an oxygen storage material[24-27]. Sayle *et. al.* also pointed out that from their theoretical calculations, oxygen vacancy formation was surface specific and more favourable on higher energy ceria surfaces, such as (110) and (100) which the ceria rods and cubes incorporated[12].

6.3 Temperature Programmed Reduction (TPR)

The thermodynamics of the oxygen vacancy formation of the ceria cubes and rods could be studied by performing TPR studies. Figure 6.3 shows the TPR profiles of ceria morphologies support and also compared with the 1% Pd deposited samples. Both undeposited ceria

morphologies showed similar TPR profiles, with 2 distinctive peaks at 450 °C and 800 °C which corresponded to the reduction of surface oxygen and bulk oxygen, respectively[28, 29]. The lower temperature of oxygen surface reduction suggested that it was easily reducible compared to the bulk oxygen. It agreed with computational calculations which suggested that the oxygen vacancy formation energy on ceria surface is approximately 30% lower than its bulk[30, 31]. The larger peak area of the surface oxygen for ceria rods when compared to the ceria cubes could be attributed to higher surface area of the former, as shown in Chapter 4.

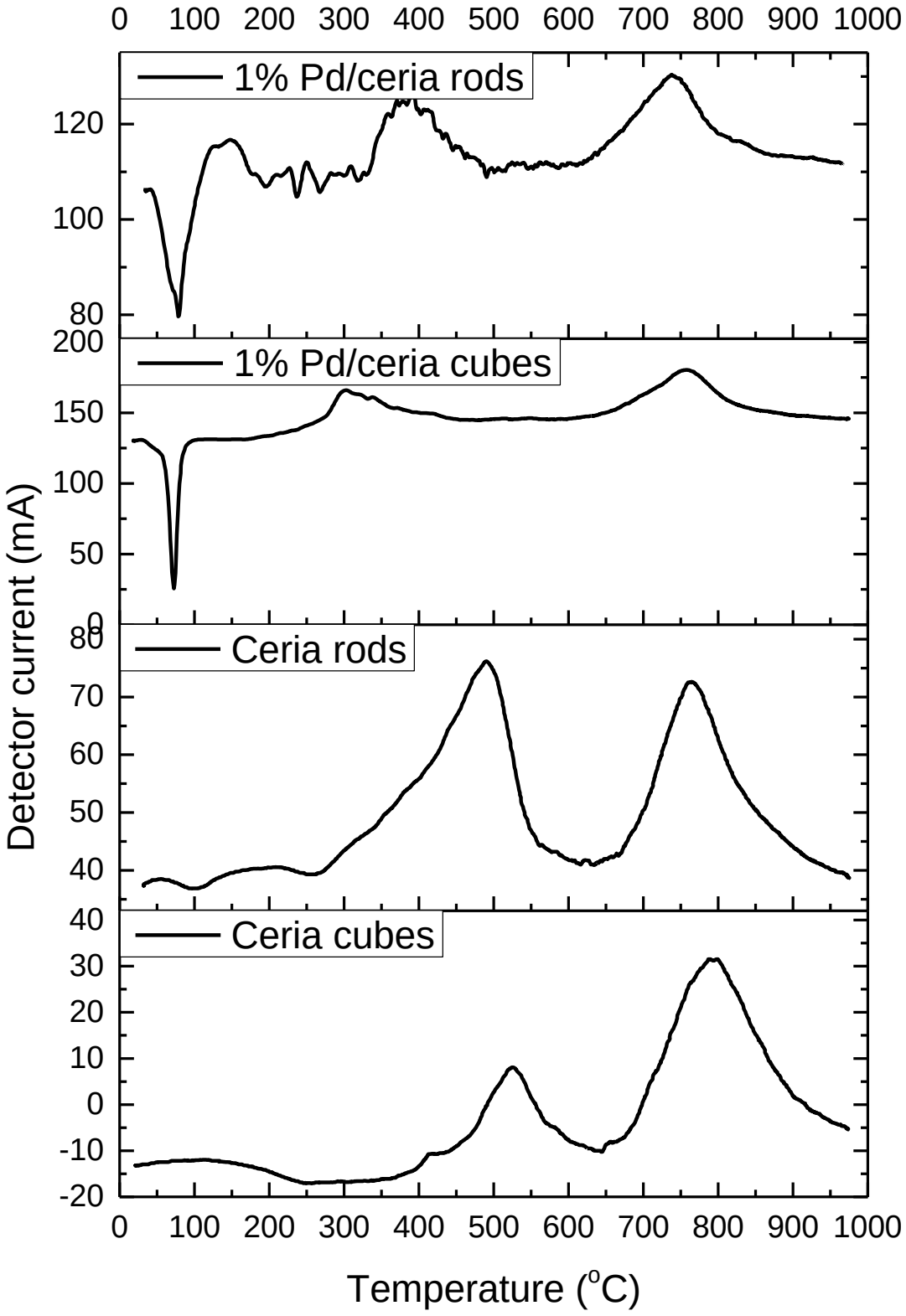

Figure 6.3 TPR profiles of 1% Pd/ceria cubes, 1% Pd/ceria rods, ceria cubes, ceria rods.

However, when 1% Pd was deposited onto the ceria cubes and rods, the bulk oxygen reduction peaks remained at 800 °C whilst the surface oxygen reduction peaks were shifted to lower temperatures. This was an indication that Pd internally catalysed the reduction of surface oxygen. Hence, Pd acted as a promoting agent to enhance the oxygen vacancy formation on the surface of the ceria supports by lowering their surface oxygen reduction activation energy[32]. This observation supported the study made by Vayssilov et. al. where according to DFT calculations, deposition of Pt nanoparticles activated the oxygen on the ceria support, which they referred to as reverse oxygen spillover[33].

In addition, the surface oxygen reduction temperature indicated to be about 100 °C lower on the 1% Pd/ceria cubes than that of the 1% Pd/ceria rods, where their reduction peaks were at 302 °C and 391 °C respectively. This suggested that the reverse oxygen spillover between Pd and ceria was structure sensitive where it was more pronounced on the (100) surface of the ceria cubes than the (110) on the rods. It also indicated that thermodynamically, the oxygen vacancy formation was more favourable on the (100) than the (110) when Pd was deposited, as it has lower activation energy on the 1% Pd/cubes.

Both TPR profiles of 1% Pd/ceria morphologies also showed negative peaks at −80 °C which were attributed to the β-hydride phase, a well-known characteristic of Pd^0 [34]. The β-hydride phase is due to hydrogen interstitial atoms stored in the Pd octahedral holes. Under reducing conditions, these hydrogen interstitial atoms were given off at 80 °C, hence resulting in the negative peak.

Upon integrating the peaks of the TPR profiles to obtain the areas under the peaks, the number of oxygen atoms reduced from the ceria samples can be calculated, hence their reducibility can

be derived (Figure 6.4). The total oxygen reduced from the undeposited ceria cubes and rods samples corresponded to 20% reduction of ceria from CeO_2 to Ce_2O_3 at 1000°C, with most of the oxygen reduced from the bulk of the samples, suggested by the peaks at 800 °C. Compared to the Pd deposited samples, reduction of 38% were achieved for 1% Pd/ceria rods and 28% for the 1% Pd/ceria cubes, with most of reduction occurred at the lower temperatures (surface oxygen). Hence, other than lowering the reducing temperature of the surface oxygen of the ceria, the Pd also acted as a gateway for the oxygen in deeper layers of ceria to be reduced more favourably. The higher reduction percentage of the 1% Pd/ceria rods compared to 1% Pd/ceria cubes might be due to the high surface area of the former.

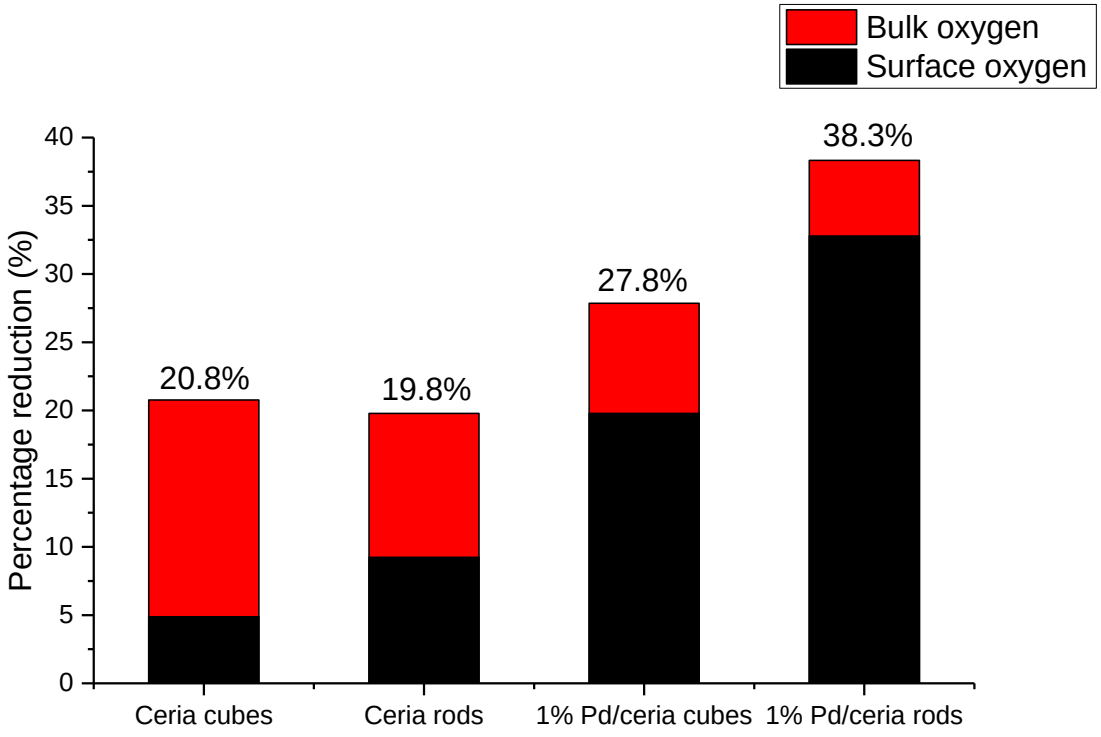

Figure 6.4 Percentage reduction of ceria from CeO_2 to Ce_2O_3, derived from the integrated peak areas of the TPR profiles in Figure 6.3.

6.4 Scanning Transmission Electron Microscopy – Electron Energy Loss Spectroscopy (STEM-EELS)

STEM coupled with EELS was used to investigate the positional Ce^{4+}/Ce^{3+} composition of the ceria sample[35-37]. It also provided the location of the deposited Pd nanoparticles. As ceria oxygen reduction to produce oxygen vacancies is accompanied by the reduction of Ce^{4+} to Ce^{3+}, the presence of Ce^{3+} is an indicator of oxygen vacancy formation. Therefore, the positional Ce^{4+}/Ce^{3+} composition would provide useful information about the formation of the oxygen vacancies between the (100) surface in ceria cubes and the (110) of the rods.

Figure 6.5a shows the high-angle annular dark field image (HAADF) of the 1% Pd/ceria cubes which was obtained by STEM and Figure 6.5b shows the corresponding EELS map where the HAADF image was divided into pixels, where each pixels was an individual EELS spectrum. One example of an EELS spectrum from one of the pixels is shown in Figure 6.6. The EELS spectrum (blue) was subtracted with the background (red) to obtain the background corrected EELS spectrum of the sample (green), where the peaks from different elements could be revealed. The different regions of energy dispersion correlates to the different elements present in the sample. The EELS spectrum also provided the Ce^{4+}/Ce^{3+} composition which could be calculated from the Ce M4/M5 peaks.

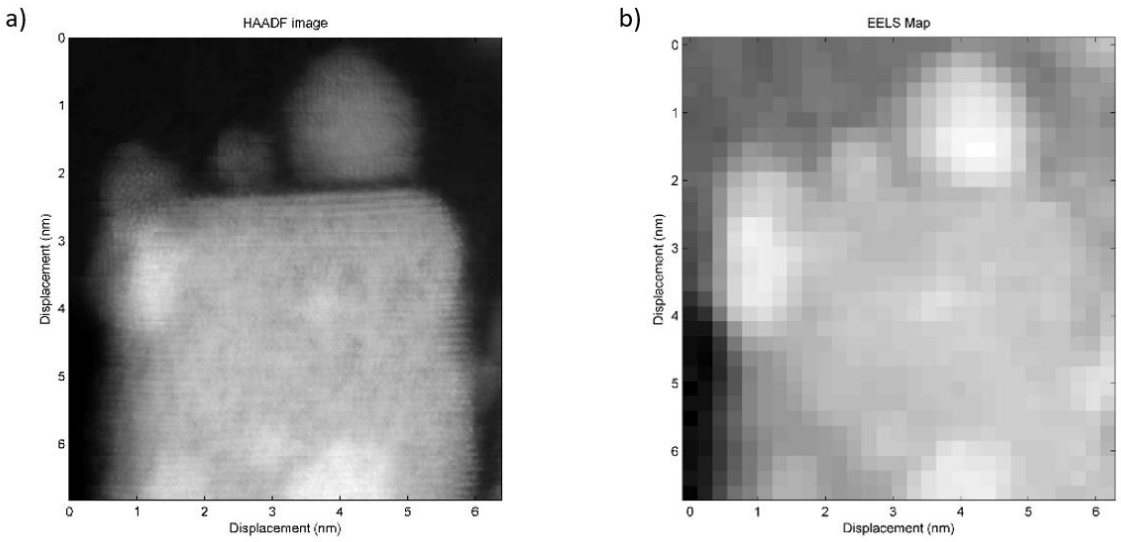

Figure 6.5 a)STEM HAADF image of 1% Pd/ceria cubes and b) its corresponding EELS map.

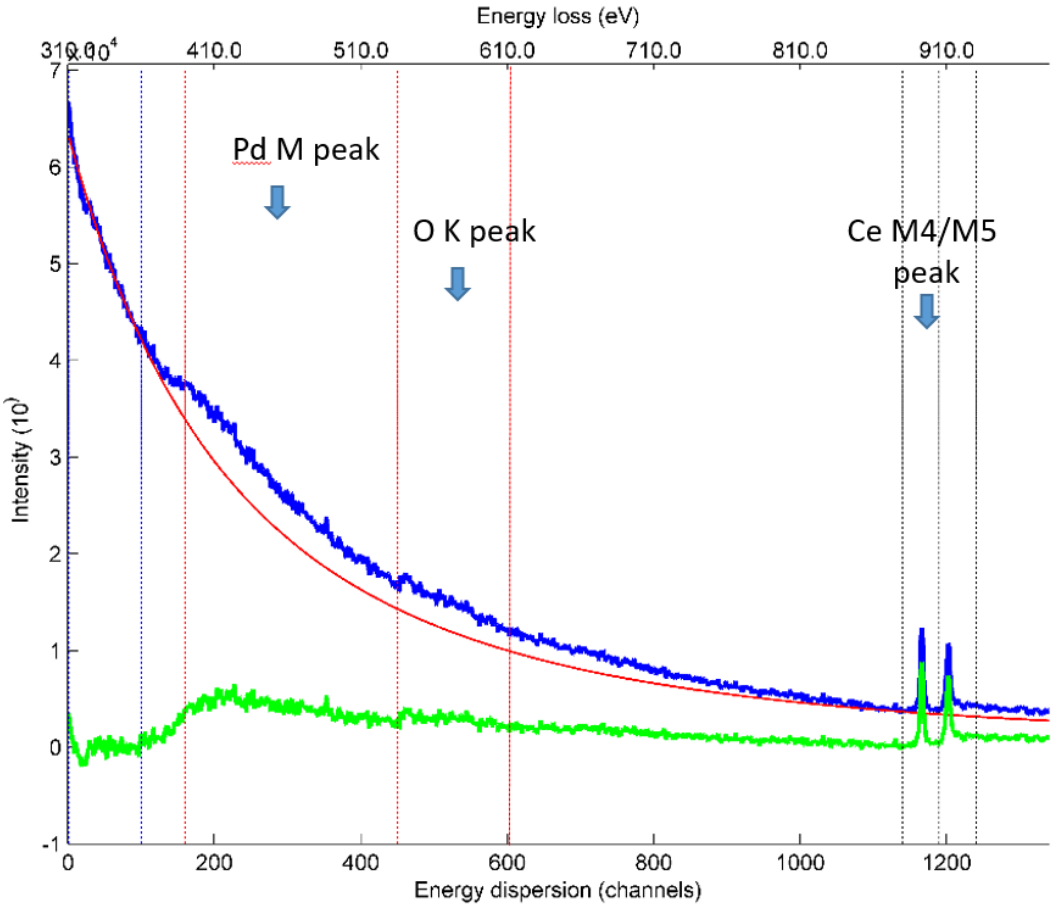

Figure 6.6 EELS spectrum of 1% Pd/ceria cubes.

The TPR study demonstrated that with Pd nanoparticles deposited on the ceria morphologies, the surface oxygen was reduced at 200 – 400 °C for the 1% Pd/ceria cubes and 300 – 500 °C for the 1% Pd/ceria rods (Figure 6.3). Hence, the 1% Pd/ceria morphologies were pre-reduced at 500 °C with H_2 gas for 1 hour before their STEM-EELS measurements were taken. According to the TPR, at 500 °C reduction, it was expected that the surface oxygen of the ceria would be reduced whilst their bulk oxygen remained unreduced, as reduction of ceria bulk oxygen was initiated at 700 °C.

Figure 6.7 and 6.8 showed the EELS mapping of the pre-reduced 1% Pd/ceria cubes and rods respectively. The ceria Ce^{4+}/Ce^{3+} composition mapping (Figure 6.7a and 6.8a) was represented by the greyscale of Ce^{4+} proportion, where white indicated 100% Ce^{4+} whilst black exhibited 100% Ce^{3+} and cyan represented areas where Ce was not present. The Pd composition greyscale (Figure 6.7b and 6.8b) on the other hand was displayed by white where Pd was present and black where Pd was absent.

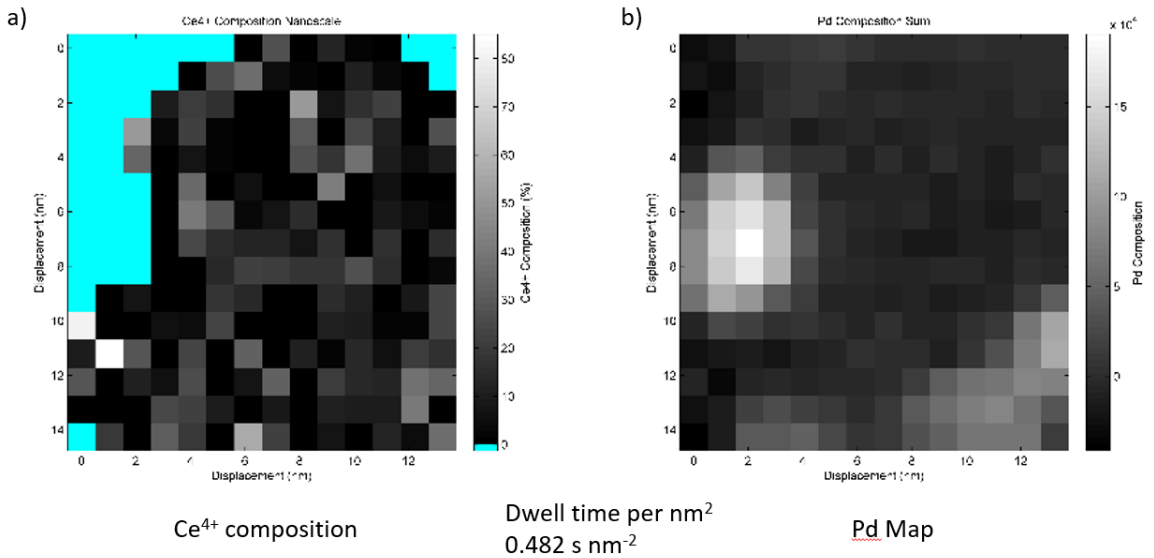

Figure 6.7 Compositional mapping of 1% Pd/ceria cubes reduced at 500 °C in H_2 for 1 hour a) Ce^{4+}/Ce^{3+} b) Pd EELS mapping.

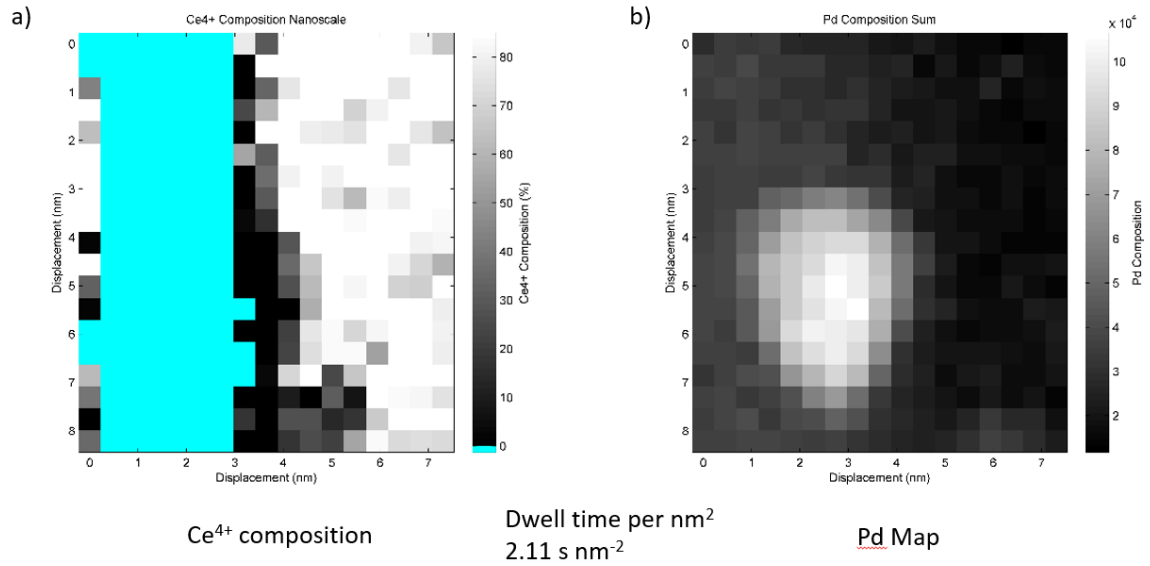

Figure 6.8 Compositional mapping of 1% Pd/ceria rods reduced at 500 °C in H_2 for 1 hour a) Ce^{4+}/Ce^{3+} b) Pd EELS mapping.

After pre-reduction at 500 °C in H_2 for 1 hour, the ceria cubes support indicated to be completely reduced, where not just the expected surface oxygen reduction occurred, but the bulk oxygen was also reduced (Figure 6.7a). However, the reduction only took place on the surface oxygen of the ceria rods as expected from the TPR study, indicated by the black area on the surface of the rods and white areas in the bulk (Figure 6.8a). It also suggested that Pd enhanced the reduction as the depth of reduction was increased at the ceria rods surface adjacent to the Pd nanoparticle.

The pre-reduced EELS mapping of the 1% Pd/ceria cubes was also compared with that of the unreduced sample (Figure 6.9a). The unreduced sample appeared to be reduced on the surface but most of the bulk oxygen remained unreduced. Due to the lack of reduction pre-treatment on the unreduced sample, the surface reduction might be caused by the electron beam of the STEM.

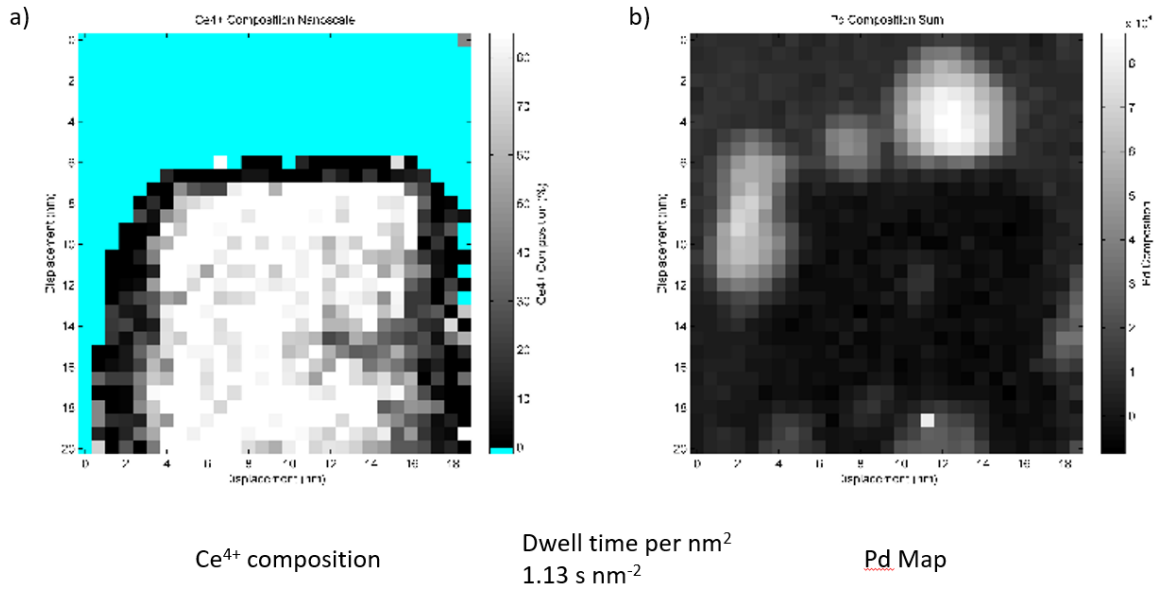

Figure 6.9 Compositional mapping of unreduced 1% Pd/ceria cubes a) Ce^{4+}/Ce^{3+} b) Pd EELS mapping.

To investigate the bulk reduction of 1% Pd/ceria cubes further, the sample was pre-reduced at 200 °C for 1 hour, the temperature where the initial surface reduction occurred according to the TPR study. Similar to the sample pre-reduced at 500 °C, the EELS mapping indicated that both the ceria surface oxygen and bulk oxygen was reduced (Figure 6.10a). This gave an indication that other than the low activation energy of the surface oxygen reduction on the (100) surface of the cubes, it also allowed access to reduce the bulk oxygen through the (100) surface, which implied fast oxygen mobility through this surface. As the pre-reduction was performed at 200 °C, this suggested that the bulk reduction process was kinetically driven.

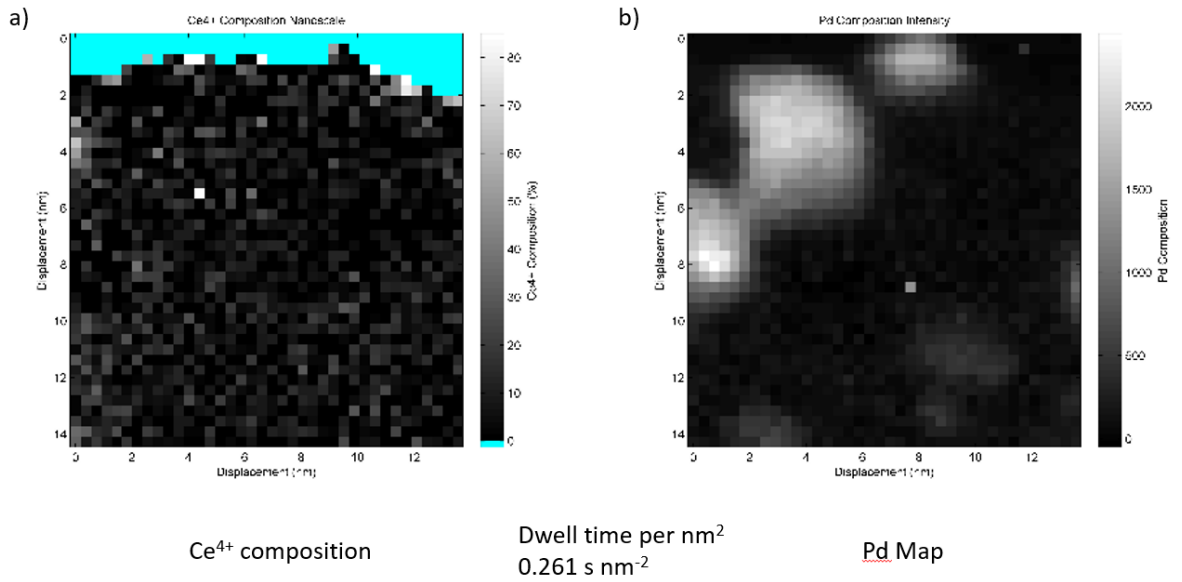

Figure 6.10 Compositional mapping of 1% Pd/ceria cubes reduced at 200 °C in H_2 for 1 hour a) Ce^{4+}/Ce^{3+} b) Pd EELS mapping.

As a control experiment, the undeposited ceria cubes were also tested, with samples pre-reduced at 500 °C (Figure 6.11a) and without pre-treatment (Figure 6.11b). Both samples showed similar EELS mapping which suggested surface oxygen reduction indicated by the presence of Ce^{3+} whilst most of the bulk oxygen of the cubes remained unreduced. The surface reduction of the pre-reduced ceria cubes sample agreed with the TPR result, where without the Pd deposition, the surface oxygen reduction on the ceria cubes occurred at 500 °C. On the other hand, the sample without pre-reduction treatment also experienced an unexpected surface reduction, which gave an indication that the electron beam could also reduce the sample, as it was also observed on the unreduced 1% Pd/ceria cubes sample (Figure 6.9).

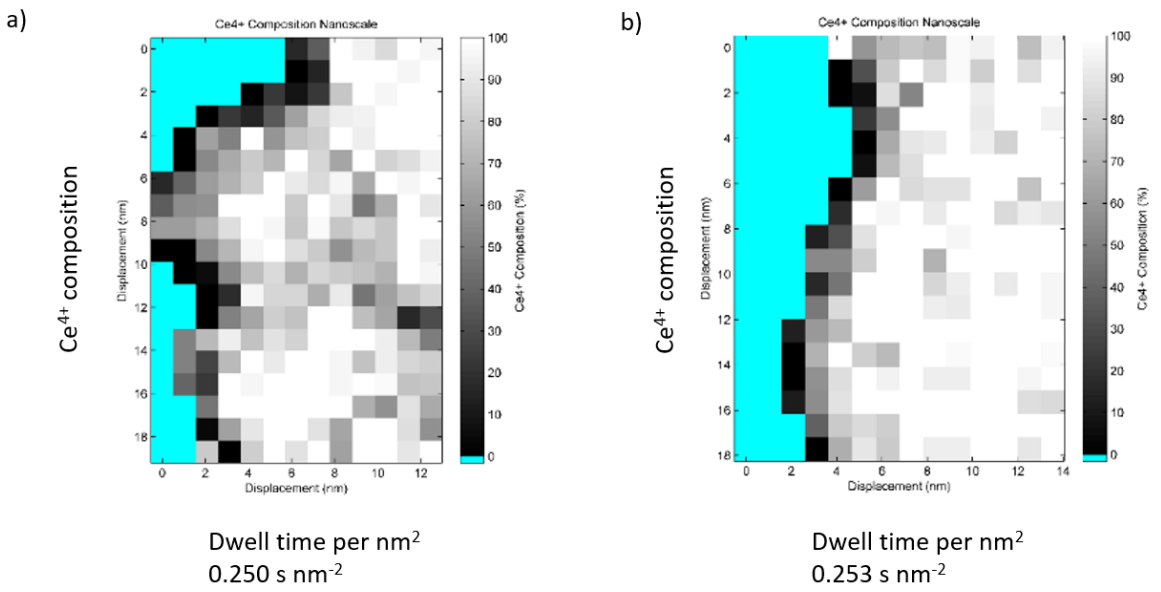

Figure 6.11 Compositional Ce^{4+}/Ce^{3+} EELS mapping of undeposited ceria cubes a) reduced at 500 °C in H_2 for 1 hour b) no pre-treatment

In general, the reduction of bulk oxygen in the ceria cube support was only observed in samples with Pd nanoparticles deposited on them. This suggested that Pd was required to access this bulk oxygen, hence Pd acted as a gateway for the bulk oxygen to be reduced, which is in agreement with the TPR study. However, this bulk oxygen reduction did not apply to the ceria rods.

As the electron beam of STEM had shown to be able to reduce the sample, as observed on the unreduced ceria cubes and 1% Pd/ceria cubes samples (Figure 6.9 and 6.11b), the kinetics of this bulk reduction could be studied by focussing the electron beam on the sample and measuring the EELS mapping consecutively. Figure 6.12 a, b and c showed 3 consecutive EELS mappings of unreduced 1% Pd/ceria cubes. The 1st measurement showed that only the surface of the ceria cubes was reduced, as observed previously, but as more EELS measurements were taken, the reduction of the bulk oxygen became more apparent. With this information, the rates of reduction were calculated and mapped to their corresponding areas.

The rates of reduction were represented by the visible light colours spectrum where red signified the fastest rate of reduction whilst blue signified that no reduction was taking place (Figure 6.12 g and h). The bulk oxygen in the ceria cubes experienced the fastest rate of reduction between the 1st and 2nd scan and the rate decreased between the 2nd and the 3rd scan as most of the bulk oxygen has been reduced.

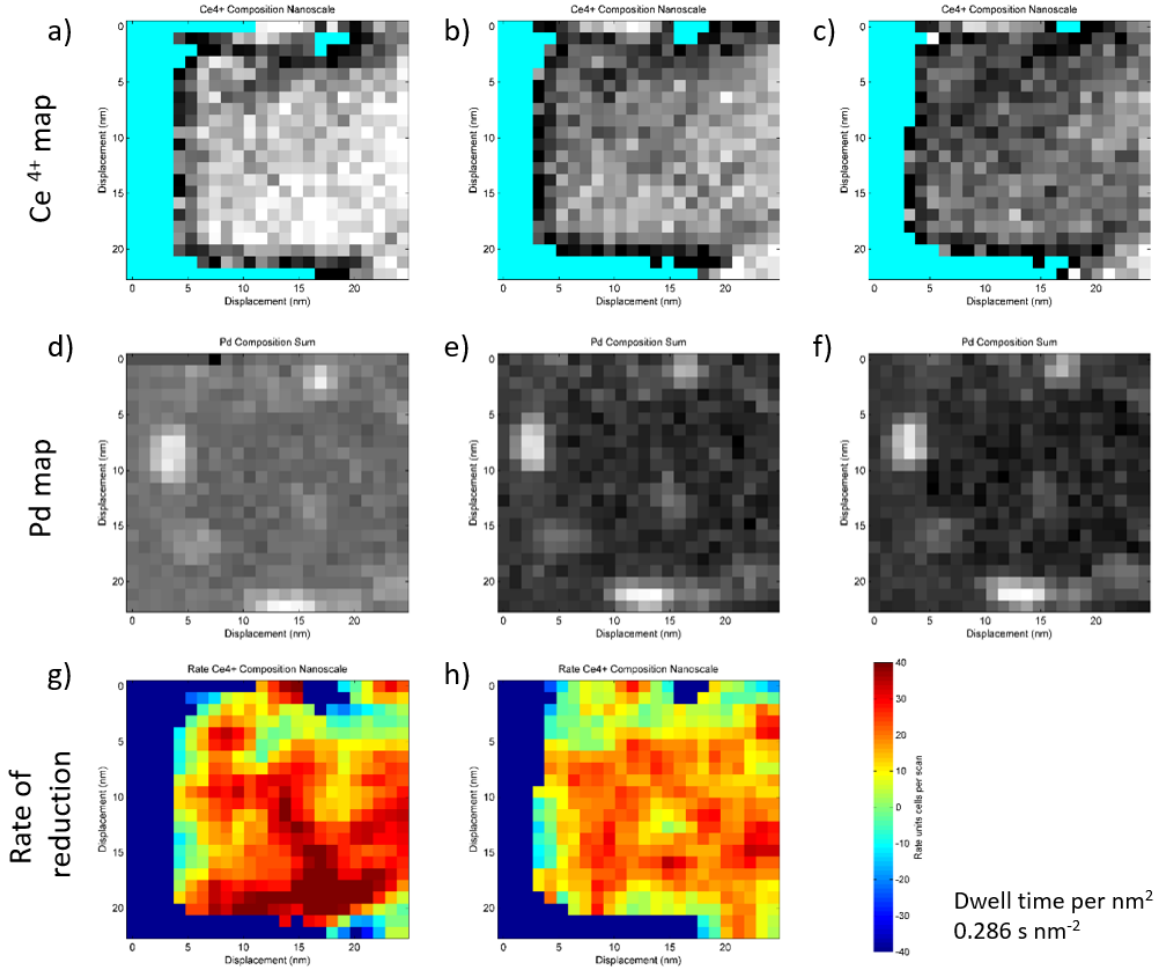

Figure 6.12 Compositional Ce^{4+}/Ce^{3+} EELS mapping of 1% Pd/ceria cubes at a) 1st scan b) 2nd scan c) 3rd scan and their corresponding Pd mapping d), e) and f) respectively. Rate of reduction between g) 1st and 2nd scans and h) 2nd and 3rd scans.

The rate of reduction mapping also suggested that the fastest reduction rates occurred at ceria sites adjacent to Pd nanoparticles deposition. It was especially highlighted in the mapping

between the 1st and 2nd scans. This agreed with the previous observation that Pd acted as a gateway for the reduction of these bulk oxygen.

The rate of reduction of 1% Pd/ceria cubes by the electron beam was also compared with that of undeposited ceria cubes. Similar as before, the 1st scan showed that only the reduction of surface oxygen was reached, whereas the bulk oxygen remained unreduced (Figure 6.13). As the scans proceeded, there was no bulk oxygen reduction observed and the rate of reduction mappings indicated minimal reduction in the ceria bulk, even after 5 scans. Hence, this emphasised further that Pd was needed to reduce the bulk oxygen through the (100) surface of the ceria cubes.

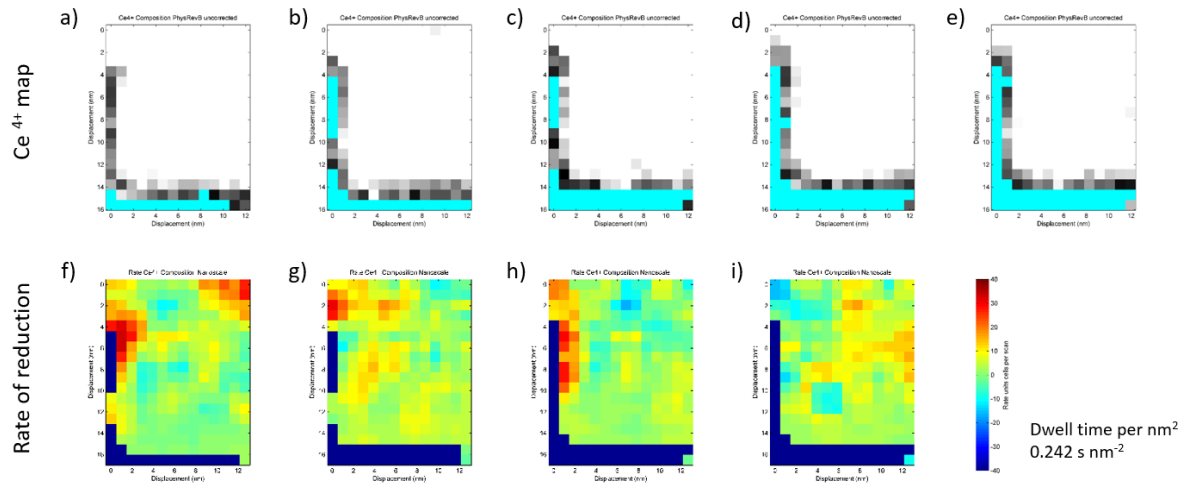

Figure 6.13 Compositional Ce^{4+}/Ce^{3+} EELS mapping for undeposited ceria cubes at a)1st scan, b) 2nd scan, c) 3rd scan, d) 4th scan and e) 5th scan. Rate of reduction between f) 1st and 2nd, g) 2nd and 3rd, h) 3rd and 4th and i) 4th and 5th scans.

Therefore, these STEM-EELS studies demonstrated that Pd was needed to activate the oxygen of the ceria, which agreed with the TPR study. In addition, in the case of the ceria cubes, the Pd could also be used to access the reduction of the bulk oxygen though the (100) surface. Hence, this could provide a postulation on the observations of the catalyst testing results, where

the Pd with cubes support appeared to have a higher oxygen reservoir and faster oxygen mobility, which were used for poison cleaning, than the rods support. Because of the participation of the bulk oxygen in ceria cubes, more of the poison could be cleaned off compared to the ceria rods, where only surface oxygen was available.

6.5 Ambient Pressure X-ray Photoelectron Spectroscopy (AP-XPS)

The Ce^{4+}/Ce^{3+} composition of the ceria surface was also characterised by x-ray photoelectron spectroscopy (XPS)[38-42]. In contrast to STEM-EELS, XPS is purely a surface study technique, limited to a few monolayers depth of the sample. The most commonly used method of determining the oxidation state of Ce is by the measuring the Ce 3d core level. However, most of the XPS studies on ceria were done under ultra-vacuum conditions which might not reflect the sample under catalytic conditions. Hence, using ambient pressure (AP)-XPS developed by Tao et. al., measurements of these catalysts could be performed in *operando*, where reducing or oxidising gases could be fed into the sample[43]. With this technique, the surface Ce^{4+}/Ce^{3+} composition under reaction conditions could be determined. To reflect the TPR study, the catalyst samples were heated in 1 Torr H_2 gas to 500 °C, the temperature suggested by TPR experiment to reduce the surface oxygen for oxygen vacancy formation in Pd deposited ceria morphologies (Figure 6.3). The samples were cooled to 100 °C under H_2 before their XPS measurements were taken. The samples were also reoxidised by heating them in 1 Torr O_2 gas at 300 °C for 3 hours to investigate the oxygen replenishing of the reduced ceria samples.

Figure 6.14 shows the Ce 3d XPS spectra for 1% Pd/ceria cubes and rods and compared with their corresponding undeposited samples, under UHV, reduced and oxidised conditions. Under UHV, all their spectra correspond to the typical Ce 3d spectrum of fully oxidised CeO_2 sample

(Figure 6.15a), which contains six peaks resulting from spin orbit-splitting of 3d core level. Additional peaks were also present which were due to 'shake-down' states where electrons are transferred from the O 2p level to the Ce 4f level in the excited state. On the other hand, the typical spectrum of fully reduced ceria, Ce_2O_3 shown in Figure 6.15c consists of 4 peaks which also resulted from spin-orbit splitting of 3d core level. Under reduced conditions, the spectra of all the samples (Figure 6.14, labelled under H_2 100 °C) resembled that of the partially reduced CeO_{2-x} (Figure 6.15b), where their spectra were the combination of CeO_2 and Ce_2O_3.

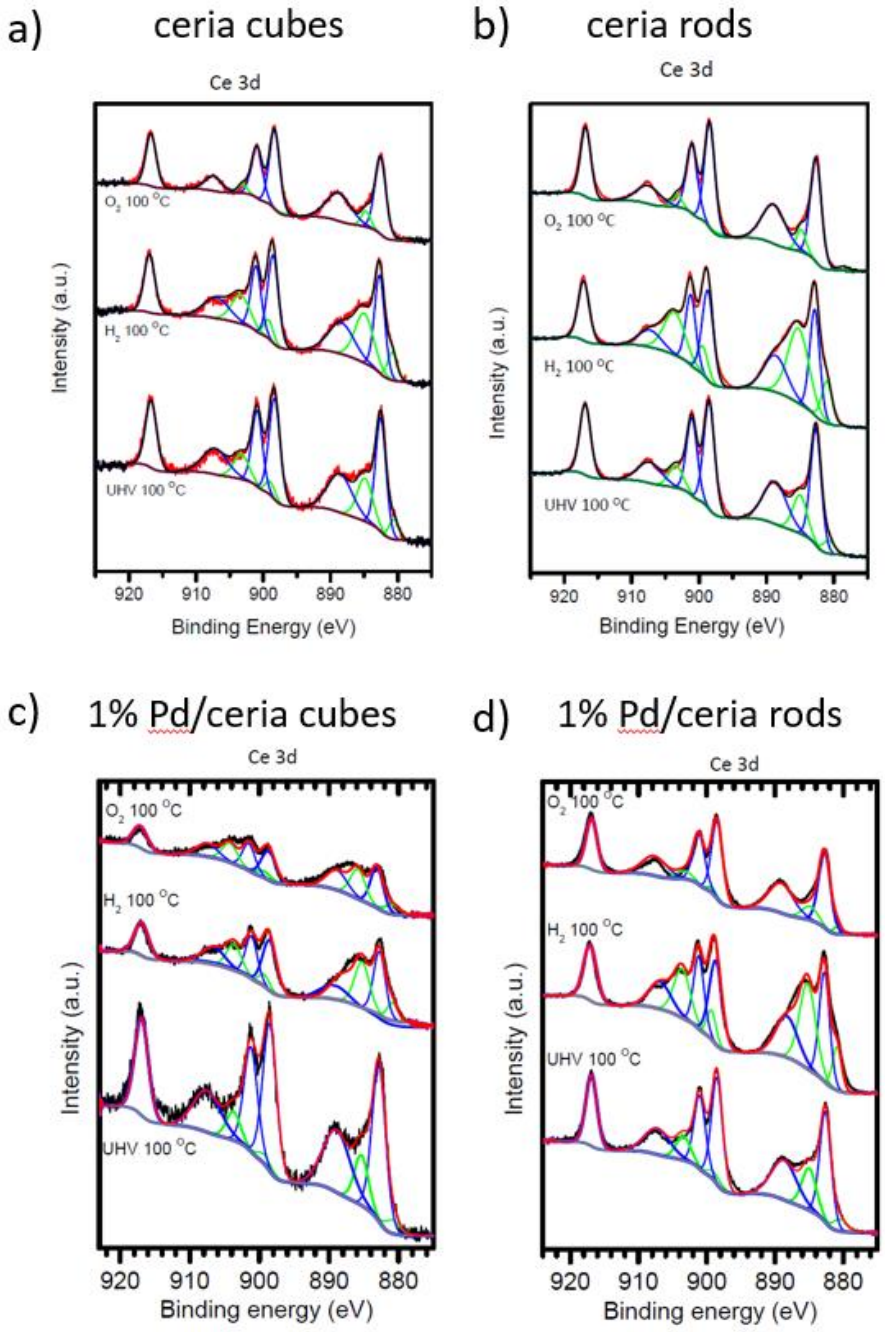

Figure 6.14 XPS Ce 3d spectra of a) ceria cubes b) ceria rods c) 1% Pd/ceria cubes d) 1% Pd/ceria rods under UHV (UHV 100 °C), reduced (H_2 100 °C) and reoxidised (O_2 100 °C) conditions.

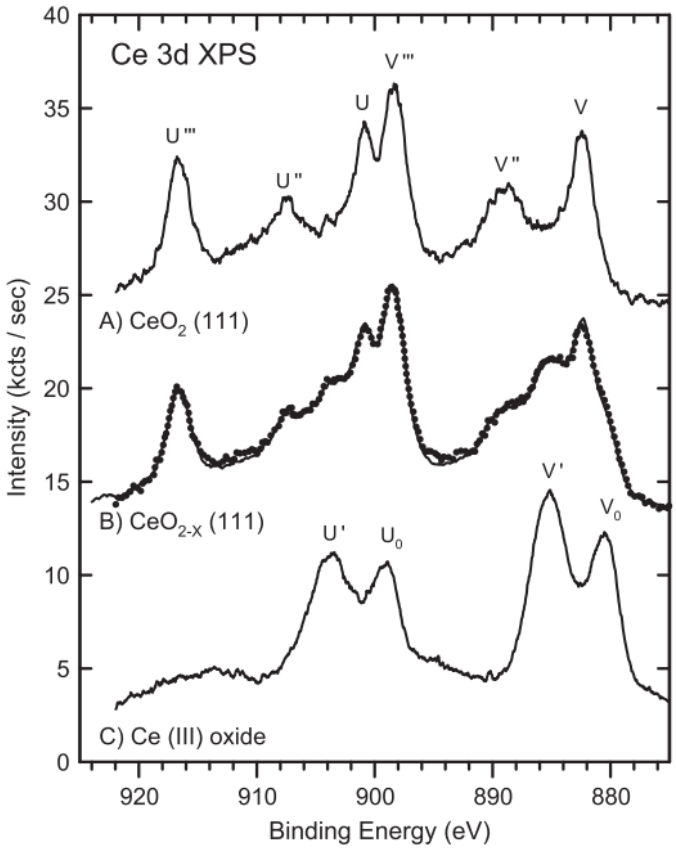

Figure 6.15 Typical XPS Ce 3d spectra of a) fully oxidised ceria, CeO_2 b) partially reduced ceria, CeO_{2-x} and c) fully reduced ceria, Ce_2O_3[38].

The Ce 3d spectra were also used to calculate the Ce^{4+}/Ce^{3+} compositions of the samples under the different conditions (Figure 6.16). Under UHV, small amounts of Ce^{3+} (green) were present in all the samples, which could attributed to the existing oxygen vacancies in ceria, which was also observed in EPR experiments. The oxygen vacancies increased after the samples were reduced to 500 °C in 1 Torr H_2, indicated by the increase in Ce^{3+} and the decrease in Ce^{4+} compositions. This trend was in agreement with the STEM-EELS results, however XPS only showed the reduction of around 30% as opposed to the nearly 100% reduction of ceria surface observed in STEM-EELS. The discrepancy in the degree of reduction might be attributed to the reduction process, where the sample for STEM-EELS was reduced in H_2 at atmospheric pressure whilst the reduction in AP-XPS was performed with 1 Torr H_2. Due to the low H_2 pressure in AP-XPS, the equilibrium of surface oxygen reduction was not as heavily shifted

towards the reduction process as observed in pre-reduction treatment for the STEM-EELS samples.

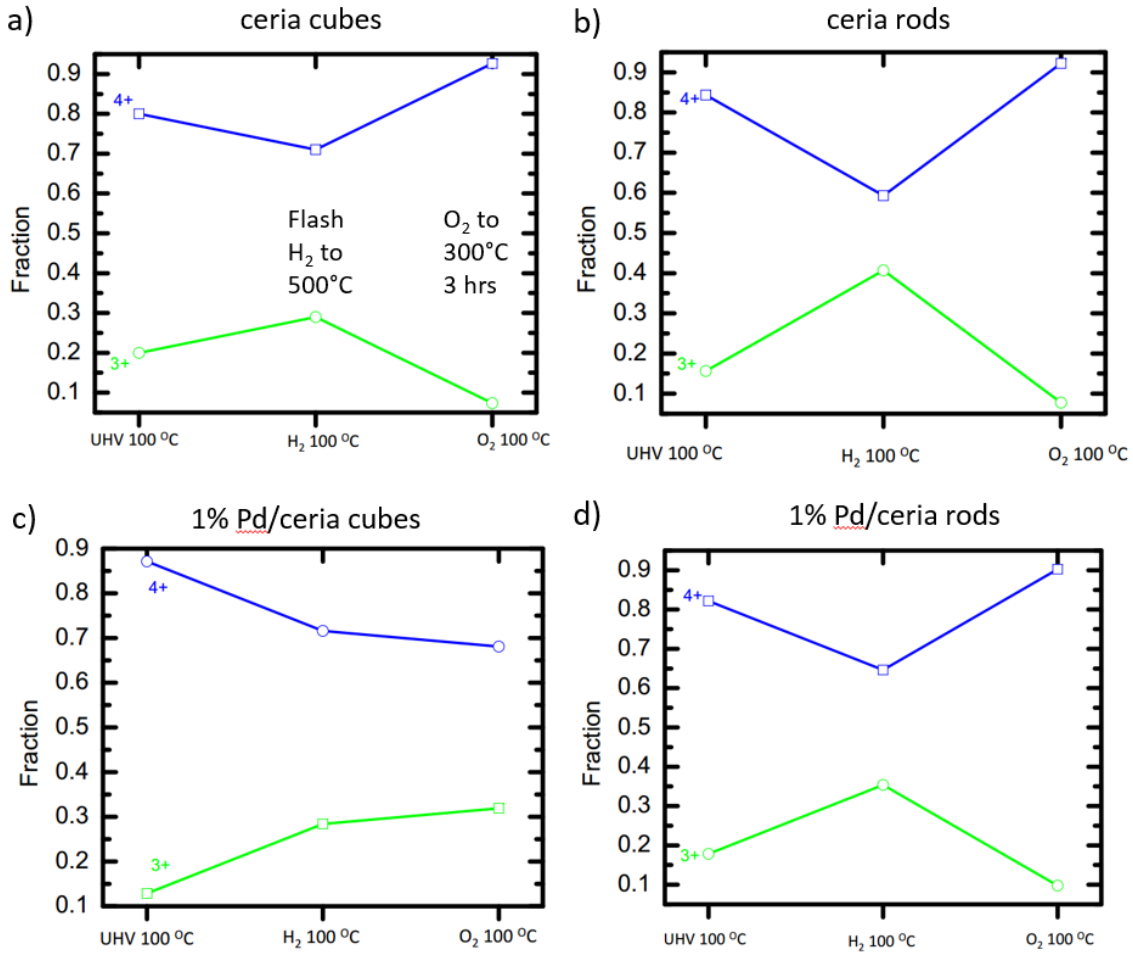

Figure 6.16 Ce^{4+} (blue) / Ce^{3+} (green) compositions calculated from XPS Ce 3d spectra of a) ceria cubes b) ceria rods c) 1% Pd/ceria cubes d) 1% Pd/ceria rods under UHV (UHV 100 °C), reduced (H_2 100 °C) and reoxidised (O_2 100 °C) conditions.

Upon oxidation with 1 Torr O_2 gas at 300 °C for 3 hours, all the samples appeared to be restored to the initial CeO_2 where most of Ce^{3+} were oxidised back to Ce^{4+} (Figure 6.16, labelled under O_2 100 °C), indicating their oxygen vacancies were refilled by O_2 in the oxidation process. With the exception of the 1% Pd/ceria cubes sample where upon oxidation, the surface composition of Ce^{4+}/Ce^{3+} remained unchanged. This might be due to the replenishing of the bulk oxygen during the oxidation process, as the oxygen supplied was used to fill the oxygen

vacancies in the bulk, hence leaving the oxygen vacancies on the surface still unfilled. This also indicates that the bulk reduction was kinetically driven as the reduction still occurred despite the surface oxygen not being completely reduced.

6.6 Pulse Isotopic Exchange (PIE)

Pulse isotopic exchange (PIE) experiments were used to determine the rate of oxygen exchange on the surfaces of the ceria morphologies, with and without deposited Pd[44-46]. The rate of oxygen exchange would provide information about the kinetics of the oxygen mobility of these ceria surfaces. The ceria samples were maintained in equilibrium with 21% $^{16}O_2$/Ar carrier gas mixture and pulses of known volume of 22% $^{18}O_2$/Ne/Ar mixture were injected to the ceria samples, where the ^{16}O in ceria would be exchanged with the ^{18}O. The pulse isotopic oxygen exchange experiments was performed at different temperatures so their activation energies could be obtained. Figure 6.17 shows the relative intensities of the resultant gas of the pulse isotopic exchange for Pd deposited and undeposited ceria cubes and rods samples, at temperatures from 425 – 550 °C. The general trend observed was as the temperature was increased, the $^{18}O_2$ peak decreased and $^{16}O^{18}O$ peak increased indicating faster oxygen exchange rate.

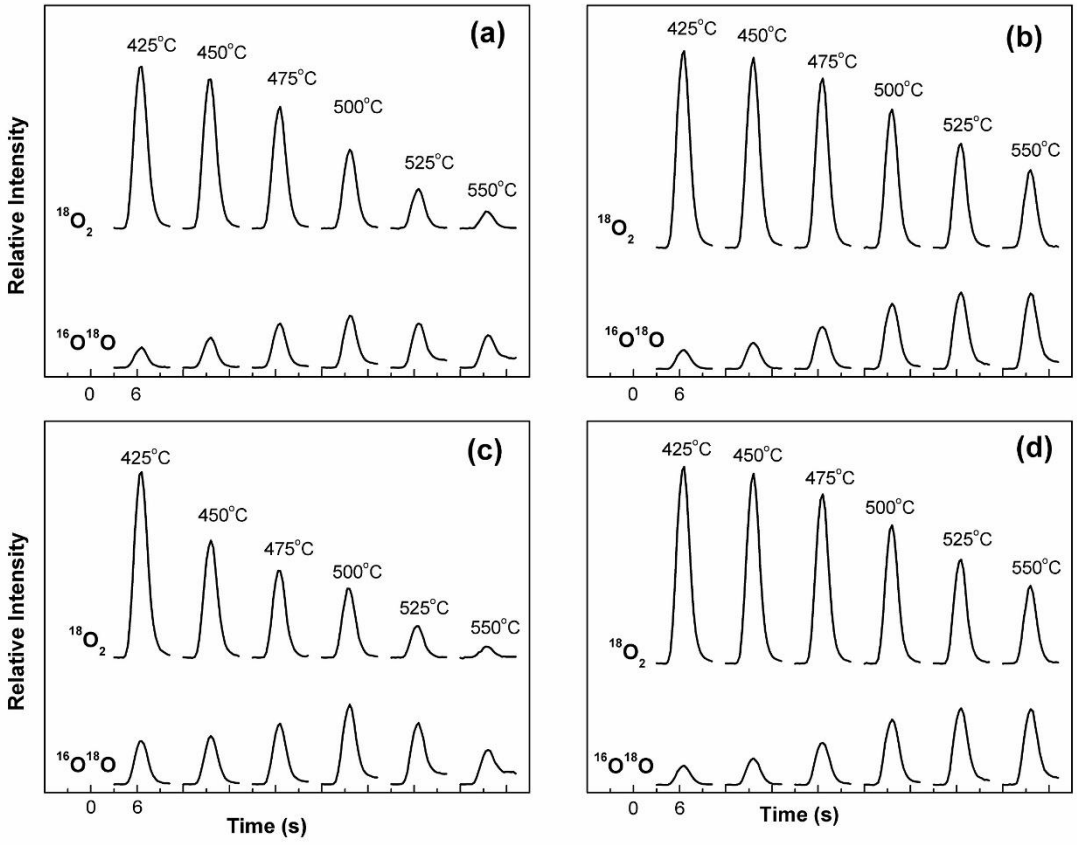

Figure 6.17 Mass spectroscopic peaks of $^{18}O_2$ and $^{16}O^{18}O$ output gases from PIE measurements of a) ceria cubes b) 1% Pd/ceria cubes c) ceria rods d) 1% Pd/ceria rods at different temperatures. All peaks correspond to the time length of 7 seconds.

The $^{18}O_2$ and $^{16}O^{18}O$ peaks were integrated to obtain the peak areas so the mole fractions of $^{18}O_2$ and $^{16}O^{18}O$ in the gas outlet can be calculated, where they were used to derive the surface exchange rate, R_0 (Equation 6.2). The details of the calculations are covered in Chapter 2.

$$R_o = -\frac{2pO_2}{RS_r} \cdot \frac{F}{T} \ln\left(\frac{f_{g,o}^{18}}{f_{g,i}^{18}}\right), \qquad \text{Equation 6.2}$$

where R_o is the surface exchange rate (mol O m^{-1} s), pO_2 is the partial pressure of oxygen, R is the gas constant, S_r is the surface area of the oxide sample, F is the gas flow rate and T is the temperature.

The Arrhenius plot of surface exchange rates at temperatures 425 – 550 °C is shown in Figure 6.18. In general, the cubes samples appeared to have faster surface exchange rates compared to the rods and the undeposited samples had faster rates than their corresponding Pd deposited samples. Furthermore, all the samples had the same gradients suggesting similar activation energy (Table 6.1), hence all the samples underwent similar oxygen exchange mechanism.

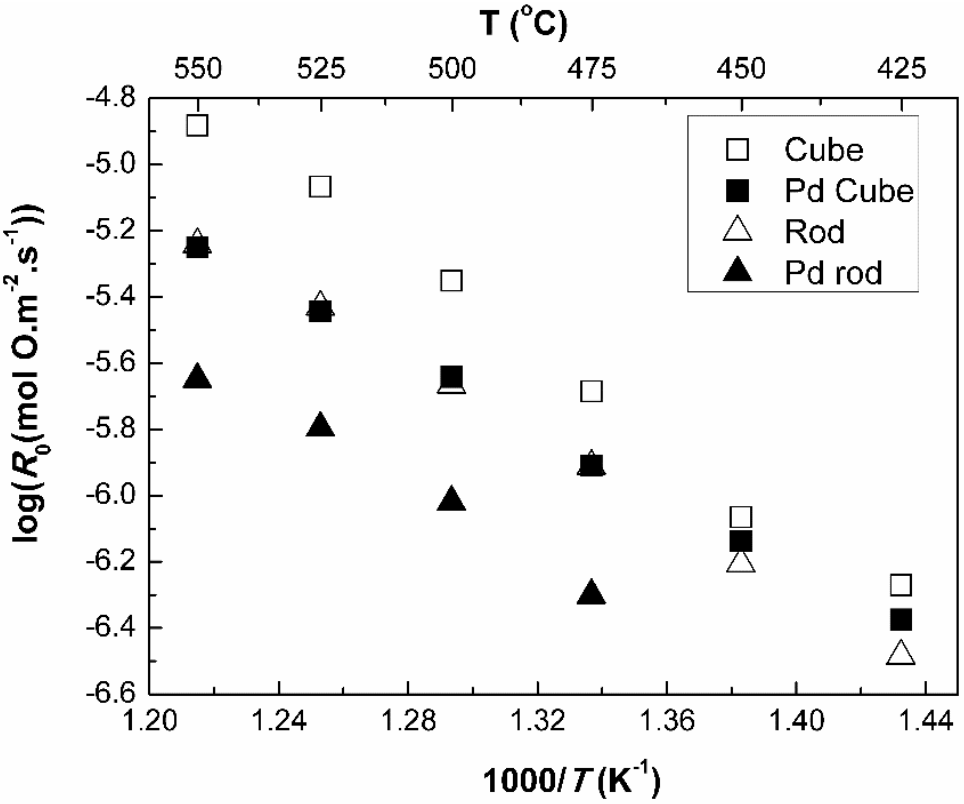

Figure 6.18 Arrhenius plots of rate of oxygen exchange from PIE measurements of ceria cubes and rods and 1% Pd/ceria cubes and rods.

Sample	Activation energy (kJ/mol)	Error (kJ/mol)
Ceria cubes	129	± 6
Ceria rods	111	± 2
1% Pd/ceria cubes	100	± 2
1% Pd/ceria rods	103	± 8

Table 6.1 Activation energies of rate of oxygen exchange calculated from Arrhenius plot Figure 6.18.

By comparing between the undeposited ceria morphologies, the faster oxygen exchange rates observed by the ceria cubes in comparison to the rods suggested that the (100) surface of the cubes had faster oxygen mobility than the (110) surface of the ceria rods. Their similar activation energies also agreed with the TPR measurements where their surface oxygen reduction occurred at similar temperatures.

However, the TPR study showed that deposition of Pd lowered the activation energy of the surface oxygen and STEM-EELS experiments demonstrated that Pd deposition enhanced the rate of oxygen mobility of the ceria surface, which were in disagreement with the observations in PIE experiments. The disagreement might be due to the experimental conditions of the samples, as TPR and STEM-EELS were performed under reducing conditions, the PIE on the other hand was carried out under oxidising conditions. The Pd^0 was known to oxidise to PdO under oxidising conditions at high temperatures, which could attribute to the slower oxygen mobility. To rectify this issue, the experiments were repeated with the samples pre-reduced in 5% H_2/Ar at 350 °C for 30 minutes before the PIE measurements were taken. The downside of this pre-reduction method was that the samples were not in equilibrium with the 20% $^{16}O_2$/Ar carrier gas mixture, hence Equation 6.1 could not be used to calculate the rate of oxygen exchange. However the oxygen exchange rates could be analysed qualitatively by observing

the isotopic oxygen fractions of $^{18}O_2$ and $^{16}O^{18}O$ in the gas outlet. Generally, low fraction of $^{18}O_2$ and high fraction of $^{16}O^{18}O$ indicated fast oxygen exchange rate.

Figure 6.19 shows the isotopic oxygen fractions of the $^{18}O_2$ and $^{16}O^{18}O$ upon PIE with the reduced (black) undeposited and Pd deposited ceria morphologies at different temperatures, compared with their respective unreduced samples (red). The pre-reduction appeared to have insignificant effect on both of the undeposited ceria morphologies, whereas significant changes in the isotopic oxygen fraction profiles were observed for the Pd deposited samples. Hence the previous hypothesis on the deactivation of Pd^0 due to oxidation to PdO might be valid, where the pre-reduction resulted in faster oxygen exchange rates for both Pd deposited ceria morphologies compared to unreduced samples, suggested by the lower $^{18}O_2$ fraction and $^{16}O^{18}O$ fraction upon pre-reduction.

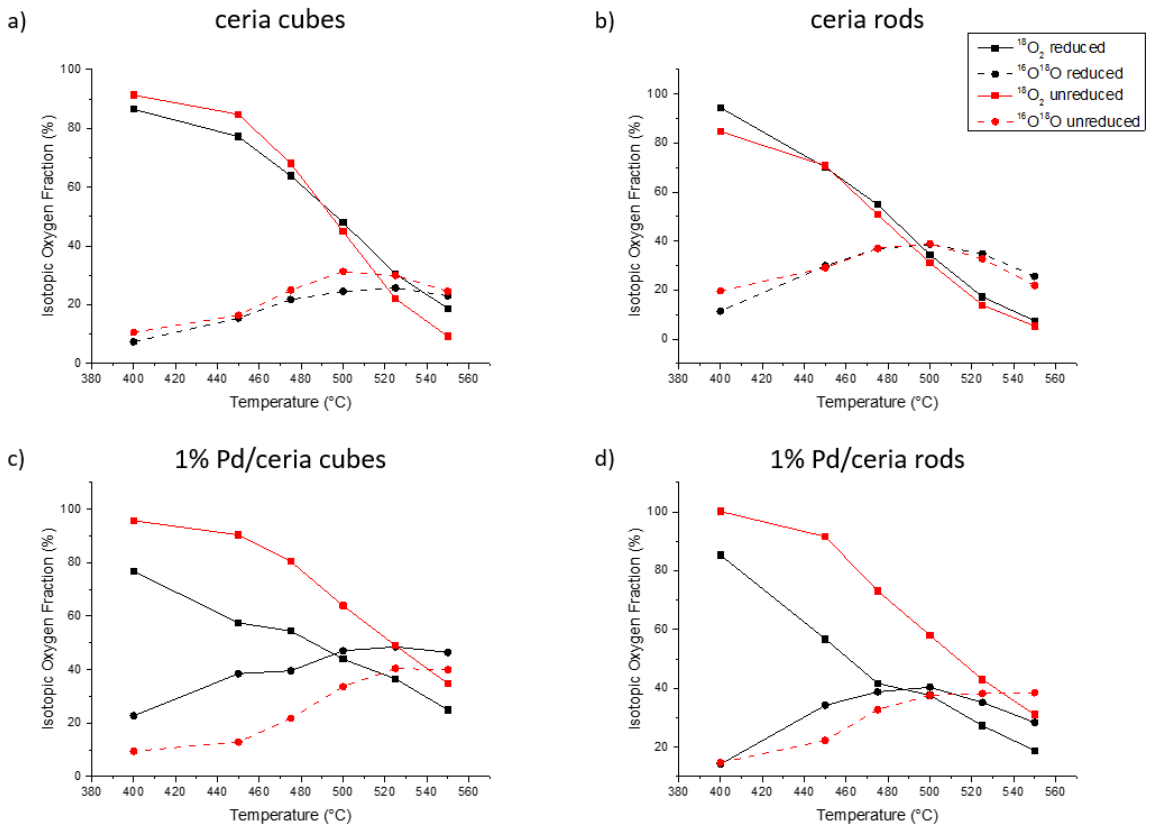

Figure 6.19 Isotopic oxygen fractions of $^{18}O_2$ and $^{16}O^{18}O$ from PIE measurements of a) ceria cubes b) ceria rods c) 1% Pd/ceria cubes d) 1% Pd/ceria rods at different temperatures.

However, the oxidation of Pd^0 to PdO implied that the oxygen gas fed into the system was used for the oxidation process, which meant that the isotopic oxygen fraction of $^{18}O_2$ would not be a suitable indicator of oxygen exchange rate. Hence, the rate of oxygen exchange for the pre-reduced samples between the 1% Pd/ceria cubes and rods were compared by the $^{16}O^{18}O$ isotope oxygen fraction (Figure 6.20), since during the pulse, the only source of ^{16}O was from the samples. The generic trend observed across the different temperatures was the cubes showed to have higher $^{16}O^{18}O$ fraction which suggested faster oxygen exchange rate than the rods. As a result, this study demonstrated that Pd on cubes support had faster oxygen mobility than on the rods support, which were in agreement with previous TPR and STEM-EELS study, as well as the catalyst testing results.

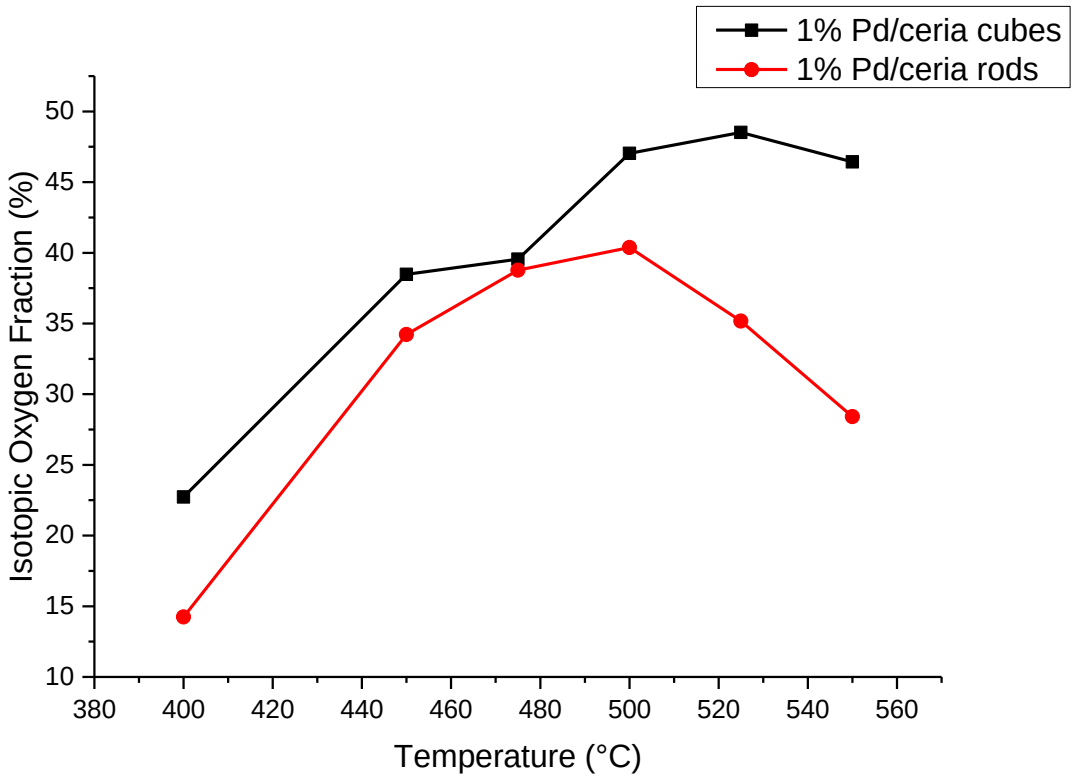

Figure 6.20 Isotopic oxygen fraction of $^{16}O^{18}O$ from PIE measurements of 1% Pd/ceria cubes (black) compared with 1% Pd/ceria rods (red).

The PIE experiments demonstrated that the oxygen mobility was faster on the (100) surface of the ceria cubes than the (110) surface of the ceria rods. This trend was also observed with Pd deposited on the ceria support morphologies, upon pre-reduction of the samples, which indicated Pd^0 was required to activate these surface oxygen as opposed to the oxidised PdO.

6.7 Density Functional Theory (DFT)

Density Functional Theory (DFT) is one of the most used computational calculations to investigate the stability of the ceria surfaces, as their properties such as oxygen vacancy formation and oxygen mobility are dependent on the ceria surface energy. Previous studies have found that the high surface energies of ceria resulted in high reactivity[1, 3, 4, 8, 25]. Most DFT

calculations and other computational modelling studies on ceria surfaces are were in agreement that (111) is the most stable surface with the lowest surface energy[12]. However, the order of surface energies between (110) and (100) have been disputed[10, 13, 14, 47-49]. This disagreement between the stability of (100) and (110) surfaces was due to the limitation of computation studies on the accurate description of reduced CeO_{2-x}.

Figure 6.21 shows the structural models of (111), (110) and (100) ceria surfaces. The (100) surface has been reported by Kim *et. al.* to be terminated by O in their direct recoil spectroscopy / low energy ion scattering of Kr experiments[50]. It also has been argued to produce a net dipole moment perpendicular to the surface due to alternately charged planes with a repeat unit consisting of only two planes which is termed a polar surface[14, 47, 49]. Hence, most computational studies involve eliminating of this net dipole by removing half of the oxygen from the top surface and placing them on the bottom surface (Figure 6.21d)[10, 11, 13, 48]. However, this did not represent the actual surface of the ceria under reaction conditions.

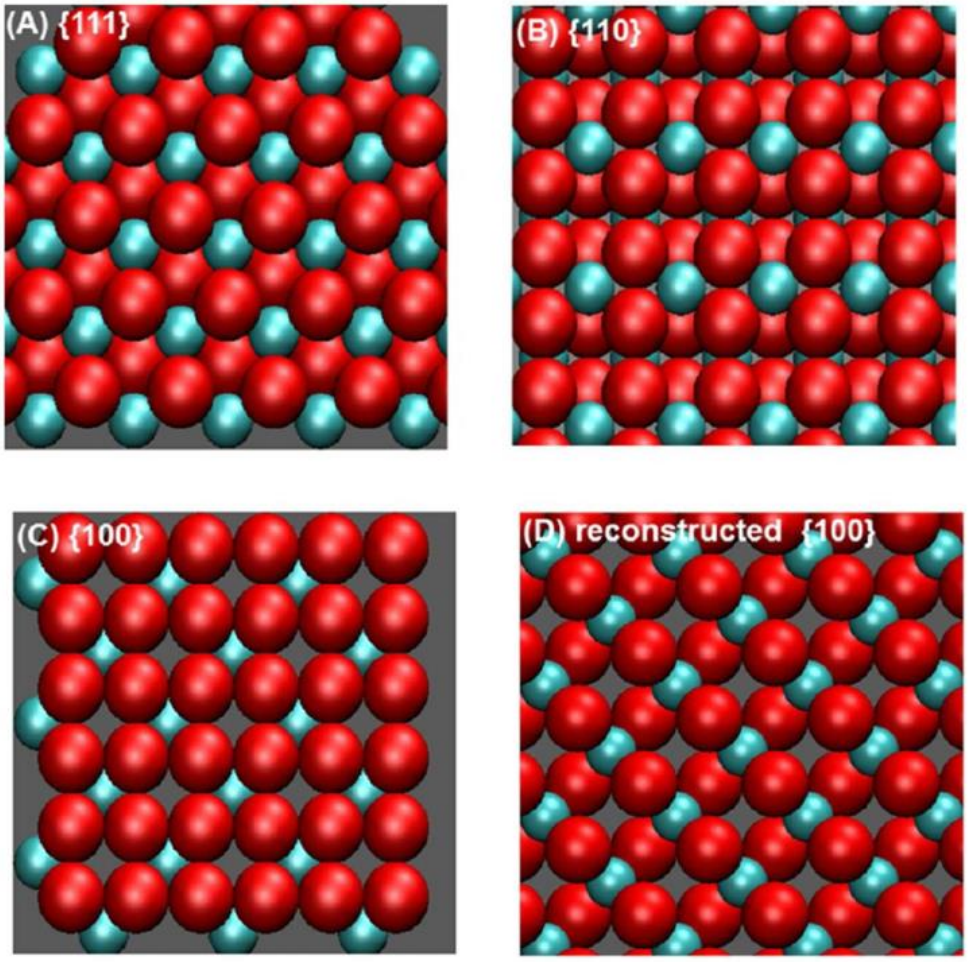

Figure 6.21 Surfaces of ceria a) (111) b) (110) c) (100) and d) reconstructed (100) by removing half of surface oxygen to remove polarity[3].

The calculated surface energy of ceria shown in Table 6.2 indicated that stability was in the order (111) < (110) < (100). On the other hand, upon reconstruction of (100) to remove the dipole moment ($100_{O\text{-half}}$), the stability of (100) and (110) were reversed suggested by the less favourable oxygen vacancy formation (2.40 and 1.99 eV respectively). Hence this might result in the disagreement between the energy of these two surfaces. Furthermore, when one oxygen atom was added into the reconstructed (100) surface ($100_{O\text{-half}+1}$), the oxygen vacancy formation became favourable. This suggested that between the unconstructed (100) surface and one oxygen added to the reconstructed surface, the oxygen vacancy formation was more

favourable than the (110) surface, implying (100) was the less stable surface in the surface CeO_x, $1 < x \leq 2$ range.

Surface	Calculated energy of oxygen vacancy formation (eV)
111	3.08
110	1.99
100	-1.98
$100_{O\text{-}half}$	2.40
$100_{O\text{-}half + 1}$	-1.56

Table 6.2 DFT calculated energy of oxygen vacancy formation of ceria surfaces.

The observations on the catalyst testing, TPR, STEM-EELS and PIE experiments all demonstrated that the ceria cubes support were superior to the rods, in terms of oxygen mobility and oxygen vacancy formation. It could be postulated that these characteristics were attributed to the (100) surface, at which under reaction conditions, being at the state of more than half filled oxygen CeO_x ($1 < x \leq 2$), which gave them the higher degree of oxygen vacancy formation and faster oxygen mobility during catalysis. At this state, the ceria (100) surface has a non-zero dipole moment perpendicular to the surface, therefore regarded as a polar surface which could possibly contribute to its surface properties through electrostatic interactions.

6.8 Conclusion

The surface oxygen of the ceria (100) surface on the cubes and the (110) on the rods were investigated as they influenced the catalytic behaviour in test reactions observed in Chapter 5, where the cubes support appeared to have faster oxygen mobility to clean the poison off the Pd

than the rods support. EPR measurements demonstrated that both of the supports were capable of producing oxygen vacancies. However, when Pd was deposited onto these ceria morphologies supports, TPR measurements indicated that the oxygen vacancy formation was more thermodynamically favourable on the cubes than on the rods. The observation in TPR agreed with STEM-EELS experiments where deposition of Pd enhanced the reducibility of the surface oxygen on both supports, hence increasing their oxygen vacancy formation. In addition, STEM-EELS also demonstrated the participation of bulk oxygen on the Pd deposited ceria cubes only, which was a kinetically driven process due to fast mobility of oxygen through the (100) surface. This bulk reduction of cubes was also observed in AP-XPS experiments where upon oxidation of the reduced 1% Pd/ceria cubes sample, the surface oxygen vacancies remained unfilled due to the replenishing of bulk oxygen vacancies. The kinetics of the oxygen mobility through the cubes and rods surfaces were investigated by performing PIE experiments where the cubes appeared to have faster oxygen mobility than the rods, indicated by the faster oxygen exchange rate, for both Pd deposited and undeposited samples. From DFT calculation, it was argued that these faster oxygen mobility and more favourable oxygen vacancy formation of the rods were attributed to the intrinsic properties of polar (100) surface being more than half filled with oxygen as opposed to the reconstructed (100) surface by removing half of the surface oxygen as suggested in the literature.

6.9 References

1. E. Aneggi, D. Wiater, C. de Leitenburg, J. Llorca and A. Trovarelli, *ACS Catal.*, 2014, 4, 172-181.

2. H. X. Mai, L. D. Sun, Y. W. Zhang, R. Si, W. Feng, H. P. Zhang, H. C. Liu and C. H. Yan, *J. Phys. Chem. B*, 2005, 109, 24380-24385.

3. Z. Wu, M. Li, D. R. Mullins and S. H. Overbury, *ACS Catal.*, 2012, 2, 2224-2234.

4. X. Wang, Z. Jiang, B. Zheng, Z. Xie and L. Zheng, *Crystengcomm*, 2012, 14, 7579-7579.

5. D. R. Mullins, P. M. Albrecht and F. Calaza, *Topics in Catalysis*, 2013, 56, 1345-1362.

6. S. Chang, M. Li, Q. Hua, L. Zhang, Y. Ma, B. Ye and W. Huang, *Journal of Catalysis*, 2012, 293, 195-204.

7. X. Du, D. Zhang, L. Shi, R. Gao and J. Zhang, *The Journal of Physical Chemistry C*, 2012, 116, 10009-10016.

8. T. Désaunay, G. Bonura, V. Chiodo, S. Freni, J. P. Couzinié, J. Bourgon, a. Ringuedé, F. Labat, C. Adamo and M. Cassir, *Journal of Catalysis*, 2013, 297, 193-201.

9. D. R. Mullins, *Surface Science Reports*, 2015, 70, 42-85.

10. M. Nolan, S. Grigoleit, D. C. Sayle, S. C. Parker and G. W. Watson, *Surface Science*, 2005, 576, 217-229.

11. J. Norenberg and J. H. Harding, *Surface Science*, 2001, 477, 17-24.

12. T. X. T. Sayle, S. C. Parker and C. R. a. Catlow, *Surface Science*, 1994, 316, 329-336.

13. J. C. Conesa, *Surface Science*, 1995, 339, 337-352.

14. D. C. Sayle, S. A. Maicaneanu and G. W. Watson, *Journal of the American …*, 2002, 124, 11429-11439.

15. J. Stubenrauch, E. Brosha and J. M. Vohs, *Catal. Today*, 1996, 28, 431-441.

16. R. M. Ferrizz, G. S. Wong, T. Egami and J. M. Vohs, *Langmuir*, 2001, 17, 2464-2470.

17. N. Yoshimichi, F. Ken-ichi and I. Yasuhiro, *Nanotechnology*, 2004, 15, S49.

18. S. Gritschneder, Y. Iwasawa and M. Reichling, *Nanotechnology*, 2007, 18, 044025.

19. J. Soria, J. M. Coronado and J. C. Conesa, *J. Chem. Soc.-Faraday Trans.*, 1996, 92, 1619-1626.

20. M. Figaj and K. D. Becker, *Solid State Ion.*, 2001, 141, 507-512.

21. E. Mamontov, T. Egami, R. Brezny, M. Koranne and S. Tyagi, *The Journal of Physical Chemistry B*, 2000, 104, 11110-11116.

22. M. Che, Kibblewh.Jf and A. J. Tench, *Journal of the Chemical Society-Faraday Transactions I*, 1973, 69, 857-863.

23. A. Martinez-Arias, J. C. Conesa and J. Soria, *Res. Chem. Intermed.*, 2007, 33, 775-791.

24. E. Aneggi, M. Boaro, C. D. Leitenburg, G. Dolcetti and A. Trovarelli, *Catal. Today*, 2006, 112, 94-98.

25. H.-X. Mai, L.-D. Sun, Y.-W. Zhang, R. Si, W. Feng, H.-P. Zhang, H.-C. Liu and C.-H. Yan, *The journal of physical chemistry. B*, 2005, 109, 24380-24385.

26. A. Trovarelli, *Comments on Inorganic Chemistry*, 1999, 20, 263-284.

27. R. Di Monte and J. Kaspar, *Topics in Catalysis*, 2004, 28, 47-57.

28. E. Aneggi, M. Boaro, C. D. Leitenburg, G. Dolcetti and A. Trovarelli, *J. Alloy. Compd.*, 2006, 408-412, 1096-1102.

29. K. Zhou, X. Wang, X. Sun, Q. Peng and Y. Li, *Journal of Catalysis*, 2005, 229, 206-212.

30. T. X. T. Sayle, S. C. Parker and C. R. A. Catlow, *Journal of the Chemical Society, Chemical Communications*, 1992, DOI: 10.1039/C39920000977, 977-978.

31. M. Nolan, S. C. Parker and G. W. Watson, *Surface Science*, 2005, 595, 223-232.

32. Z. Yang, Z. Lu, G. Luo and K. Hermansson, *Physics Letters, Section A: General, Atomic and Solid State Physics*, 2007, 369, 132-139.

33. G. N. Vayssilov, Y. Lykhach, A. Migani, T. Staudt, G. P. Petrova, N. Tsud, T. Skála, A. Bruix, F. Illas, K. C. Prince, V. Matolín, K. M. Neyman and J. Libuda, *Nature materials*, 2011, 10, 310-315.

34. C. W. A. Chan, A. H. Mahadi, M. M. J. Li, E. C. Corbos, C. Tang, G. Jones, W. C. H. Kuo, J. Cookson, C. M. Brown, P. T. Bishop and S. C. E. Tsang, *Nat. Commun.*, 2014, 5, 9.

35. S. Turner, S. Lazar, B. Freitag, R. Egoavil, J. Verbeeck, S. Put, Y. Strauven and G. Van Tendeloo, *Nanoscale*, 2011, 3, 3385-3390.

36. S. J. Haigh, N. P. Young, H. Sawada, K. Takayanagi and A. I. Kirkland, *Chemphyschem : a European journal of chemical physics and physical chemistry*, 2011, 12, 2397-2399.

37. L. J. Wu, H. J. Wiesmann, A. R. Moodenbaugh, R. F. Klie, Y. M. Zhu, D. O. Welch and M. Suenaga, *Physical Review B*, 2004, 69.

38. D. R. Mullins, S. H. Overbury and D. R. Huntley, *Surface Science*, 1998, 409, 307-319.

39. A. Pfau and K. D. Schierbaum, *Surface Science*, 1994, 321, 71-80.

40. E. Paparazzo, G. M. Ingo and N. Zacchetti, *Journal of Vacuum Science & Technology A*, 1991, 9, 1416-1420.

41. C. Hardacre, G. M. Roe and R. M. Lambert, *Surface Science*, 1995, 326, 1-10.

42. P. Burroughs, A. Hamnett, A. F. Orchard and G. Thornton, *Journal of the Chemical Society, Dalton Transactions*, 1976, DOI: 10.1039/DT9760001686, 1686-1698.

43. F. Tao, *Chemical Communications*, 2012, 48, 3812-3814.

44. R. A. De Souza and J. A. Kilner, *Solid State Ion.*, 1999, 126, 153-161.

45. H. J. M. Bouwmeester, C. Song, J. Zhu, J. Yi, M. van Sint Annaland and B. A. Boukamp, *Physical Chemistry Chemical Physics*, 2009, 11, 9640-9643.

46. C.-l. Song and J.-x. Yi, *Chinese Journal of Chemical Physics*, 2015, 28, 203-205.

47. N. Skorodumova, M. Baudin and K. Hermansson, *Journal*, 2004, 69.

48. M. Nolan, *Chemical Physics Letters*, 2010, 499, 126-130.

49. M. Baudin, M. Wojcik and K. Hermansson, *Surface Science*, 2000, 468, 51-61.

50. Y. J. Kim, Y. Gao, G. S. Herman, S. Thevuthasan, W. Jiang, D. E. McCready and S. A. Chambers, *Journal of Vacuum Science & Technology A*, 1999, 17, 926-935.

7 Conclusion and Future Perspective

Contents

7.1 Conclusion

The original aim of this research was to investigate the roles of different ceria surfaces as a support for Pd nanoparticles in heterogeneous catalysis. The surfaces of the ceria were controlled by fabricating the support into the cube and rod morphology, that predominantly exposes the (100) and (110) surface, respectively. The loading of 1% Pd was achieved by a deposition-precipitation method where well-dispersed Pd nanoparticles of 2 nm diameter were deposited onto these ceria morphologies.

The catalytic properties of 1% Pd deposited on the ceria cubes and rods were tested with methane combustion and gas-phase formic acid decomposition reactions. In both reactions, the 1% Pd/ceria cubes demonstrated minimal deactivation compared to the 1% Pd/ceria rods, resulting in higher TOF of the former. The exceptional catalytic properties of the 1% Pd/ceria cubes was attributed to the ability of the ceria cubes support in 'cleaning' the poison species off the Pd nanoparticles by oxidising them with the oxygen spilled over from its surface. It was hypothesised that these spilled over oxygen are formed more readily on the (100) surface than the (110) surface.

The properties of the surface oxygen of the ceria morphologies were investigated with various characterisation techniques. All evidences were in agreement in demonstrating that the ceria (100) surface on the cubes showed faster oxygen mobility and more favourable oxygen vacancy formation compared to the (110) surface of the rods, resulting in the enhancement of these unique properties of ceria.

7.2 Future Perspective

It is believed that these morphology control of ceria support and the fundamental knowledge acquired by this study could be applied to the industrial chemical processes which make use of the oxygen mobility and oxygen buffering capability properties of ceria such as the three way catalyst system. Based on this research, future development of ceria synthesis should be aimed at an efficient and economical method that maximises the (100) surface where these properties can be augmented, hence creating a ceria based catalyst with higher efficiency and activity. It could also be applied as a support for catalysed reaction that suffers rapid deactivation from poison species. With the ceria (100) surface, a new class of poison resistant catalysts based on controlled exposure of its active oxide surface could be developed.